

**Numerical Prediction of the Impact Response of Tailored 1500 MPa and 2000 MPa Press Hardening
Boron Steel**

By

Joseph Guignard

A Thesis
Submitted to the Faculty of Graduate Studies
through the Department of Mechanical, Automotive and Materials Engineering
in Partial Fulfillment of the Requirements for
the Degree of Master of Applied Science
at the University of Windsor

Windsor, Ontario, Canada

2022

© Joseph Guignard 2022

**Numerical Prediction of the Impact Response of Tailored 1500 MPa and 2000 MPa Press Hardening
Boron Steel**

by

Joseph Guignard

APPROVED BY:

A. Cherniaev
Department of Mechanical, Automotive, & Materials Engineering

R. Riahi
Department of Mechanical, Automotive, & Materials Engineering

D. Green, Co-Advisor
Department of Mechanical, Automotive, & Materials Engineering

W. Altenhof, Co-Advisor
Department of Mechanical, Automotive, & Materials Engineering

July 8, 2022

DECLARATION OF ORIGINALITY

I hereby certify that I am the sole author of this thesis and that no part of this thesis has been published or submitted for publication.

I certify that, to the best of my knowledge, my thesis does not infringe upon anyone's copyright nor violate any proprietary rights and that any ideas, techniques, quotations, or any other material from the work of other people included in my thesis, published or otherwise, are fully acknowledged in accordance with the standard referencing practices. Furthermore, to the extent that I have included copyrighted material that surpasses the bounds of fair dealing within the meaning of the Canada Copyright Act, I certify that I have obtained a written permission from the copyright owner(s) to include such material(s) in my thesis and have included copies of such copyright clearances to my appendix.

I declare that this is a true copy of my thesis, including any final revisions, as approved by my thesis committee and the Graduate Studies office, and that this thesis has not been submitted for a higher degree to any other University or Institution.

ABSTRACT

This thesis investigates the response of 1500 MPa and 2000 MPa press hardening steel (PHS) in a dynamic crushing scenario. The work involves creating numerical models to simulate tailored channel sections. The zones of different hardness are created using the tailored hot stamping process (THS), where a heated die set is used to quench an austenitized blank to produce parts with zones of differentiating hardness.

The 1500 MPa PHS was quenched using a die heated to different temperatures to produce a range of microstructures (225 HV to 473 HV) as well as the 2000 MPa PHS (297 HV to 574 HV). The as quenched specimens were characterized at strain rates of 0.003 s^{-1} (quasi-static), 0.1 s^{-1} (quasi-static), 100 s^{-1} (intermediate rate) and 1500 s^{-1} (high rate).

The PHS exhibited strain rate-sensitive behavior that was logarithmic in nature. The fully quenched 1500 MPa PHS exhibited an ultimate tensile strength that varied from 1502 MPa at a strain rate of 0.003 s^{-1} to 2003 MPa at a strain rate of 1500 s^{-1} . The 2000 MPa PHS exhibited a similar increase in strength with respect to strain rate.

The materials were tested for their ability to be spot welded so that the numerical models had accurate spot weld parameters. Both materials were welded using the same weld settings and produced average weld nugget sizes of 5.8 mm (1500 MPa PHS) and 5.3 mm (2000 MPa PHS).

Numerical models were developed using data from the uniaxial tensile testing and were simulated at different impact speeds. Axial crushing of tailored and fully hardened channels were simulated to compare the effects of tailoring PHS. The tailored and fully hardened channels absorbed similar amounts of energy. The tailored 1500 MPa PHS absorbed 4.84 kJ and 4.88 kJ for the tailored and fully hardened models. Similarly, the 2000 MPa PHS tailored and fully hardened models absorbed 4.92 kJ and 4.98 kJ, respectively. Although the absorbed energies are comparable, the tailored channels had a lower average impact force. The tailored channels also had more localized crushing, while the fully hardened channels deformed in several sections along their length.

To my dear Hannah

ACKNOWLEDGEMENTS

I would like to thank my supervisors Professor William Altenhof and Professor Daniel Green for giving me the opportunity to contribute to this project and for their continued support. They have provided guidance throughout this project that I am very lucky to have had. It has been an excellent learning experience that I feel will help immensely in the future.

I would also like to thank my fellow colleagues including Yang Song, Mohammad Shirinzadeh, Lauren Awad, Dr. Iman Sari Sarraf and Radha Thakkar. The project was greatly enhanced by the collective knowledge of the group, and they were a pleasure to work with.

Support for this project from our industrial partners Ford R&D, ArcelorMittal Dofasco and Marwood International is gratefully acknowledged as well as NSERC for their assistance.

Lastly, I would like to thank my parents, Cindy and André, and my siblings, Abbie and Lucas, as well as the rest of my family and friends for their unwavering support.

TABLE OF CONTENTS

| | |
|---|-----|
| DECLARATION OF ORIGINALITY | iii |
| ABSTRACT..... | iv |
| DEDICATION | v |
| ACKNOWLEDGEMENTS | vi |
| LIST OF TABLES..... | x |
| LIST OF FIGURES..... | xi |
| LIST OF APPENDICES | xv |
| 1. Introduction | 1 |
| 1.1 Background | 1 |
| 1.2 Motivation of Study | 1 |
| 1.3 Overview of Thesis | 2 |
| 2. Background | 3 |
| 2.1 The Hot Stamping Process | 3 |
| 2.2 Heating Techniques..... | 4 |
| 2.2.1 Conventional Heating..... | 4 |
| 2.2.2 Resistance Heating..... | 4 |
| 2.2.3 Induction Heating..... | 5 |
| 2.3 Tailoring techniques..... | 6 |
| 2.3.1 Bypass Resistance Heating..... | 6 |
| 2.3.2 Tailor-Welded Blanks | 6 |
| 2.3.3 Post tempering..... | 7 |
| 2.4 Material Characterization | 7 |
| 2.4.1 Microstructure | 7 |
| 2.4.2 Strain Rate..... | 9 |
| 2.5 Hardening Function Fitting | 11 |
| 2.6 Forming Limit | 14 |
| 2.7 Numerical Prediction of the Hot Stamping Process..... | 15 |

| | |
|---|----|
| 2.8 Spot Welding..... | 16 |
| 2.9 Numerical Simulation of Crash of As-Quenched Structures | 18 |
| 2.10 Crash Performance..... | 21 |
| 2.11 Damage Modelling | 23 |
| 2.12 Research Objectives..... | 25 |
| 3. Mechanical Testing Methodology..... | 27 |
| 3.1 Description of work..... | 27 |
| 3.2 Specimen Preparation..... | 28 |
| 3.2.1 Specimen Geometry..... | 28 |
| 3.2.2 Heat Treatment of Steel Specimens | 30 |
| 3.2.3 Specimen Hardness Testing | 31 |
| 3.3 Material Characterization | 34 |
| 3.3.1 Quasi-Static Tensile Testing | 34 |
| 3.3.2 Intermediate Rate Tensile Testing | 36 |
| 3.3.3 High Strain Rate Tensile Testing..... | 40 |
| 3.4 Extended flow curves..... | 45 |
| 3.5 Determination of Work Hardening Model..... | 46 |
| 3.6 Description of Hot Stamping Channel Die | 47 |
| 3.7 Channel Spot Welding..... | 49 |
| 3.7.1 Determination of Spot-Welding Parameters | 49 |
| 3.8 Axial Crush Fixture | 50 |
| 4. Numerical Simulation Models..... | 53 |
| 4.1 Uniaxial Tensile Test Numerical Model..... | 53 |
| 4.1.1 Boundary Condition of Uniaxial Numerical Model | 54 |
| 4.2 Channel Clamping Model | 54 |
| 4.2.2 Spot Weld Model | 56 |
| 4.2.3 Boundary Conditions..... | 58 |
| 4.3 Numerical Model of the Axial Crush Test | 58 |
| 4.3.1 Load Cell Modeling..... | 59 |
| 4.3.2 Boundary conditions | 59 |
| 4.3.3 Tailored Model..... | 60 |

| | |
|---|-----|
| 5. Mechanical Test Results..... | 61 |
| 5.1 Hardness Tests | 61 |
| 5.1.1 Tensile Specimen Hardness | 61 |
| 5.1.2 Split Hopkinson Bar Specimen Hardness | 64 |
| 5.2 Quasi-Static Tensile Testing | 65 |
| 5.3 Intermediate Rate Tensile Testing | 67 |
| 5.4 High-Rate Tensile Testing..... | 71 |
| 5.5 True Strain Rate | 74 |
| 5.6 Hardening Function Fitting | 74 |
| 5.7 Weld Parameters | 86 |
| 6. Numerical Model Results | 88 |
| 6.1 Uniaxial Tension Model Results | 88 |
| 6.2 Channel Clamping Model Results | 89 |
| 6.3 Axial Crush Model Results..... | 91 |
| 7. Conclusions and Recommendations | 98 |
| 7.1 Conclusions | 98 |
| 7.2 Recommendations | 99 |
| REFERENCES/BIBLIOGRAPHY | 101 |
| APPENDICES | 109 |
| A.3 Split Hopkinson Bar Grip Insert..... | 122 |
| B.1 Tailored 1500 MPa PHS at 25 m/s | 123 |
| B.2 Tailored 2000 MPa PHS at 40 m/s | 124 |
| VITA AUCTORIS | 126 |

LIST OF TABLES

| | |
|---|----|
| Table 1 - Chemical composition in wt.% of 1500 MPa PHS provided by ArcelorMittal..... | 27 |
| Table 2 - Mechanical properties of 1500 MPa PHS provided by ArcelorMittal..... | 27 |
| Table 3 - Chemical composition in wt.% of 2000 MPa PHS provided by ArcelorMittal..... | 28 |
| Table 4 - Mechanical properties of 2000 MPa PHS provided by ArcelorMittal..... | 28 |
| Table 5 – Thickness of tensile specimens for targeted pre-strain values. | 46 |
| Table 6 – Properties of steel [74]. | 55 |
| Table 7 - Average specimen hardness for rows in tailored sheets of 1500 MPa PHS. | 62 |
| Table 8 - Average specimen hardness for rows in tailored sheets of 2000 MPa PHS. | 63 |
| Table 9 - Average specimen hardness across rows in tailored sheets of 1500 MPa PHS. | 63 |
| Table 10 - Average specimen hardness across rows in tailored sheets of 2000 MPa PHS. | 64 |
| Table 11 - 100 s ⁻¹ strain rate validation metric results..... | 69 |
| Table 12 - R squared values for fitted Voce hardening functions of 1500 MPa PHS..... | 82 |
| Table 13 - R squared values for fitted Voce hardening functions of 1500 MPa PHS..... | 82 |
| Table 14 - Final weld parameters for 1500 MPa and 2000 MPa PHS. | 87 |
| Table 15 - Weld nugget sizes of 1500 MPa PHS..... | 87 |
| Table 16 - Weld nugget sizes of 1500 MPa PHS..... | 87 |
| Table 17 – Validation metric of 1500 MPa PHS. | 89 |
| Table 18 – 25 m/s crash performance parameters..... | 93 |
| Table 19 – 40 m/s crash performance parameters..... | 96 |

LIST OF FIGURES

| | |
|--|----|
| Figure 1 - Press hardening boron steel channel section..... | 2 |
| Figure 2 - Gradient of hardness values between the different heated zones of the specimen as a function of applied contact pressure and tool temperature in the heated tool zone [4]. | 3 |
| Figure 3 - Sequence of hot stamping of reinforcements using blanking immediately after resistance heating [12]. | 5 |
| Figure 4 - Functional principle of the two-step induction heating device [7]. | 6 |
| Figure 5 - Measured hardness distributions in the top, sidewall, and flange regions of the 1.2 mm channels (along z-axis) [15]. | 7 |
| Figure 6 - Schematic of the time–temperature-profile of a heated tool tailoring method (according to Merklein et al., 2013) [17]. | 8 |
| Figure 7 - Cooling curves with constant cooling rates superimposed on the CCT diagram of 22MnB5 (CCT data retrieved from ArcelorMittal, 2012a) (a) and corresponding prediction results of the Åkerström model (b) [20]. | 9 |
| Figure 8 - The engineering stress versus strain curves measured at different nominal strain [23]. | 10 |
| Figure 9 - Nominal strain rates considered in the experimental work of Okeeffe [27]. | 11 |
| Figure 10 - True stress–plastic strain curves of specimens after cold rolling (Material: C20E and SNCM220) [69]. | 12 |
| Figure 11 - Extending the hardening flow curve of (a) DP600 and (b) TRIP780 in RD by adding linear part of their corresponding biaxial flow curve (blue dashed lines) [70]. | 13 |
| Figure 12 - Fracture locus for fully bainitic material condition developed using forming limits [31]. | 14 |
| Figure 13 - Simulation results of the standard tensile tests for several interpolated material grades [20]. | 16 |
| Figure 14 - Hardness measurements extracted from the in-plane measurements and peak temperatures [32]. | 17 |
| Figure 15 - Hardness range and average hardness (in parentheses) for each bin in the crash models. Bins using the TCM II model are bolded [38]. | 19 |
| Figure 16 - Final Binned Parts [38]. | 20 |
| Figure 17 - Geometry of 3-Point Bend [41]. | 21 |
| Figure 18 - 2020 Ford F-150 driver-side small overlap frontal crash test [49]. | 22 |
| Figure 19 - Normalized damage accumulation [55]. | 24 |

| | |
|---|----|
| Figure 20 - The fracture loci of the different microstructures of Usibor® 1500-AS [56]. | 25 |
| Figure 21 - Mini Dogbone Tensile Specimen (units in mm). | 29 |
| Figure 22 - Engineering stress versus strain curves (up to the UTS) of the miniature dog-bone and subsize ASTM specimens (at 0.003 s^{-1}) [25]. | 30 |
| Figure 23 - a) H13 quenching dies with K-type thermocouple. b) Quenching furnace. | 31 |
| Figure 24 - Mounted hardness specimens in two-part epoxy. | 32 |
| Figure 25 - a. Buehler Micromet II Microhardness tester. b. Mounted hardness specimen. | 33 |
| Figure 26 - Locations of Vickers hardness tests on tailored sheet. | 34 |
| Figure 27 - MTS Criterion model 43 universal testing machine. | 35 |
| Figure 28 - Quasi-static tensile testing with DIC camera. | 36 |
| Figure 29 - Intermediate rate tensile testing apparatus with mini dogbone specimen. | 37 |
| Figure 30 - IRTTA speed versus air tank pressure. | 38 |
| Figure 31 - IRTTA mini dogbone grips. | 39 |
| Figure 32 - Mounted IRTTA grips with mini dogbone specimen. | 39 |
| Figure 33 - Split Hopkinson pressure bar testing setup. | 40 |
| Figure 34 - Split Hopkinson pressure bar modified grip wedge. | 41 |
| Figure 35 - Split Hopkinson bar specimen grip tailoring procedure. | 42 |
| Figure 36 - Split Hopkinson specimen mounting fixture. | 43 |
| Figure 37 - Split Hopkinson pressure bar with the mounted specimen. | 44 |
| Figure 38 - Split Hopkinson bar load cell calibration. | 45 |
| Figure 39 - Hot stamping channel die (front view). | 48 |
| Figure 40 - Hot stamping channel die (side view). | 49 |
| Figure 41 - Axial crush fixture with channel mounted to impact barrier. | 51 |
| Figure 42 - Detailed axial crush fixture. | 51 |
| Figure 43 - Removable section of axial crush fixture. | 52 |
| Figure 44 - Mini dogbone FEA mesh (half geometry). | 53 |
| Figure 45 - Strain rate logarithmic interpolation [46]. | 54 |
| Figure 46 - Mini dogbone boundary conditions. | 54 |
| Figure 47 - Meshed clamping fixture for a double hat channel section. | 56 |
| Figure 48 - Numerical model of the welded double-hat channel sections mounted in the clamp. | 57 |
| Figure 49 - Flange displacement for clamping simulation. | 58 |
| Figure 50 - Clamping simulation boundary conditions. | 58 |

| | |
|---|----|
| Figure 51 – Axial crush numerical model..... | 59 |
| Figure 52 - Specimen layout cut from tailored sheets..... | 61 |
| Figure 53 - Microhardness distribution of tailored and untailored specimens..... | 64 |
| Figure 54 - DIC strain processing for 1500 MPa PHS..... | 65 |
| Figure 55 - True stress versus true strain for 1500 MPa PHS at strain rates of 0.003 s^{-1} and 0.1 s^{-1} | 66 |
| Figure 56 - True stress versus true strain for 2000 MPa PHS at strain rates of 0.003 s^{-1} and 0.1 s^{-1} | 67 |
| Figure 57 - Strain calculation using motion tracking software..... | 68 |
| Figure 58 - MPa PHS quenched at $350\text{ }^{\circ}\text{C}$ comparison of filtering at 2000 kHz at a strain rate of 100 s^{-1} | 69 |
| Figure 59 - Average intermediate strain rate tensile testing for 1500 MPa PHS at a strain rate of 100 s^{-1} | 70 |
| Figure 60 - Average intermediate strain rate tensile testing for 2000 MPa PHS at a strain rate of 100 s^{-1} | 71 |
| Figure 61 - Average high strain rate tensile testing for 1500 MPa PHS at a strain rate of 1500 s^{-1} | 72 |
| Figure 62 - Average high strain rate tensile testing for 2000 MPa PHS at a strain rate of 1500 s^{-1} | 73 |
| Figure 63 - True strain rate versus true strain curves..... | 74 |
| Figure 64 - Average true stress versus true strain curves for 1500 MPa PHS quenched at $350\text{ }^{\circ}\text{C}$ at strain rates of 0.003 s^{-1} | 75 |
| Figure 65 - Experimental flow curves for 1500 MPa PHS at all strain rates and material hardness values ($250\text{ }^{\circ}\text{C}$ curves are omitted for clarity)..... | 76 |
| Figure 66 - Experimental flow curves for 2000 MPa PHS at all strain rates and material hardness values ($250\text{ }^{\circ}\text{C}$ curves are omitted for clarity)..... | 77 |
| Figure 67 - Voce flow curves quenched at $550\text{ }^{\circ}\text{C}$ for 1500 MPa PHS..... | 78 |
| Figure 68 - Voce flow curves quenched at $350\text{ }^{\circ}\text{C}$ for 1500 MPa PHS..... | 78 |
| Figure 69 - Voce flow curves quenched at $250\text{ }^{\circ}\text{C}$ for 1500 MPa PHS..... | 79 |
| Figure 70 - Voce flow curves quenched at $20\text{ }^{\circ}\text{C}$ for 1500 MPa PHS..... | 79 |
| Figure 71 - Voce flow curves quenched at $550\text{ }^{\circ}\text{C}$ for 2000 MPa PHS..... | 80 |
| Figure 72 - Voce flow curves quenched at $350\text{ }^{\circ}\text{C}$ for 2000 MPa PHS..... | 80 |
| Figure 73 - Voce flow curves quenched at $250\text{ }^{\circ}\text{C}$ for 2000 MPa PHS..... | 81 |
| Figure 74 - Voce flow curves quenched at $20\text{ }^{\circ}\text{C}$ for 2000 MPa PHS..... | 81 |
| Figure 75 - Ultimate true stress versus strain rate for 1500 MPa PHS..... | 83 |
| Figure 76 - Ultimate true stress versus strain rate for 2000 MPa PHS..... | 83 |
| Figure 77 - Extended hardening behaviour of 1500 MPa PHS fitted to a linear function..... | 84 |

| | |
|--|----|
| Figure 78 - Extended hardening behaviour of 2000 MPa PHS fitted to an exponential function. | 85 |
| Figure 79 - Extended flow curves for 1500 MPa PHS quenched at 550 °C. | 86 |
| Figure 80 - Extended flow curves for 2000 MPa PHS quenched at 550 °C | 86 |
| Figure 81 - Numerical predictions of the flow curves of 1500 MPa PHS quenched at 550C in uniaxial tension fitted with a rate-dependent Voce hardening function. | 88 |
| Figure 82 - Clamping simulation effective stress for 1500 MPa PHS. | 90 |
| Figure 83 - Clamping simulation effective stress for 2000 MPa PHS. | 91 |
| Figure 84 - Predicted force-displacement and energy absorption results for two 1500 MPa PHS channel sections that were quenched differently. | 92 |
| Figure 85 - Predicted force-displacement and energy absorption results for two 2000 MPa PHS channel sections that were quenched differently. | 93 |
| Figure 86 - 25 m/s projectile speed stress results. | 94 |
| Figure 87 - 40 m/s projectile speed stress results. | 94 |
| Figure 88 - Force-displacement and energy absorption numerical results with a 40 m/s projectile speed for tailored 1500 MPa PHS. | 95 |
| Figure 89 - Force-displacement and energy absorption numerical results with a 40 m/s projectile speed for tailored 2000 MPa PHS. | 96 |

LIST OF APPENDICES

| | |
|--|-----|
| Appendix A. Technical Drawings..... | 109 |
| Appendix B. LS-DYNA Energy Balance..... | 123 |
| Appendix C. Mesh Sensitivity for Axial Crush Numerical Simulation..... | 125 |

1. Introduction

1.1 Background

Boron steel meets several needs of a rapidly changing automobile industry. Canada is striving to reduce carbon emissions to net zero by 2050. Lightweight vehicles save on carbon emissions but still require strength to maintain their crashworthiness. 1500 MPa press hardening steel (PHS), and 2000 MPa PHS are 2nd generation boron steels that are press hardening. Press hardening steels are able to be simultaneously quenched and formed using special tools. In some cases, boron steels can be quenched to exhibit strengths of 2 GPa or more. However, ultra-high-strength steel is susceptible to brittle failure with a fully martensitic microstructure. The PHS most used in automotive body-in-white applications is 22MnB5 steel. By rapidly quenching sections of a part that require high strength and quenching slowly in sections that should remain more ductile in a crash event, tailored properties prevent brittle failure and maintain high strength. The hot stamping process has a profound effect on the performance of as-quenched parts. It offers the potential to significantly reduce the part weight by reducing its thickness and by removing redundant, overlapping material used to join parts together. A case study [1] showed a potential weight reduction of 38% for a tailored part, resulting in decreased fuel consumption and carbon emissions. Lightweight vehicles [2] reduce carbon emissions and increase comfort, performance, and functionality.

1.2 Motivation of Study

There currently exists a need to study advanced materials that are more suitable for crash and environmental applications. 1500 MPa PHS is a promising material for high strength applications and has been extensively studied and characterized; comparatively little research has been published on 2000 MPa PHS about its material's mechanical calibration. A strain-rate sensitive model is necessary to capture the high-speed deformation seen in crash scenarios, so several material testing rates are needed to understand this material better. 2000 MPa PHS can be used to make vehicles even lighter than before by using less material while still maintaining its structural integrity and energy absorption. A channel section (Figure 1) is used to simulate an energy-absorbing automotive component and is a consistent testing geometry as it is symmetric along its welded seam. Channel sections are created using a forming press to produce "hat sections" welded together.



Figure 1 - Press hardening boron steel channel section.

1.3 Overview of Thesis

This thesis is divided into 7 sections. A description of each section is outlined beginning with Chapter 2 which offers a comprehensive literature review of the hot stamping process. The chapter includes details of the different blank heating and tailoring methods, how press hardening steel is mechanically characterized, and the materials forming limit. In addition, the numerical modeling methods that have been used are discussed, and crash performance is quantified and outlined. Chapter 3 presents the experimental procedures used to conduct material tailoring, hardness testing, tensile testing at a range of strain rates, and weld testing. Chapter 4 outlines the methods used to create numerical models of the various tests. Chapter 5 presents the experimental results such as the specimen preparation validation, the two strain rates of quasi-static tensile tests, the intermediate strain rate tensile test, the high strain rate tensile tests, and the welding parameters. Chapter 6 outlines the results of the numerical models. Quasi-static tensile test models, intermediate rate tensile test models, and axial crush models are simulated. Finally, damage models are assessed and implemented to the tensile and axial crush models. Lastly chapter 7 provides a summary of the work. Finally, conclusions and recommendations are provided for future work on the project.

2. Background

2.1 The Hot Stamping Process

The automotive industry is currently using hot stamping for manufacturing lightweight structural and safety components [3], [4], [5]. Hot stamping is performed using either direct or indirect stamping methods [6]. Direct hot stamping consists of transferring a hot blank from a furnace to a press, where it is simultaneously formed and quenched. The indirect hot stamping process involves a subsequent heating and quenching process to achieve the desired mechanical properties in the part. Hot stamping can also be adapted to achieve parts with tailored properties. Merklein et al. [4] demonstrated the function of hot stamping and gives an overview of a method used to characterize the material and then predict its failure. ABAQUS V6.9 was used to simulate the process. The hot stamping process produces components that can have high strength and high elongation, all in the same part. It is important to carefully control the heating and forming process parameters to produce repeatable parts. Merklein et al. used a channel die with cartridge heating on one end and water cooling on the other in their experiments. The temperature difference created a heat gradient in the tool. Consequently, one end of the part became fully hardened, whereas a more ductile microstructure developed on the heated side, and a transition zone with mechanical properties that varied between these two end conditions (Figure 2).

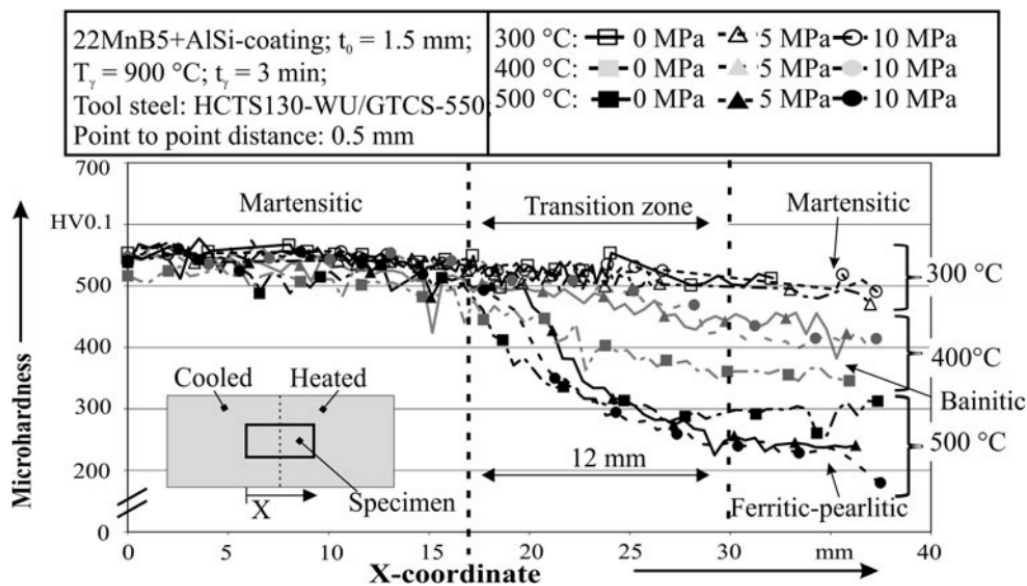


Figure 2 - Gradient of hardness values between the different heated zones of the specimen as a function of applied contact pressure and tool temperature in the heated tool zone [4].

Figure 2 shows the microhardness distribution across the tailored part when one end of the flat die was heated to different temperatures. Merklein et al. [4] also found that increasing the contact pressure and

the holding time increased the heat transfer coefficient (HTC) during quenching, which affected the final hardness in the softer zone. An investigation was also conducted to determine how the HTC of the tool is affected by whether both sides of the tool are in contact with the strip. For one-sided and two-sided contact, the HTC decreased as the gap between the die surface and the part increased to 5 mm, where after 5 mm, convection between the tool caused an increase in the HTC. As the gap increases the heat transfer mechanism changes from conduction to convection.

2.2 Heating Techniques

2.2.1 Conventional Heating

The conventional method for heating sheet metal blanks consists of using a gas or electric furnace [7]. The blank is placed in the furnace and heated to its desired temperature. While highly convenient and controllable, conventional heating is less energy efficient than other methods such as resistance heating and induction heating. In addition, the testing temperature influences the mechanical properties when forming tailored parts. The effects of different austenitization temperatures and die temperatures were studied by analyzing their influence on the true stress - true strain behaviour of 22MnB5 steel [8]. The tests proved that the soaking temperature needed to exceed 850°C to fully austenitize the sheet specimen and also that the strain rate during hot stamping had a significant effect on the final microstructure.

2.2.2 Resistance Heating

Metal sheets can also be heated quickly and efficiently by passing a high current through them. Resistance heating is faster than conventional heating, more space-efficient, and can synchronize with press cycle times [9][10][11][12]. Two-stage progressive die sets [13] create fully formed and punched hardened parts by blanking parts from an austenitized sheet. The sheet is heated using resistance heating and advanced using conventional uncoiling machines.

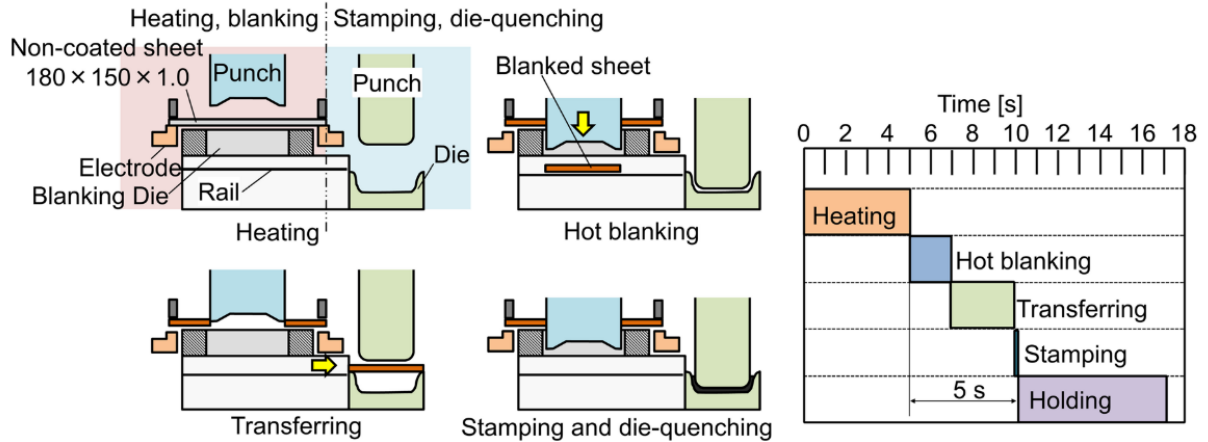


Figure 3 - Sequence of hot stamping of reinforcements using blanking immediately after resistance heating [12].

Figure 3 shows the resistance heating process to cut blanks from preheated sheets and form them after. The die incorporates resistance heating to heat individual sections of the strip as it is fed into the die. The resistance heating reduces the scale significantly as it reduces the average heating time compared to conventional furnaces from 210 s to 8 s. The faster heating time also reduces the need for coatings that are used for their corrosion-protection.

2.2.3 Induction Heating

A 2-stage induction heating method was investigated as a method of heating blanks [7]. An induction coil causes magnetic material to vibrate and generate large amounts of heat. The two stages are divided into the longitudinal and face induction stages. The longitudinal stage raises the temperature of the blank to the Curie temperature of the material. The Curie temperature corresponds to a temperature where certain magnetic materials, such as steel, show a drastic reduction in their magnetic properties. However, the blank temperature cannot go higher than the Curie temperature, so a second face induction method raises the blank to the desired temperature.

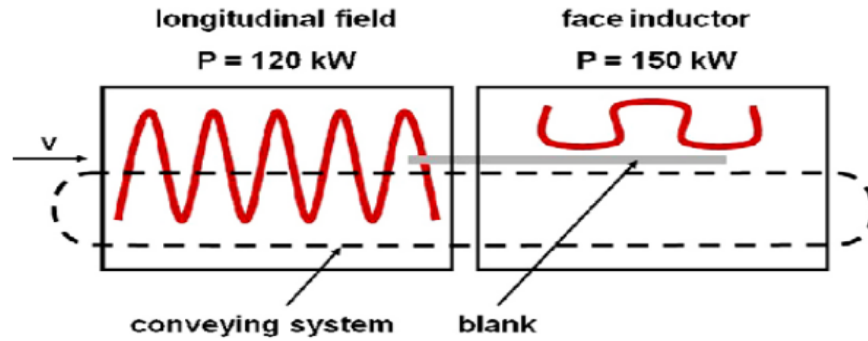


Figure 4 - Functional principle of the two-step induction heating device [7].

2.3 Tailoring techniques

Hot stamping of tailored parts is the focus of the current work, and there are several techniques used to tailor press hardenable parts. Each method was analyzed as they have potential benefits and drawbacks. Tailored hot stamping is used most often in the automotive industry as tailored parts typically do not need further post processing, and the tailoring is entirely carried out in the furnace and press. Other tailoring techniques are discussed below.

2.3.1 Bypass Resistance Heating

Tailored parts can be produced using resistance heating in only one section of the part: this is referred to as bypass resistance heating [14]. Mori et al. used large copper plates to reduce the electrical resistance of desired sections so the current will bypass the section. The bypassed sections were not quenched, and the microstructure remained unchanged in these sections to produce tailored parts.

2.3.2 Tailor-Welded Blanks

By laser welding different sheet materials together [15], a tailor-welded blank can be created that can be hot stamped to produce tailored, or engineered, parts (Figure 5). Such parts exhibit no transition zone other than the weld line, and they can be composed of sheet materials with different thicknesses welded together.

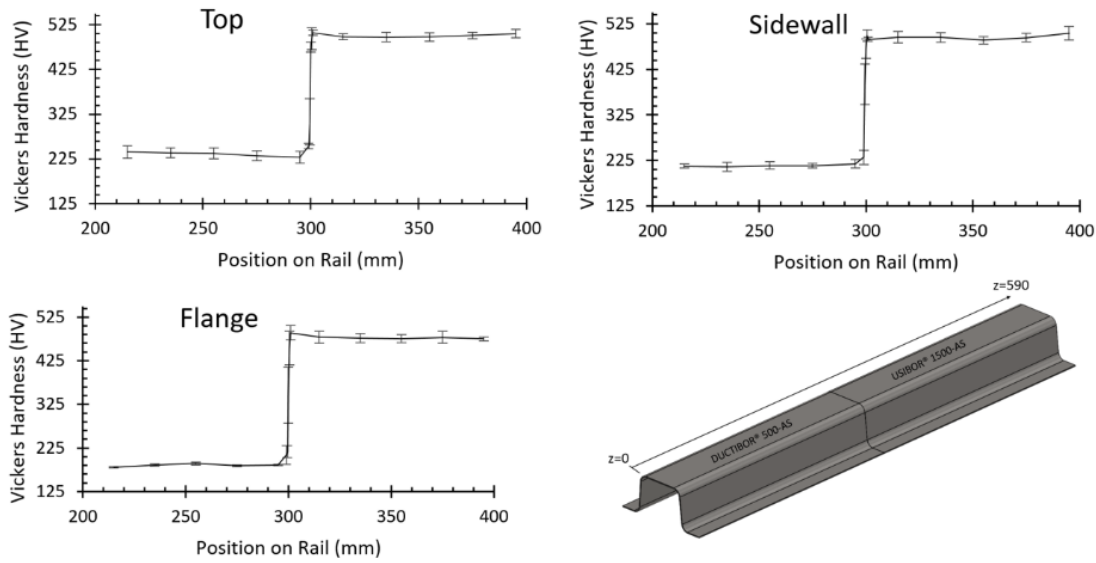


Figure 5 - Measured hardness distributions in the top, sidewall, and flange regions of the 1.2 mm channels (along z-axis) [15].

2.3.3 Post tempering

In addition to hot stamping, other processes can be applied to produce tailored effects. After quenching, tempering one region of the part [16] can change the microstructure from fully martensitic to softer multi-phase regions. The use of post tempering cannot be used if monotonic cooling of austenitized blanks is required.

2.4 Material Characterization

2.4.1 Microstructure

After fully austenitizing a press-hardenable steel sheet, it is then quenched in the forming die at a particular cooling rate. The cooling rate that is applied in each region of the part can be used to predict the final, as-quenched microstructure in that location. Different cooling rates pass through predicted microstructure zones in the continuous cooling transformation (CCT) diagram (Figure 6).

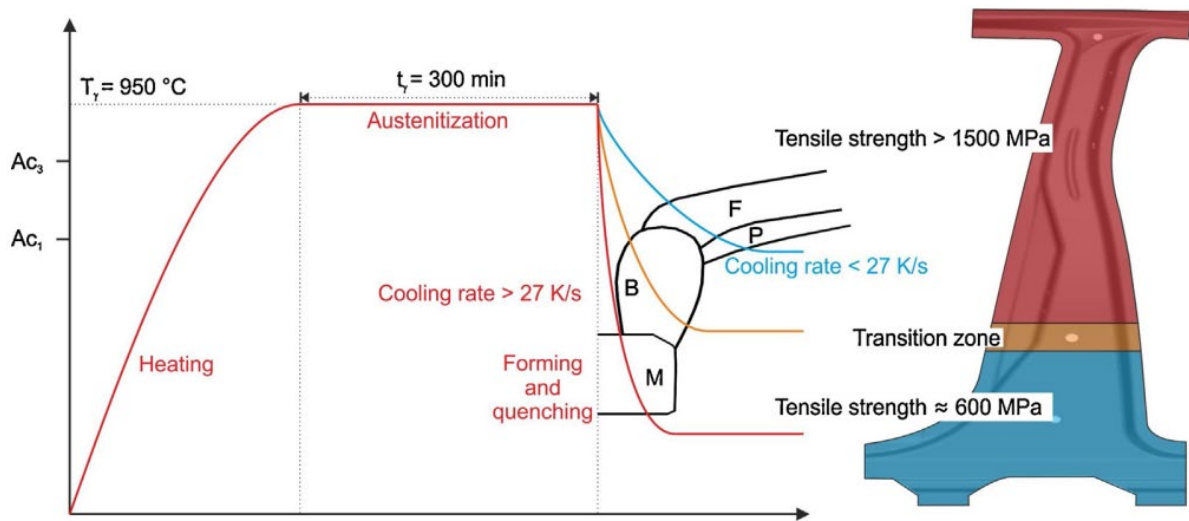


Figure 6 - Schematic of the time–temperature–profile of a heated tool tailoring method (according to Merklein et al., 2013) [17].

The critical cooling rate is that which is required to ensure the as-quenched microstructure is fully martensitic. For 22MnB5, the critical cooling rate is 27 K/s [18]. A slower cooling rate results in a microstructure consisting of bainite and possibly ferrite and pearlite. The slower cooling rates lead to “soft” zones with lower tensile strengths.

Plastic deformation of 1500 MPa PHS during forming operations have an effect on the formation of martensite and bainite [19]. The martensite start and end temperatures increase as the cooling rate decreases. The critical cooling rate increased to about 40°C/s after applying 40% of hot plastic deformation. Consideration of the plastic deformation and cooling rate are important to achieve an accurate material model and numerical prediction.

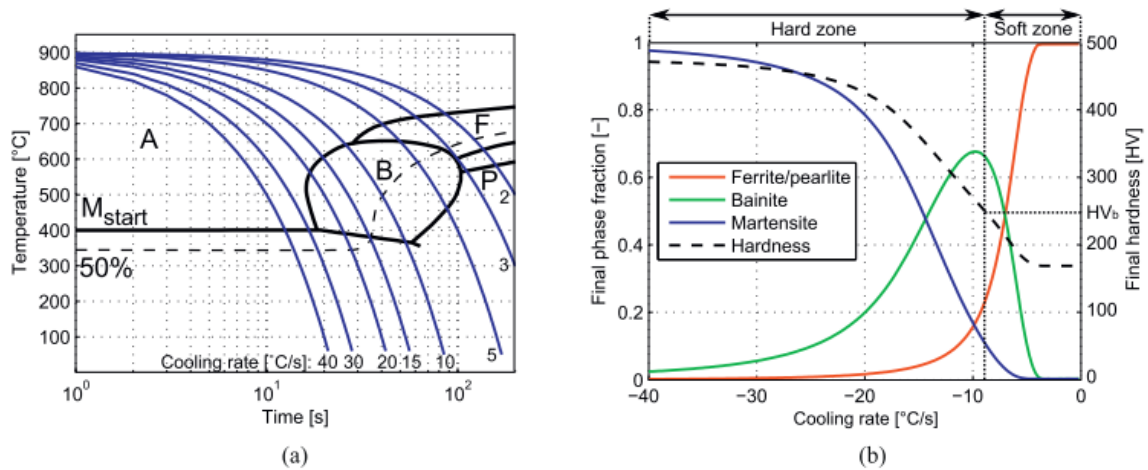


Figure 7 - Cooling curves with constant cooling rates superimposed on the CCT diagram of 22MnB5 (CCT data retrieved from ArcelorMittal, 2012a) (a) and corresponding prediction results of the Åkerström model (b) [20].

The final as-quenched microstructure of low-alloy steel can be predicted using phase-transformation equations [21]. The Åkerström [9] model used thermo-mechanical compression experiments at different strain rates to calibrate a model that is extended to steels with high boron content. Figure 7 shows how the Åkerström model is used to predict the microstructure composition in terms of the percentage of martensite, bainite, and ferrite/pearlite. It uses a bi-grade hardness-based model to predict mechanical properties. Martensite and bainite dominate the material's microstructure for cooling rates below 10 °C/s. A linear model between the two calibrated phases predicts the final properties. For cooling rates above 10 °C/s, the mechanical properties are predicted using a model comparing bainite and ferrite/pearlite. To achieve specific microstructures, each phase transformation's start and end temperatures are characterized [23] with different temperature histories and cooling rates.

The hot stamping process was also studied and found a 10% variation in tool temperature resulted in a 125% change in bainite fraction in the transition zone [22]. In addition, it was found that using different materials in the forming process drastically reduced the amount of energy required to heat the tool. A lower conductivity tool material, Macor®, was used in the forming die along with AISI H11.

2.4.2 Strain Rate

The influence of strain rate on the ultimate tensile strength and elongation is important, and the results significantly influence crash simulation predictions. Bardelcik et al. [23] investigated the effect of strain rate on the tensile strength of 1500 MPa PHS. As a result, the steel will react differently to different crash scenarios.

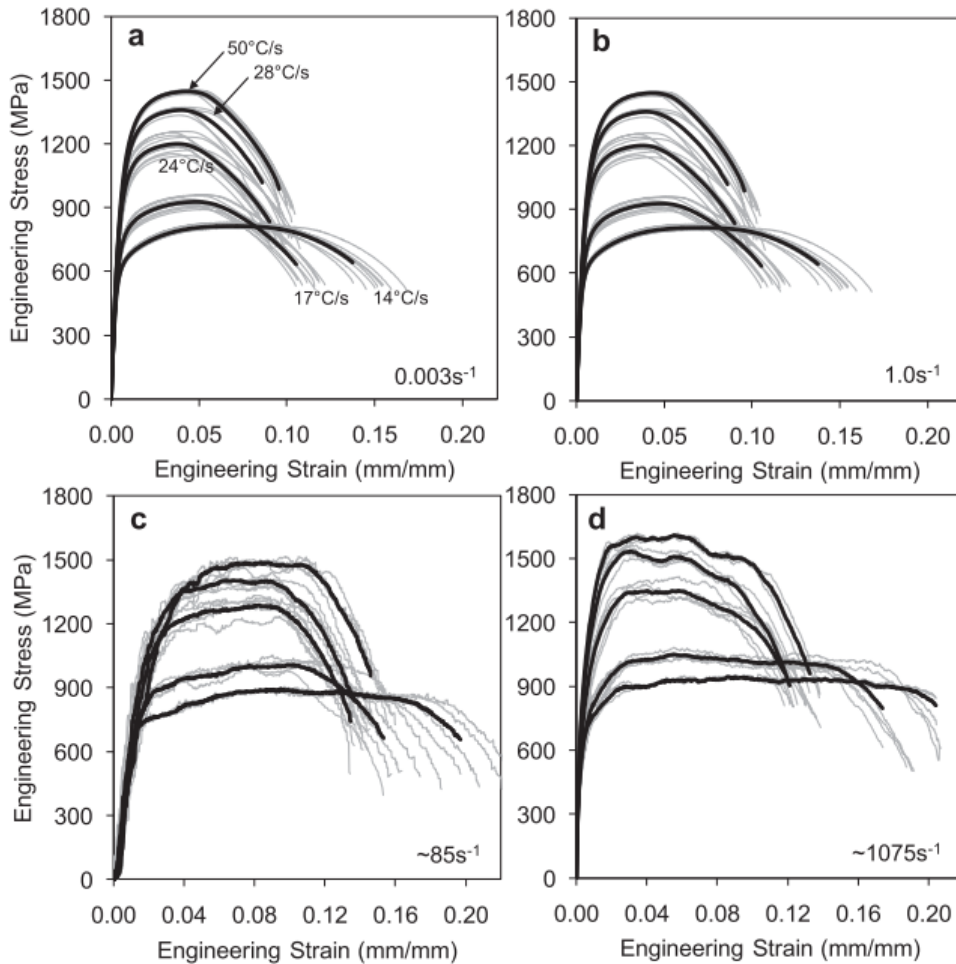


Figure 8 - The engineering stress versus strain curves measured at different nominal strain [23].

The experimental data shown in Figure 8 was obtained from different types of tests. A servo-hydraulic tensile testing apparatus was used to deform the samples at true strain rates of 0.003s^{-1} and 1.0s^{-1} . A drop tower deformed a specimen at a strain rate of 85s^{-1} . Similar intermediate strain rate testing was done in the strain rate range of 10 s^{-1} to 100 s^{-1} [24] [25] using an instrumented falling weight impact facility. A split Hopkinson bar testing apparatus achieved a strain rate of 1075s^{-1} .

The experimental data shows that boron steel is sensitive to strain rate: the tensile strength increases with increasing strain rates. These changes imply that the material will withstand a higher load under a crash situation. A strain rate of 100 s^{-1} is commonly experienced in a crash situation [26]. The highest strain rates of an automotive frame can be observed within highly localized folding in channel sections with values up to 1000 s^{-1} .

It is useful to show the strain rate on a logarithmic scale as strain rate sensitivity is often viewed as logarithmic [24]. In order to accurately model the dynamic impact of a part, the material must be

characterized at different strain rates, and the range of strain rates needs to be selected so as to cover the range of strain rates that can be experienced in an automotive crash scenario. Figure 9 shows the mechanical tests performed by O'Keefe [25] and how the strain rate of each test can be plotted on a logarithmic scale.



Figure 9 - Nominal strain rates considered in the experimental work of O'Keefe [27].

For uniaxial tension, different specimen geometries result in similar measured flow curves and ultimate stress values, providing the geometry are in accordance to the ASTM standard [28].

2.5 Hardening Function Fitting

Three types of constitutive models exist: phenomenological, physical, and artificial neural networks [64]. Phenomenological models do not consider the physical (micro-) mechanisms that are responsible for specific flow behaviour. Mathematical functions expressed in terms of various parameters that are dependent on the material's mechanical properties can be fitted to the experimental flow curves using regression analysis.

Physical models use temperature-dependent deformation micro-mechanisms to describe how a material will behave. These mechanisms may include dislocation theory, dynamic softening, and thermodynamic principles. Unfortunately, physical models are challenging to model and require advanced laboratory equipment to determine the material parameters and therefore they are rarely used to predict the forming behaviour of industrial-scale parts.

Artificial neural networks work by simulating artificial neurons. The neurons take input data and pass the data through hidden layers that attempt to solve the problem and output the material's behaviour. They have been proven highly accurate but can only be accurate using vast amounts of high-quality data that the neural network can be trained on.

An extensive study [65] compared seven hardening functions' ability to capture the behaviour of several materials. In each case, R-squared, adjusted R-squared, the goodness of fit, standard deviation, Total Normalized Mean Square Error, and the Normalized Mean Square Error were calculated to evaluate the hardening functions. A modified Johnson-Cook model was used to characterize high-strength alloy steel over a range of temperatures and low-strain rates [66]. The function considered yield, strain hardening,

temperature, and strain rate. The study evaluated the hardening functions with similar goodness of fit metrics to Sarrafs [67] work.

Uniaxial tensile data obtained from specimens subjected to quasi-static, medium, and high strain rates was fit to different phenomenological hardening functions [68]. A new approach based on nonlinear regression was used to fit the constants in the hardening equations and proved accurate and computationally efficient. However, the uniaxial data does not capture the behaviour up to large strain values, so additional tests need to be performed to extend the flow curves. A series of tensile tests conducted after various levels of cold rolling prestrains [69] demonstrated that cold rolling and subsequent tensile testing is a suitable approach to extend the stress-strain flow curve (Figure 10).

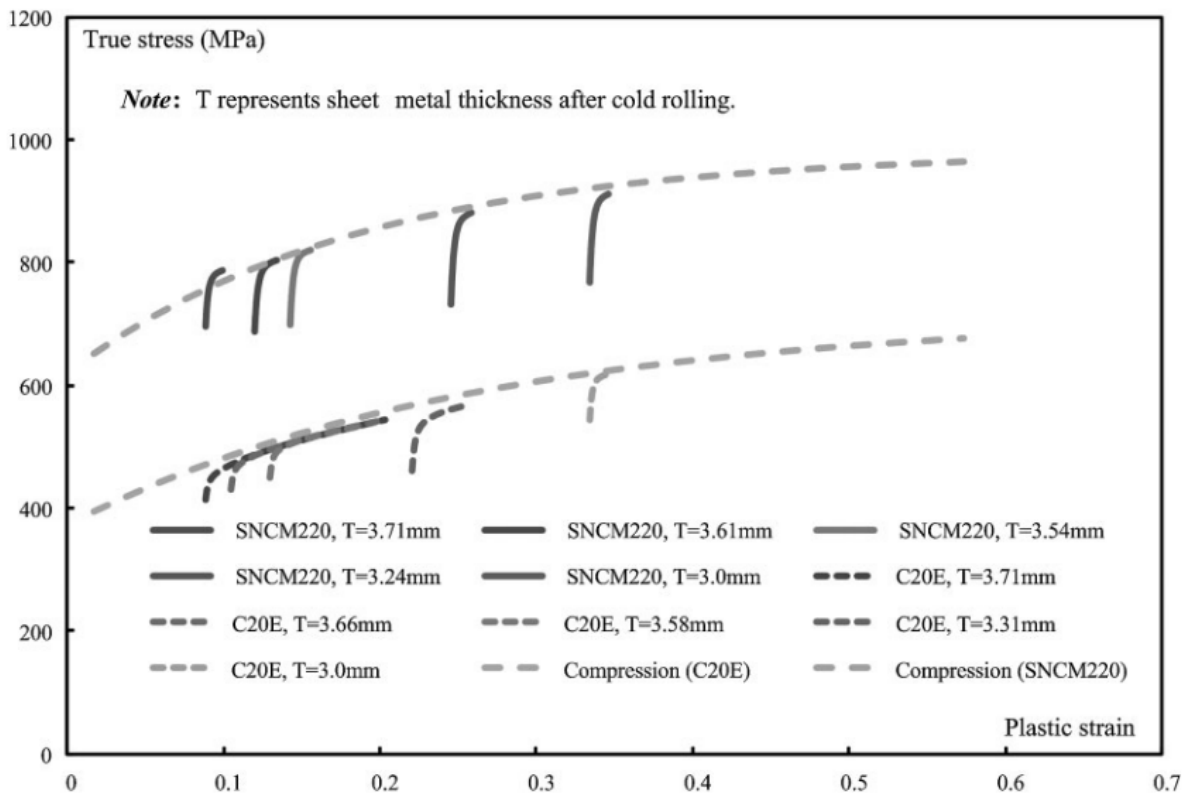


Figure 10 - True stress–plastic strain curves of specimens after cold rolling (Material: C20E and SNCM220) [69].

It has also been shown that combining hydrostatic bulge test data and uniaxial tension tests at different strain rates can also be used effectively to extend rate-dependent hardening functions [70]. The extended hardening behavior shown in Figure 11 was modeled as linear, and the transition between the linear and nonlinear behavior was smoothed using a 4-term Voce function.

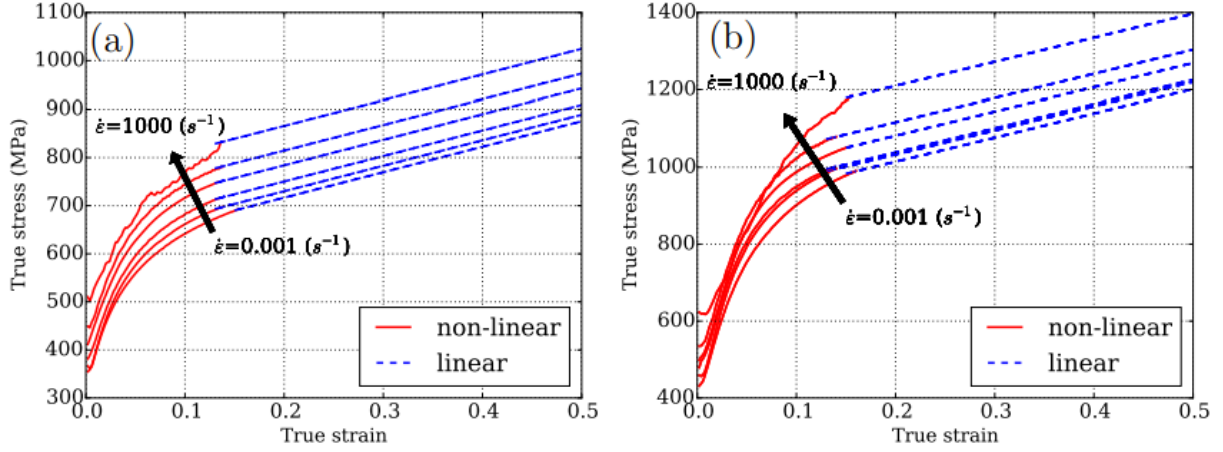


Figure 11 - Extending the hardening flow curve of (a) DP600 and (b) TRIP780 in RD by adding linear part of their corresponding biaxial flow curve (blue dashed lines) [70].

In contrast to the traditional linear regression method, genetic algorithms were used to determine parameters in commonly used constitutive equations [67]. The genetic algorithms proved more accurate than the commonly used linear regression. Three constitutive equations were tested. The Johnson-Cook [61] equation:

$$\sigma = (A + B\varepsilon^n) \left[1 + C \ln \left(\frac{\dot{\varepsilon}}{\dot{\varepsilon}_0} \right) \right] \left[1 - \left(\frac{T - T_r}{T_m - T_r} \right)^m \right] \quad (1)$$

where $\dot{\varepsilon}_0$ is the reference strain rate, and A, B, C, n, and m are material constants. T_r , T_m , and T denote room, melting, and test temperatures, respectively.

Khan et al. [71] proposed the Khan–Huang–Liang (KHL) equation:

$$\sigma = \left[A + B \left(1 - \frac{\ln \dot{\varepsilon}}{\ln D_0^p} \right)^{n_1} \varepsilon^{n_0} \right] \left(\frac{\dot{\varepsilon}}{\dot{\varepsilon}_0} \right)^c \left(\frac{T_m - T}{T_m - T_{ref}} \right)^m \quad (2)$$

where A, B, and C are material constants, m is the temperature exponent and n_0 and n_1 are the work hardening exponents.

The modified Voce equation is also used to predict hardening in rate-sensitive materials:

$$\sigma = [B - (B - A)(\exp(-m_1\varepsilon))] \times \zeta(\dot{\varepsilon}) \quad (3)$$

where A, B, C, D and m_1 are material constants to be calculated for each testing condition, and $\zeta(\dot{\varepsilon})$ is a term used to incorporate strain rate.

Of the three common equations used, the Voce [42] equation proved to be in better agreement than the Johnson-Cook and Khan–Huang–Liang equations.

2.6 Forming Limit

Damage modeling crushing experiments required a range of triaxialities that are not able to be achieved using uniaxial tension. 22MnB5 is characterized by its forming limit as a function of material thickness and forming temperature [29]. The tests performed by Li et al. were done using Nakazima [30] hemispherical dome tests with a range of geometries to generate a range of stress triaxiality values. Sheet thickness has a significant effect on the formability of 22MnB5. And the effect of the blank thickness is more prevalent at higher forming temperatures.

Forming limits have been found experimentally [31] under a range of forming temperatures and correlated to their final specimen hardness. In tailored crash scenarios, it is possible to calibrate damage and fracture based on a range of forming limits. Figure 12 shows the fracture locus interpolated from Kortenaars work.

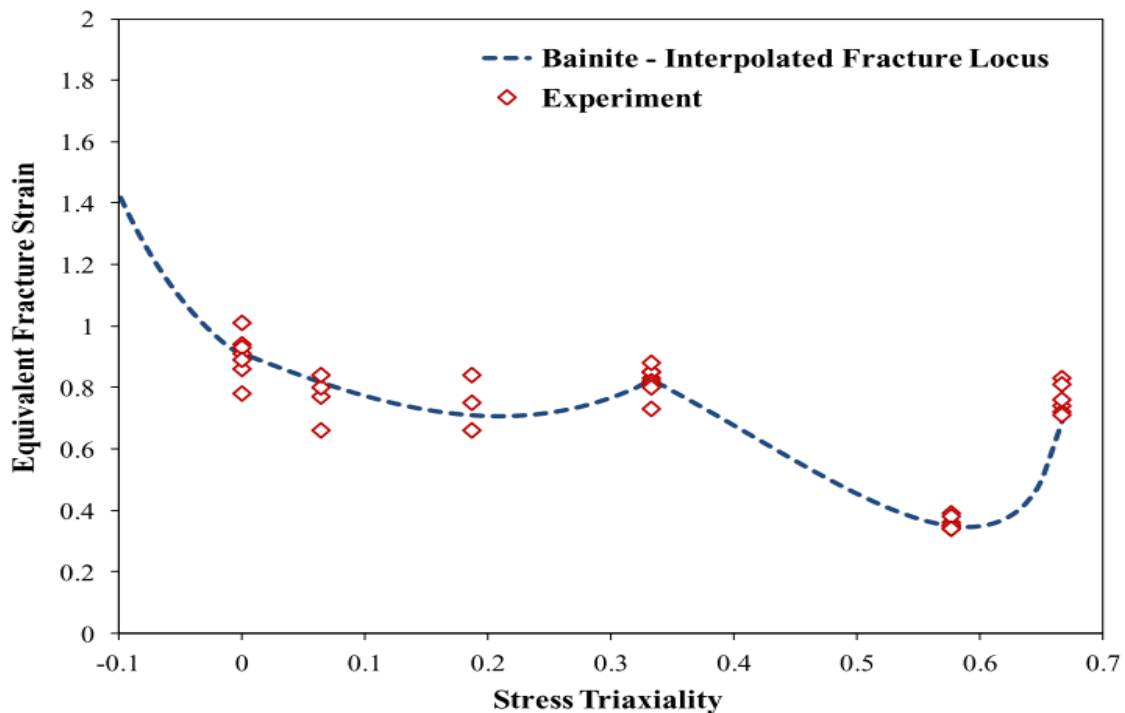


Figure 12 - Fracture locus for fully bainitic material condition developed using forming limits [31].

2.7 Numerical Prediction of the Hot Stamping Process

The hot stamping process was modeled numerically by Tang et al. [37][38] and validated using a heated forming die to create hat sections. The kinetics of phase transformations in the model was validated by examining the microstructure of experimental specimens. There was damage added to the numerical model used for hot stamping [39]. The model accurately predicted crack initiation and its damage evolution.

Eller et al. [20] created a constitutive model that is strain rate dependent and can predict the stress state from the hardness of the material. A model of 22MnB5 was constructed using three hardness grades. A cooling rate of 2°C/s, 29°C/s, and 120°C/s resulted in a ferrite/pearlite, bainite, and martensite microstructure, respectively. For hardness values found to be lower than that of bainite, the following equations were used:

$$\sigma_y(\bar{\epsilon}_p, X_b) = (1 - X_b) \cdot \sigma_{y,fp}(\bar{\epsilon}_p) + X_b \cdot \sigma_{y,b}(\bar{\epsilon}_p) \quad (4)$$

$$\bar{\epsilon}_f(\eta, \bar{\theta}, X_b) = (1 - X_b) \cdot \bar{\epsilon}_{f,fp}(\eta, \bar{\theta}) + X_b \cdot \bar{\epsilon}_{f,b}(\eta, \bar{\theta}) \quad (5)$$

$$X_b(HV) = \frac{HV - HV_{fp}}{HV_b - HV_{fp}}, \quad HV_{fp} \leq HV \leq HV_b \quad (6)$$

A similar set of equations relating hardness values above that of bainite is presented in the works as well. These equations consider the Lode angle, stress triaxiality, and the experimentally found values of stress/strain. Figure 13 shows the stress-strain curves that were calculated.

This material model is helpful as numerical models in LS-DYNA can be made to output the hardness values of a part to be associated with a hardening behavior.

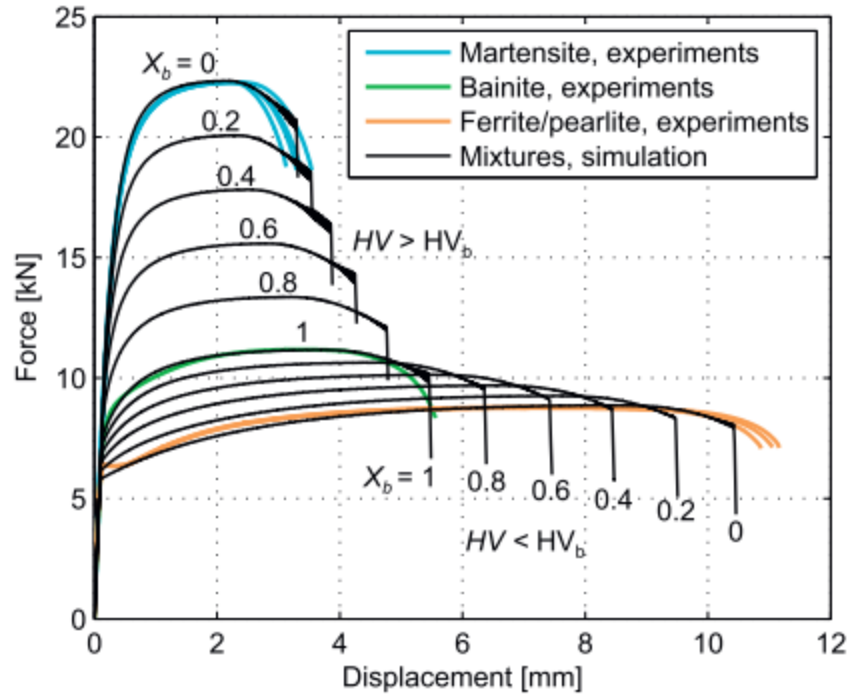


Figure 13 - Simulation results of the standard tensile tests for several interpolated material grades [20].

2.8 Spot Welding

Spot welds are widely used to assemble automotive parts and therefore any experimental or numerical simulation of crash must consider the mechanical properties of spot welds. The hat sections are joined together to make tubular parts. The hat sections are welded together by resistance welding. The spot welding creates a unique problem: indeed, a large amount of heat added to the parts will change the predicted microstructure.

Eller et al. [32] found that resistance spot welding changes the material properties by influencing a new gradient of hardness radially around the weld called the heat-affected zone (HAZ). The study used five grades of 22MnB5 to cover a range of microstructure from fully martensitic to ferritic/pearlitic. In order to determine if the microstructure of the weld and HAZ had been weakened, tensile tests were conducted. There is a temperature gradient from 2200 °C at the center of the weld to room temperature at the outside. Hardness drops were hypothesized to occur at distances corresponding to austenitization temperatures (Figure 14). The hardness drop at the HAZ is of interest because it is a point of failure in primarily martensitic microstructures.

When testing the tensile strength of the welded samples, the two softest materials had no change in the strain associated with failure. The harder samples failed much sooner as the HAZ is softer than the specimen due to the welding. Weld nuggets are always found fully hardened after welding for each sample

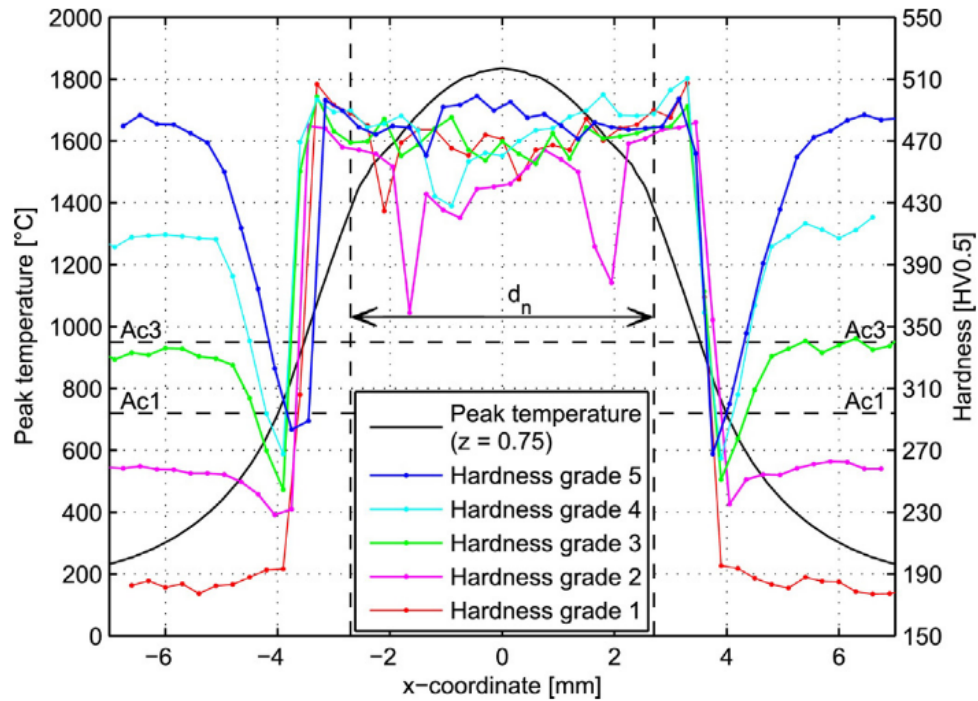


Figure 14 - Hardness measurements extracted from the in-plane measurements and peak temperatures [32].

due to the material cooling from above the melting temperature very quickly [32]. The heat-affected zone is simulated using a straight line down to the critical HAZ then linearly back up to the original hardness value of the material.

Pouranvari [33] outlines the type of failure mechanisms associated with spot welds. Spot welds have two methods for failure: interfacial failure or pullout failure. An interstitial failure occurs when there is a fracture along the weld nugget. A pullout failure occurs when the weld nuggets from one sheet are removed from the other. The study explored the option of using martensitic stainless steels in place of quenchable boron steel. Moreover, the study was extended to boron steel and obtained similar results [34]. Pullout failure is desirable for crashworthiness as it typically can absorb the most energy [35].

Xiang et al. [36] analyzed the differences in modeling spot-welds in detail. The ideal situation is where no spot-weld failure occurs as it removes the error associated with the damage modeling of the spot-welds from the model, so to avoid this issue, the appropriate size and amount of spot-weld must be chosen. In the no-damage condition, the rigid-node spot-weld condition was selected to be suitable out of 16

methods of simulation. The rigid-node method is simple, which involves the coupling of all 6 degrees of freedom of opposing nodes to each other. Also included is a study on how many spot welds are needed along the flange to achieve consistent results. With a 200 mm long tube, spot-welds closer than 25 mm apart produced consistent results.

The failure of resistance spot welds has been characterized [27]. The testing included lap shear, cross tension, V-bend, and standard uniaxial tensile testing. The tested material was 1500 MPa PHS with 1.2 mm and 1.6 mm thickness and quenched at different cooling rates. The numerical models included an “energy fade” parameter that reduced the effect of element deletion, causing all the spot welds to fail one by one. This energy fade parameter causes the model to respond more realistically as if the spot weld was pulling out.

2.9 Numerical Simulation of Crash of As-Quenched Structures

Bardelcik [23] found that materials with the same hardness did not have uniform elongations due to different pre-strain conditions. Due to the need to input each hardness as a material in LS-DYNA, LS-DYNA cannot simulate the hat-shaped part efficiently using a gradient of mechanical properties. Omer et al. [40] used a binning technique shown in Figure 15. After predicting the hardness of the formed part using the Åkerström [41] material model implemented in LS-DYNA, the elements hardness values were averaged to reduce the number of different material models to be between five and ten.

| Bin Number | Fully Cooled | Single Soft Zone 400°C | Single Soft Zone 700°C | Graded Soft Zone |
|-------------------|---------------------|-----------------------------------|-----------------------------------|-----------------------------|
| 1 | 456-462 (459.4) | 252-275 (266.8) | 192-221 (203.7) | 182-213 (199.5) |
| 2 | 463-468 (465.5) | 276-299 (288.5) | 222-250 (243.7) | 214-244 (227.0) |
| 3 | 469-474 (471.6) | 300-322 (308.3) | 251-279 (258.5) | 245-275 (250.6) |
| 4 | 475-480 (477.6) | 323-345 (333.4) | 280-309 (290.9) | 276-306 (285.6) |
| 5 | 481-487 (483.7) | 346-368 (355.1) | 310-338 (328.1) | 307-337 (319.8) |
| 6 | | 369-391 (378.9) | 339-367 (354.1) | 338-368 (353.2) |
| 7 | | 392-415 (402.9) | 368-396 (383.2) | 369-399 (386.4) |
| 8 | | 416-438 (426.6) | 397-425 (413.7) | 400-430 (415.8) |
| 9 | | 439-461 (448.3) | 426-455 (442.0) | 431-461 (448.4) |
| 10 | | 462-485 (477.3) | 456-484 (477.7) | 462-492 (477.6) |

Figure 15 - Hardness range and average hardness (in parentheses) for each bin in the crash models. Bins using the TCM II model are bolded [38].

A “Tailored Crash Model” (TCM) I [28] and TCM II [42] model was implemented for the hardening curves. The TCM I model is a modified version of the Voce [42] hardening model:

$$\sigma = \left(A + \left((B - A)e^{-\frac{\varepsilon}{c}} \right) \right) (1 + \varepsilon)^D \quad (7)$$

The defined the parameters A,B,C and D are defined as functions of Vickers hardness. All elements except those containing more than 1% ferrite were modeled using the TCM I model. The TCM II model is also Voce-based, but the parameters are found using functions of the area fraction of bainite, martensite, and ferrite instead of the Vickers hardness.

There are bins of five to ten different hardness values which can be simulated using the model. Omer used this method as the input to the dynamic crush simulation. The methodology used was first to reflect the part to form the double hat section. The next step was to add a fold initiator (an indentation at the top of the hat section to initiate the first fold). Next the spot-weld were meshed with the same parameters as Prajogo [43]. Lastly boundary conditions were imposed.

Figure 16 shows the binned part with five material models. The binned zones are nontrivial, so they must be derived from a numerical simulation and inputted into the crash model.

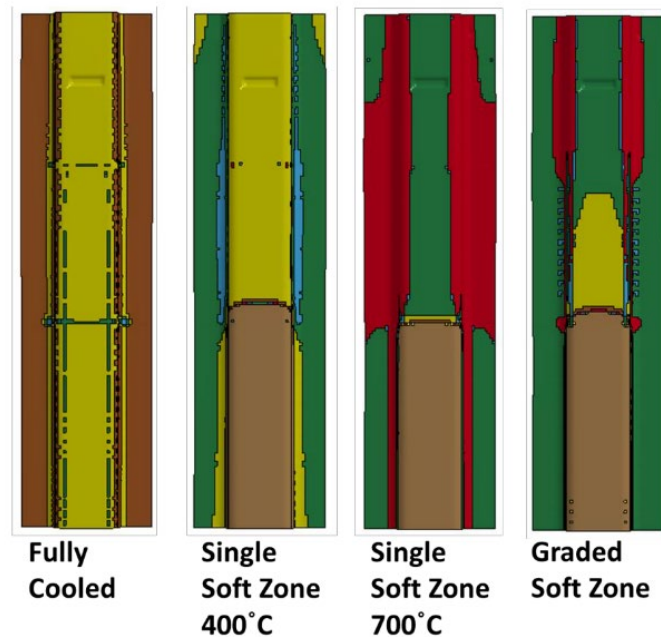


Figure 16 - Final Binned Parts [38].

The fold initiator was not simulated in the forming operation but was created in the crash model by displacing nodes 4 mm to the center. The channel sections are 600 mm long and have a cross section that is 125 mm by 125 mm. This approach to modeling the fold initiator will affect the material properties in the area. The boundary conditions restricted the bottom 50 mm of elements fully but left the top rows of elements with no boundary conditions.

Using a Belytschko-Tsay shell element formulation, seven integration points were used through the thickness of the elements. Bari [44] shows that five integration points are sufficient to simulate a crash situation, so seven integration points will be sufficient. A mesh sensitivity analysis determined that a 3 mm x 3 mm [45] element size provided acceptable results.

Quasi-static and dynamic 3-point bend tests were simulated and validated using experimental results by Prajogo [43]. Analyses were conducted on both a full spot-welded backplate and a split backplate. The split backplate localizes the bending further, modeled with deformable quadrilateral shell elements with a size of 2.5 mm by 2.5 mm; however, the backing plate was modeled using the same type of elements only with a size of 5 mm by 5 mm since they experience relatively small deformations. Figure 17 shows the model's geometry, and the different colors indicate the different hardness zones created in the hot

stamping process. The simulation uses quarter symmetry due to the symmetrical nature of the test. The spot welds are simulated using the *MAT_SPOTWELD keyword within LS-DYNA [46] with a diameter of 8 mm.

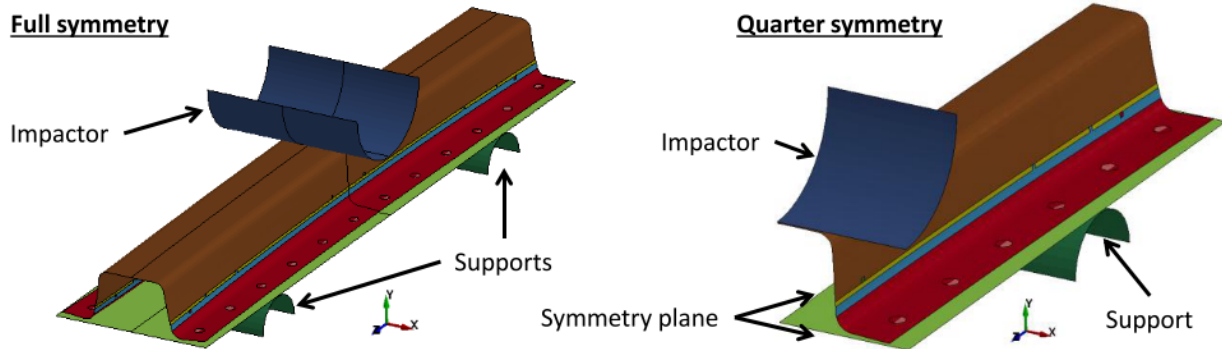


Figure 17 - Geometry of 3-Point Bend [41].

Hot-stamped tailor-welded blanks were studied to characterize the failure of laser-welded sheets of Ductibor® 500-AS and Usibor® 1500-AS [47]. As a result of the austenitization process before quenching in water-cooled flat dies, the weld line had a homogenous microstructure. Typical laser-welded parts have a hard fusion zone in the center and a soft heat-affected zone around the fusion zone. Therefore, tailor welded blanks reduce the chance of weld failure. An analysis of the axial crush and three-point bending performance of hot-stamped tailor-welded blanks was conducted [48]. The study also used Ductibor® 500-AS and Usibor® 1500-AS as the materials to be welded together. The transition zone between the materials was 2 mm. The numerical model includes rate sensitivity, a GISSMO failure model, and a spot weld failure model modeled using the same parameters as O’Keeffe et al. [47]. The tube structures were sand blasted prior to crashing them to prevent the aluminum-silicone coating from chipping off during the crash and obstructing the high-speed cameras.

2.10 Crash Performance

Crashworthiness measures a vehicle's ability to protect its occupants from a crash. Crashworthy vehicles absorb energy during an impact while maintaining the integrity of the passenger compartment. It is necessary to absorb impact energy as well as to stop intrusion into the passenger compartment [49]. It is also required to avoid large accelerations or decelerations within human tolerance limits to mitigate serious injury or death to any occupants. Figure 18 shows an example of a crashworthy vehicle that absorbed kinetic energy while maintaining the integrity of the passenger’s cabin.



Figure 18 - 2020 Ford F-150 driver-side small overlap frontal crash test [49].

The ultimate crashworthiness of a vehicle depends on how the vehicle can protect its passengers. The general crashworthiness can be significantly improved, considering advanced materials and clever design. For example, a redesigned B pillar [50] that uses tailor welded blanks instead of traditional methods reduced intrusion displacement and velocity in the passenger compartment.

Materials with ultra-high-strength can prevent deformations of the frame and mitigate intrusions into the vehicle, but they do not absorb much energy because once they yield, they are less ductile and fail. Therefore, more ductile materials can absorb energy as they can deform significantly prior to failure. The use of tailored hot stamped parts in a vehicle structure can ensure both its structural integrity with ultra-high-strength regions and its ability to absorb impact energy with engineered soft zones.

The crashworthiness of a structure is measured by its ability to absorb impact energy and bring the vehicle to rest without causing the occupant to experience rapid deceleration, as defined by several metrics [51] [52]. The first metric that indicates crashworthiness is the total energy absorption, TEA (Eq. 8 and 9). The TEA is calculated by integrating the force acting on the specimen with respect to the crushing displacement. Equation 9 shows how TEA is estimated with numerical integration. Specific energy absorption, SEA, is calculated as TEA normalized with respect to mass:

$$TEA = \int_0^{\delta_T} F(x)dx \quad (8)$$

$$TEA = \sum_{i=1}^{N-2} F_i \cdot \left(\frac{\delta_{i+1} - \delta_{i-1}}{2} \right) \quad (9)$$

Crush force efficiency, CFE is typically defined as the ratio of mean load, F_m to initial peak force, F_{max} .

$$CFE = \frac{F_m}{F_{max}} \quad (10)$$

An ideal value of crush force efficiency is 100%, but it is impossible to achieve this as the initial impact force is difficult to reduce. Mean crushing force provides an average force throughout the test defined as:

$$F_m = \frac{1}{\delta_T} \int_0^{\delta_T} F(x)dx \quad (11)$$

Hsu and Jones [53] discuss a metric for characterizing the ratio of TEA normalized with respect to the same volume of sacrificial material called the energy-absorbing effectiveness factor (EAEF). For a circular extrusion, this metric can be defined as:

$$\psi = \frac{F_m \delta_T}{\pi \sigma_o \epsilon_f (r_o^2 - r_i^2) L} \quad (12)$$

The last metric for crashworthiness is the initial peak impact force. However, it is useful when comparing samples against each other.

2.11 Damage Modelling

Damage in a numerical material model relates a damage value reaching a threshold where the material would normally fail. Eller et al. [20] modeled damage in a numerical model using a modified Mohr-Coulomb fracture criterion. The model relates stress triaxiality to the Lode angle and allows the model to calibrate to the experimental values. In addition, the model implements a damage indicator to predict where the initial fracture begins and how it will propagate through the material. This model was validated using a four-point bending test on a hat-shaped section. The model accurately predicted the fracture locations and is considered to be accurate.

LS-DYNA implements several damage models, including the generalized incremental stress state dependent damage model (GISSMO) [54], with rate-sensitive constitutive behavior. The GISSMO model is a phenomenological damage model that Daimler developed. The model accurately predicts instability,

which is essential for crash situations [55]. The GISSMO model calculates instability and damage separately from the existing material model and its plasticity. The parameters in the material model are determined using a variety of mechanical tests that correspond to different stress triaxialities.

The fracture loci are characterized [56] using 0°, 10°, and 30° butterfly specimens [57], hole expansion tests [58], VDA 238–100 V-bend tests [59], and Nakazima-type plane-strain and equal-biaxial tension tests [30].

The previous approach to crash damage in LS-DYNA was the Gurson model [60]. The model inherently uses stress triaxiality in the damage evolution. However, it underpredicts damage in most cases and cannot capture fracture under shear stress states. The yield function is expressed as a function of void nucleation with failure being initiated at a critical void volume fraction. Figure 19 shows a linear damage accumulation from the Johnson-Cook [61][62] damage model, non-linear damage accumulation using the Gurson damage model, and that predicted by the GISSMO damage model. The Johnson-Cook model is shown to overestimate damage while the Gurson model underestimates it.

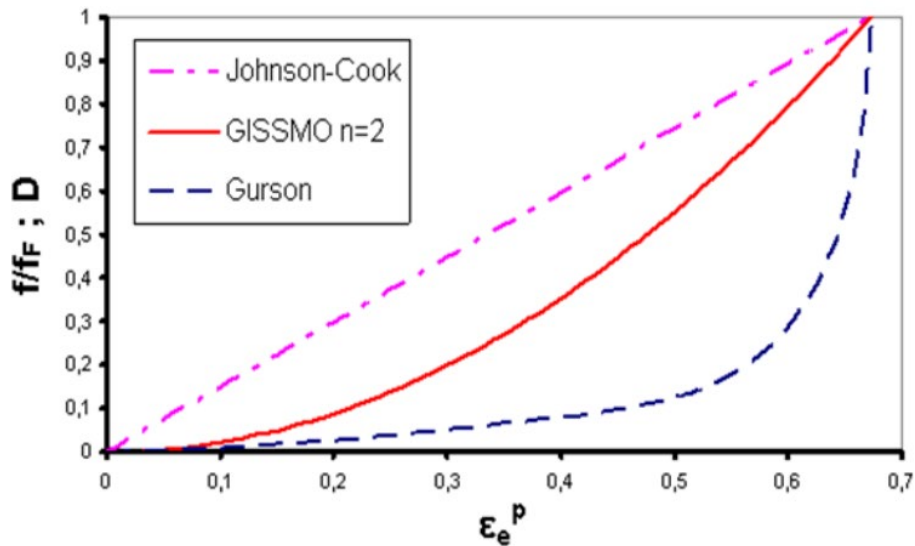


Figure 19 - Normalized damage accumulation [55].

A numerical model of a 22MnB5 axial crush rail was developed using the GISSMO damage model [63]. The fracture locus of 22MnB5 steel proved to be more conservative when model parameters were determined using the Nakazima [30] dome experiments compared to when they were obtained from V-Bend experimental data.

The fracture behavior of Usibor® 1500 was studied [56] and modeled using the GISSMO damage model. Usibor® 1500 specimens were quenched in three different ways so as to obtain microstructures that contained 100% martensite, 60% martensite and 40% bainite, and 100% bainite. Tests with stress triaxialities ranging from 0 (simple shear) to 2/3 (equal-biaxial tension) were carried out to obtain experimental fracture strains for each quench condition. Figure 20 shows the predicted and experimental fracture loci for the three different microstructures.

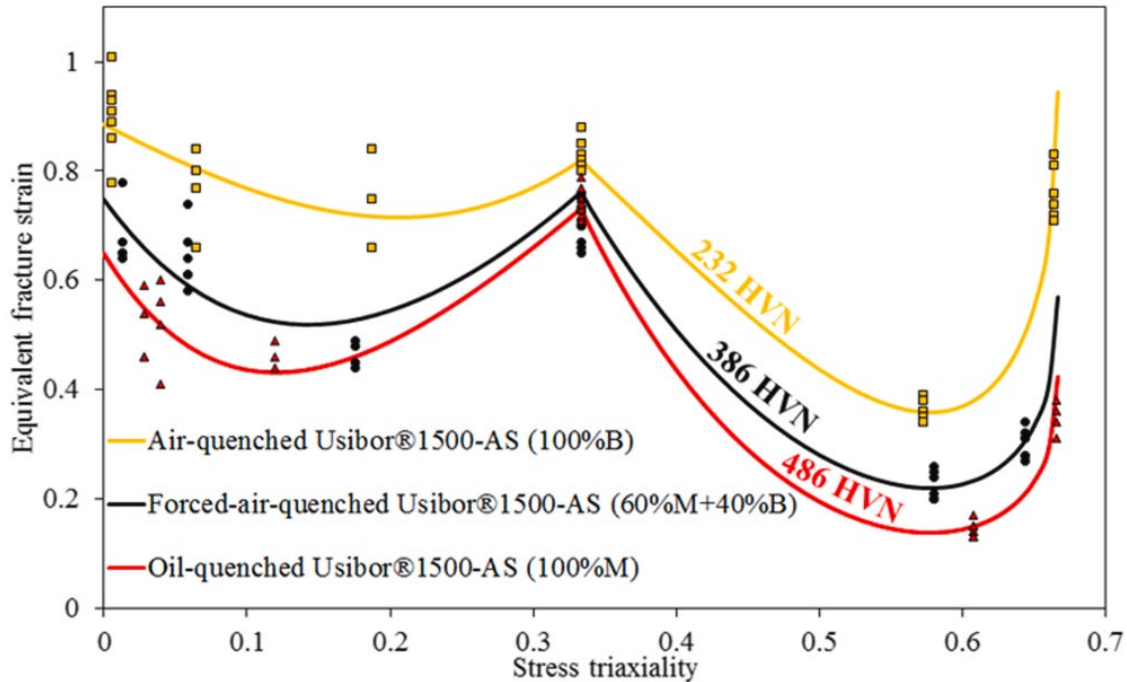


Figure 20 - The fracture loci of the different microstructures of Usibor® 1500-AS [56].

2.12 Research Objectives

The main objective of this work is to develop a dynamic, axial crush model for 1500 MPa PHS and 2000 MPa PHS. However, several objectives must first be studied to develop the numerical models:

1. The 1500 MPa PHS and 2000 MPa PHS must be heated and quenched at different cooling rates to produce specimens with a range of mechanical properties.
2. The hardness and phase volume fractions should be determined for each as-quenched condition that is produced.
3. The as-quenched specimens must be tested in uniaxial tension over a range of different strain rates to model the hardening behavior of the materials.

4. A material model must be created using fitted flow curves at different strain rates and hardness values.
5. Numerical models must be created to characterize the preload and axial crush for different channel tailoring conditions.

3. Mechanical Testing Methodology

3.1 Description of work

In this section, the methodology for characterizing the selected grades of steel will be described, not only in their as-received condition, but also after several different heating and cooling treatments. The chosen material must be characterized and studied to numerically model a dynamic impact. Arcelor Mittal Dofasco provided the press hardening boron steel. The sheet metal supplied for this work is 1500 MPa PHS (aluminized 22MnB5), which is 1.36 mm thick, and 2000 MPa PHS (aluminized 37MnB4), which is 1.4 mm thick. The sheet material is coated with an Al-Si layer to protect against oxidation during the quenching process. The chemical composition of the 1500 MPa PHS and the mechanical properties are shown in Tables 1 and 2. The chemical composition of the 2000 MPa PHS and the mechanical properties are shown in Tables 3 and 4.

| <i>Steel</i> | <i>Chemical Composition in wt. %</i> | | | | | | | | |
|---------------------|--------------------------------------|--------------|--------------|--------------|---------------|--------------|--------------|--------------|--------------|
| | <i>C</i> | <i>Si</i> | <i>Mn</i> | <i>P</i> | <i>S</i> | <i>Al</i> | <i>Cr</i> | <i>Cu</i> | <i>Mo</i> |
| <i>1500 MPa PHS</i> | <i>0.2332</i> | <i>0.23</i> | <i>1.18</i> | <i>0.012</i> | <i>0.002</i> | <i>0.046</i> | <i>0.20</i> | <i>0.012</i> | <i>0.005</i> |
| | <i>N</i> | <i>Ni</i> | <i>Nb</i> | <i>Ti</i> | <i>B</i> | <i>V</i> | <i>Ca</i> | | |
| | <i>0.0048</i> | <i>0.008</i> | <i>0.001</i> | <i>0.033</i> | <i>0.0033</i> | <i>0.004</i> | <i>0.002</i> | | |

Table 1 - Chemical composition in wt.% of 1500 MPa PHS provided by ArcelorMittal.

| <i>Steel</i> | <i>Mechanical Properties</i> | | |
|---------------------|------------------------------|-------------------------------|-----------------------|
| | <i>Yield Stress (MPa)</i> | <i>Tensile Strength (MPa)</i> | <i>Elongation (%)</i> |
| <i>1500 MPa PHS</i> | <i>417</i> | <i>610</i> | <i>23</i> |

Table 2 - Mechanical properties of 1500 MPa PHS provided by ArcelorMittal.

| <i>Steel</i> | <i>Chemical Composition in wt. %</i> | | | | | | | | |
|---------------------|--------------------------------------|--------------|--------------|--------------|---------------|--------------|---------------|--------------|--------------|
| | <i>C</i> | <i>Si</i> | <i>Mn</i> | <i>P</i> | <i>S</i> | <i>Al</i> | <i>Cr</i> | <i>Cu</i> | <i>Mo</i> |
| <i>2000 MPa PHS</i> | <i>0.3300</i> | <i>0.48</i> | <i>0.65</i> | <i>0.005</i> | <i>0.001</i> | <i>0.032</i> | <i>0.35</i> | <i>0.008</i> | <i>0.198</i> |
| | <i>N</i> | <i>Ni</i> | <i>Nb</i> | <i>Ti</i> | <i>B</i> | <i>V</i> | <i>Ca</i> | | |
| | <i>0.0019</i> | <i>0.412</i> | <i>0.047</i> | <i>0.025</i> | <i>0.0025</i> | <i>0.005</i> | <i>0.0003</i> | | |

Table 3 - Chemical composition in wt.% of 2000 MPa PHS provided by ArcelorMittal.

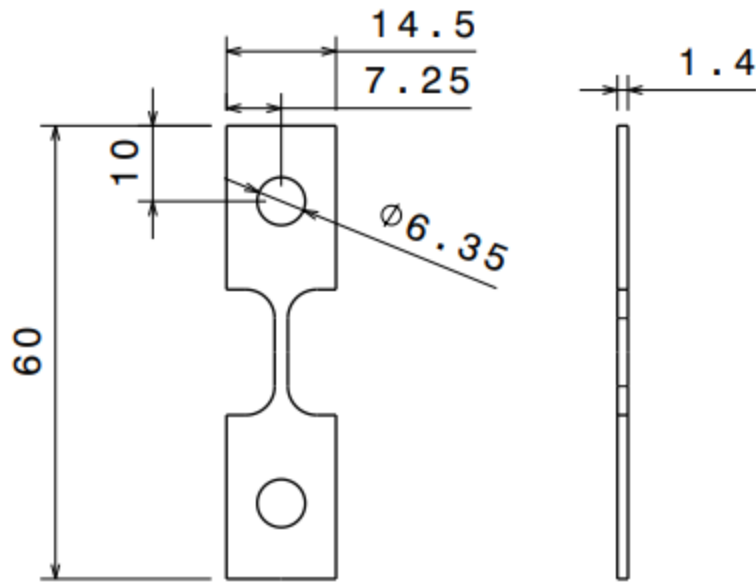
| <i>Steel</i> | <i>Mechanical Properties</i> | | |
|---------------------|------------------------------|-------------------------------|-----------------------|
| | <i>Yield Stress (MPa)</i> | <i>Tensile Strength (MPa)</i> | <i>Elongation (%)</i> |
| <i>2000 MPa PHS</i> | <i>532</i> | <i>686</i> | <i>21</i> |

Table 4 - Mechanical properties of 2000 MPa PHS provided by ArcelorMittal.

3.2 Specimen Preparation

3.2.1 Specimen Geometry

All tensile tests were done using the Mini Dogbone geometry to ensure consistency. The specimen geometry was chosen with a similar gauge section as Smerd et al. [72] and Thompson et al. [24]. The specimen geometry has a small gauge section to reduce ringing during high-rate testing and inertial effects during dynamic testing. Its geometry is also advantageous as it can be applied to a range of tensile tests at different strain rates since it deforms easily. The Mini Dogbone specimen has a reduced 9 mm gauge length to fit the split Hopkinson pressure bar. Wire EDM was used to cut all specimens due to its superior edge quality and accuracy for the thin Mini Dog Bone geometry.



Front view
Scale: 1:1

Figure 21 - Mini Dogbone Tensile Specimen (units in mm).

Similar miniature dogbone geometry has been compared to subsized ASTM specimens (at 0.003 s^{-1}). The comparison results are shown in Figure 22. The plotted stress versus strain curves agree and justify using the smaller miniature dogbone geometry for press hardening boron steel.

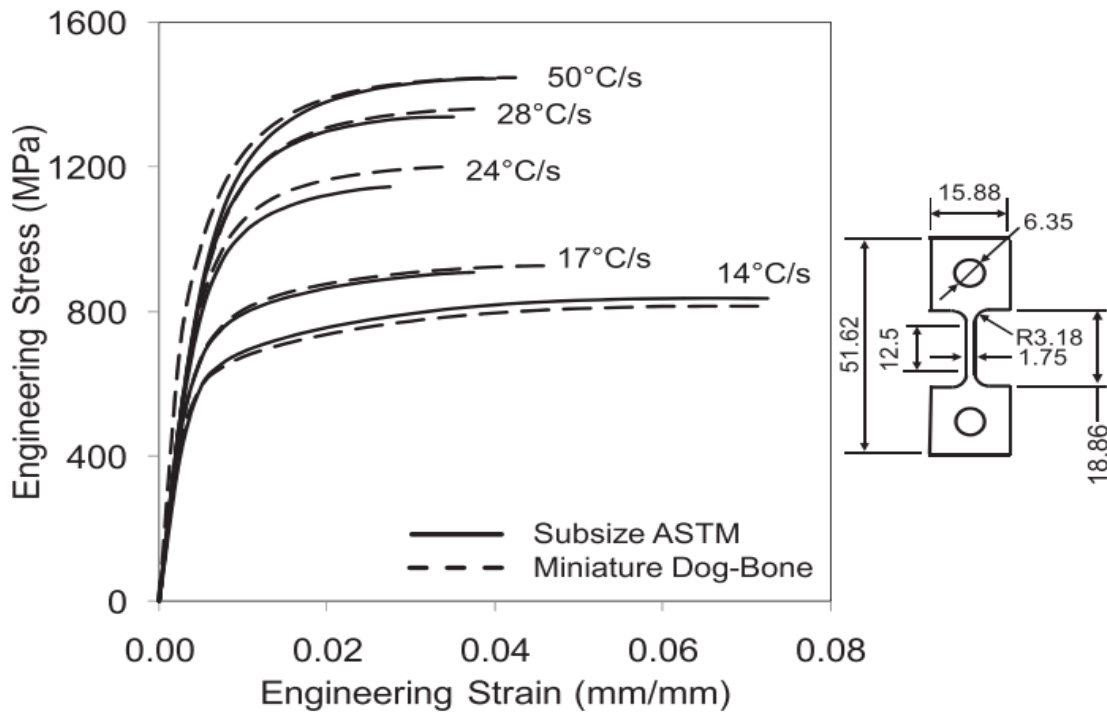


Figure 22 - Engineering stress versus strain curves (up to the UTS) of the miniature dog-bone and subsize ASTM specimens (at 0.003 s^{-1}) [25].

The quasi-static and split Hopkinson pressure bar tensile specimens do not have the hole in the gripping region shown in Figure 21. However, the intermediate rate tensile samples have a hole in the gripping region to ensure the specimen cannot slip during the test and to grip the specimen. In addition, the grips have been designed with a shoulder bolt to apply a clamping force and a contact force, at the hole, to minimize slippage.

Tensile specimens quenched using the flat quench die resulted in 4 different hardness values to cover the possible range of microstructures that hot stamping can produce. The four hardness levels cover the 1500 MPa PHS and 2000 MPa PHS microstructures from ferrite/pearlite to fully martensitic.

3.2.2 Heat Treatment of Steel Specimens

The blanks were fully austenitized at $930 \text{ }^\circ\text{C}$ by heating them in an electric furnace for 6 minutes, accounting for a 1-minute rise time and 5 minutes of holding time [4]. The austenitized blanks were then manually transferred to the preheated die set, allowed to cool for 5 minutes in this flat die. Once the specimen was removed from the flat die, it was allowed to cool at room temperature. Die temperatures of $20 \text{ }^\circ\text{C}$, $250 \text{ }^\circ\text{C}$, $350 \text{ }^\circ\text{C}$, and $550 \text{ }^\circ\text{C}$ were used to produce a range of microstructures that are realistic for

the forming die. When active heating is used, the forming die's temperature ranged between 250 °C and 500 °C. The forming die also can be operated at room temperature, so all possible microstructures are within the tested range.

Sheet specimens were heated and then quenched using a small die set made from H13 steel and heated in a furnace shown in Figure 23. A K-type thermocouple welded to the side was used to read the temperature of the die. In contrast, a separate K-type thermocouple was used to validate the displayed ambient temperature of the furnace.



Figure 23 - a) H13 quenching dies with K-type thermocouple. b) Quenching furnace.

The dimensions of the blanks were 100 mm x 200 mm sheets of 1500 MPa PHS and 2000 MPa PHS.

3.2.3 Specimen Hardness Testing

A two-part epoxy matrix was used to mount sheet specimens after heat-treating the PHS to create tensile coupons. First, the mounted specimens were ground and polished (shown in Figure 24) using the following Si-C paper: 220 grit, 400 grit, 600 grit, 800 grit, 1200 grit, then using polycrystalline diamond suspension fluid of 9 μm and then 1 μm .

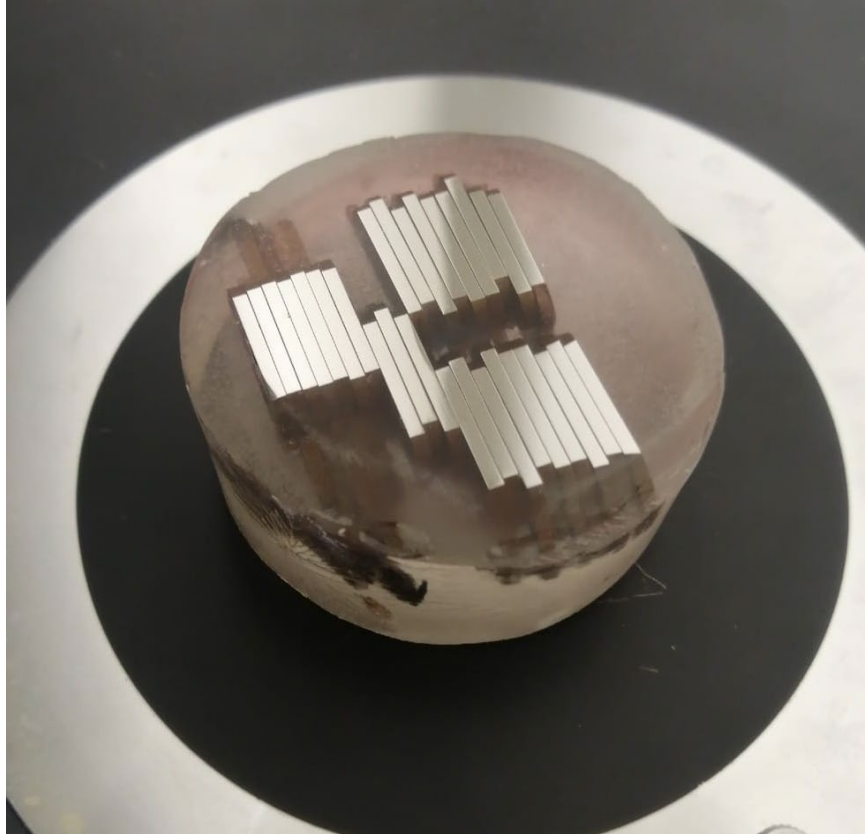


Figure 24 - Mounted hardness specimens in two-part epoxy.

The hardness of the mounted specimens was measured using a Buehler Micromet II Microhardness tester shown in Figure 25 calibrated to 1000g of applied load. The standard followed is the ASTM E92-17 for Vickers hardness. Hardness tests were repeated five times on each specimen and an average hardness value was calculated. For each test, the hardness was determined using the following formula:

$$HV = 1854.4 * \frac{F}{d_v^2} \quad (13)$$

- HV = Vickers Hardness
- F = Force (g)
- d_v = mean Vickers indentation diagonal length (μm)

The diagonal length of the indentation on the mounted specimens was measured using an Olympus GX-51 optical microscope at 20X magnification.

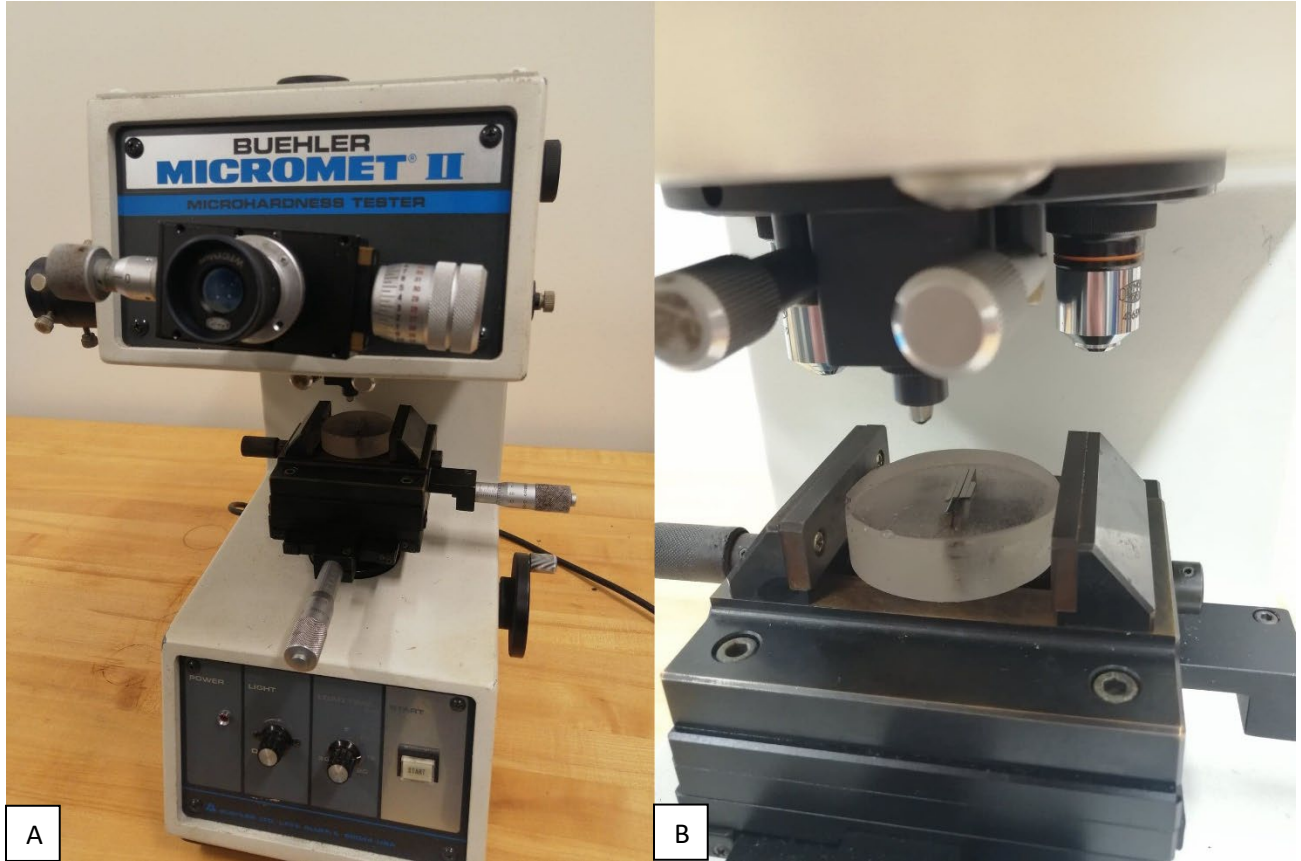


Figure 25 - a. Buehler Micromet II Microhardness tester. b. Mounted hardness specimen.

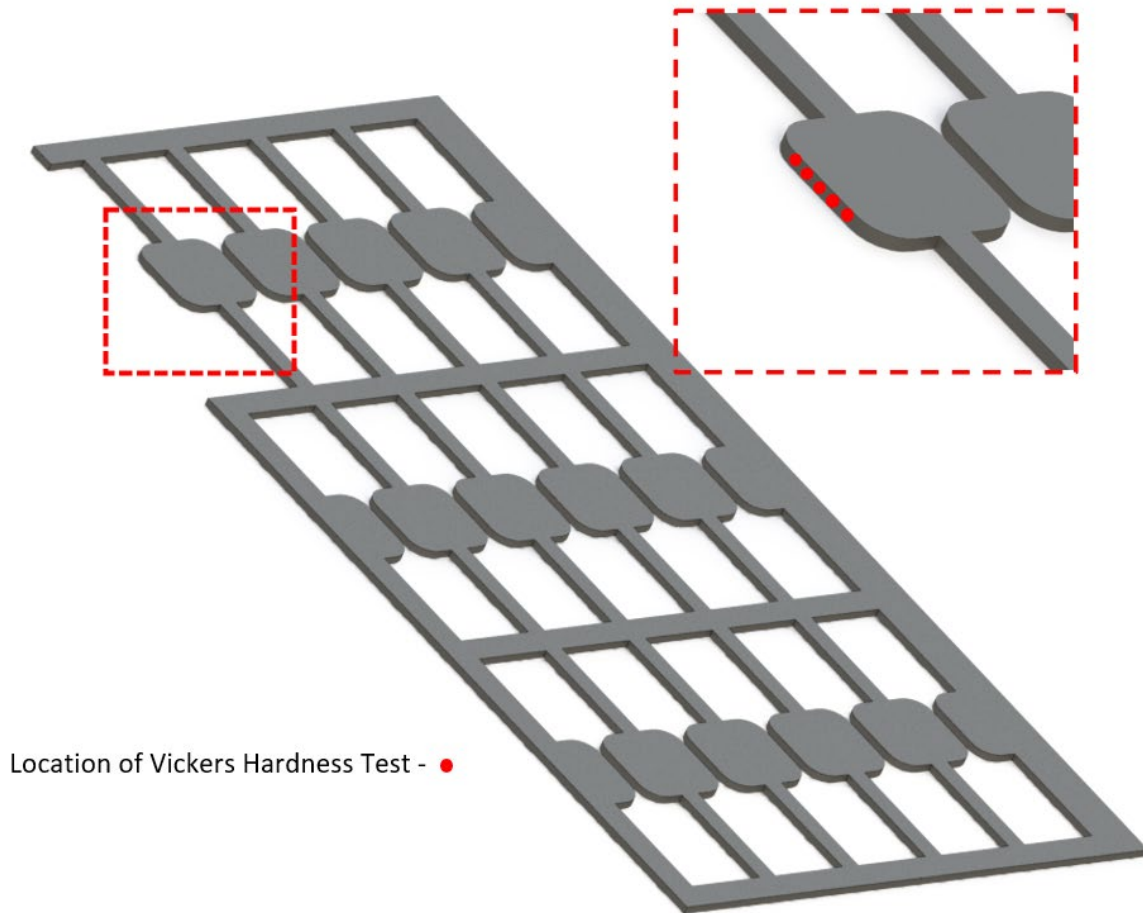


Figure 26 - Locations of Vickers hardness tests on tailored sheet.

3.3 Material Characterization

In choosing the tests to characterize the PHS materials, the logarithmic nature [24] of the strain rate effects of the metal was taken into consideration. Strain rates were chosen to be at least one order of magnitude greater than the last.

3.3.1 Quasi-Static Tensile Testing

Quasi-Static strain rates of 0.003 s^{-1} and 0.1 s^{-1} were chosen to characterize the hardening behaviour of the steel. An MTS Criterion series 43 electromechanical universal test system measured the engineering stress against the engineering strain for the mini dog bone specimens. The MTS Load is capable of a

maximum force of 30 kN and can be sampled at 5000 Hz. Load data was sampled at 10 Hz during the 0.003 s^{-1} strain rate test.



Figure 27 - MTS Criterion model 43 universal testing machine.

The 0.1 s^{-1} strain rate was sampled at 75 Hz and is limited by the speed of the MTS video extensometer. A black stochastic speckle pattern was applied to the surface of the tensile sample, which was tracked using an MTS digital image correlation camera.

Three repeat tensile tests were done at each microstructure and each strain rate to account for a range of hardened conditions of the 1500 MPa and 2000 MPa PHS.



Figure 28 - Quasi-static tensile testing with DIC camera.

3.3.2 Intermediate Rate Tensile Testing

A strain rate of 100 s^{-1} was achieved for the intermediate strain rate. The intermediate rate tensile testing apparatus (IRTTA) was used to deform the specimens with a high-speed video extensometer sampled at 225 kHz.

The IRTTA held the specimen in place between two plates. One plate was fixed to an impact barrier, and the other was impacted by the bullet fired by the pneumatic impactor. A PCB 224C load cell was mounted between the fixed plate and one side of the tensile sample grip. The load cell has an 8000 lbf tension range (overload limit: 10 000 lbf) with a sensitivity of 0.2 mV/lbf. The moving side of the grip is mounted to the plate using a needle bearing to reduce any radial alignment issues while the samples are loaded. In addition, a rubber damper was implemented to reduce ringing in the system to improve the signal quality.

The IRTTA uses linear bearings to reduce the system's twisting and ensure the tensile sample was deformed uniaxially.



Figure 29 - Intermediate rate tensile testing apparatus with mini dogbone specimen.

A laser displacement transducer triggered the data acquisition system when the pneumatic projectile passed through the beam. Next, a second laser displacement transducer was used to estimate the IRTTA crosshead position. The IRTTA crosshead position was used to estimate the velocity of the pneumatic accelerator projectile so that a specific strain rate can be targeted. Figure 30 shows the strain rates achieved using a series of tests at different tank pressures. Equation 14 was created by fitting a cubic polynomial to the data.

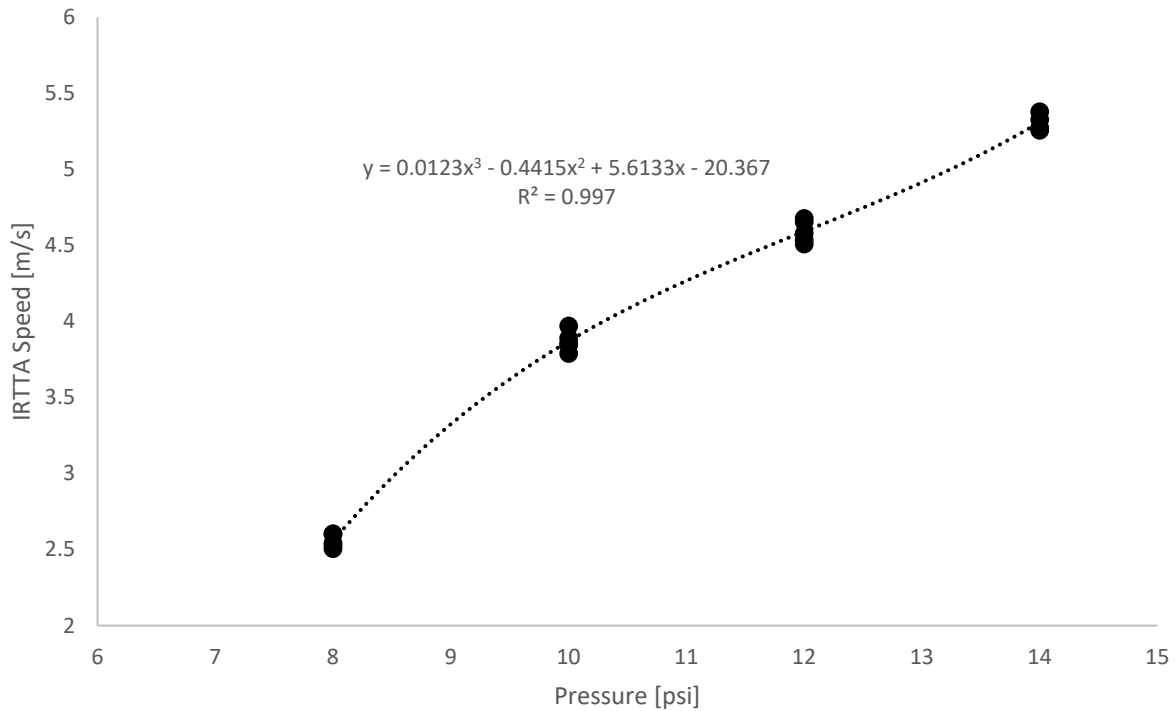


Figure 30 - IRTTA speed versus air tank pressure.

$$y = 0.0123x^3 - 0.4415x^2 + 5.6133x - 20.367 \quad (14)$$

Using a gauge length of 9 mm, a strain rate of 100 s^{-1} corresponds to a projectile speed of 0.9 m/s. Using Equation 14, a tank pressure of 6.54 psi corresponds to a strain rate of 100 s^{-1} . The strain rate was predicted using numerical simulation and validated during the experiments. A Photron SA4 High-speed camera was used to measure the strain on the specimen by using the MTS digital image correlation system to track a white stochastic speckle pattern applied on the tensile sample's surface. Lightweight grips shown in Figure 31 were designed using P20 tool steel and cut using a wire EDM with a 1.40 mm slot that holds the tensile specimen. A 6.35 mm (0.25 in) diameter shoulder bolt was inserted into the grip to fasten and tension the specimen.

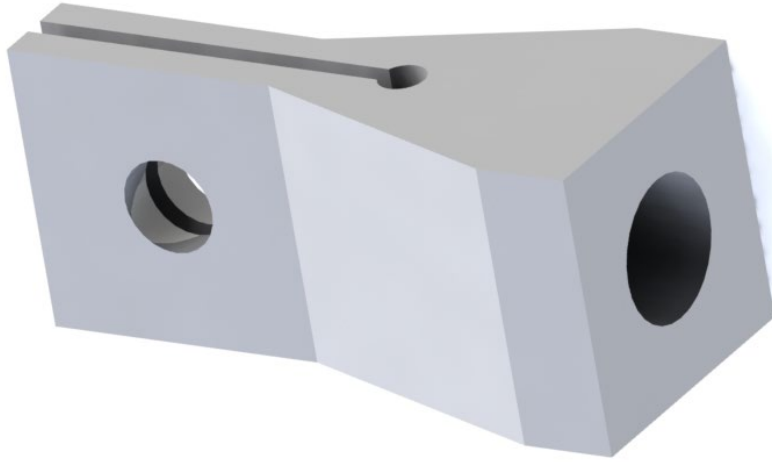


Figure 31 - IRTTA mini dogbone grips.

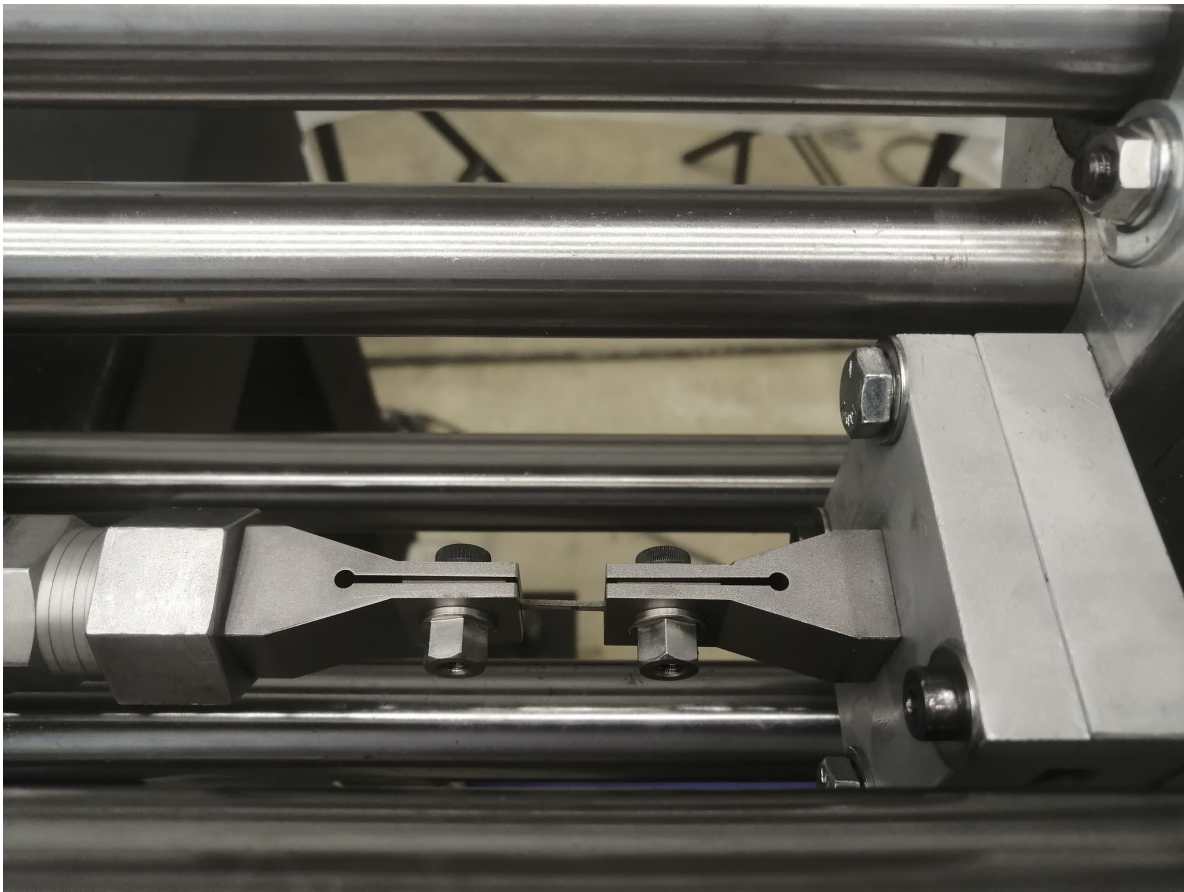


Figure 32 - Mounted IRTTA grips with mini dogbone specimen.

3.3.3 High Strain Rate Tensile Testing

For the high strain rate tensile testing, a strain rate of 1500 s^{-1} was chosen. This strain rate was achieved using the split Hopkinson bar. The split Hopkinson bar is dynamically loaded using a hollow striker bar around an incident bar to impart a tensile force through a test specimen. The striker bar impacts the end of the incident bar using an anvil attached to the end of the incident bar, shown in Figure 33.



Figure 33 - Split Hopkinson pressure bar testing setup.

The pressure of the gas gun controls the speed that the striker bar moves and the strain rate of the test specimen. The momentum trap at the end of the split bar is used to dissipate the system's energy safely.

1500 MPa PHS and 2000 MPa PHS pose challenges when testing at high strain rates that make gripping the specimens difficult. A Vickers hardness above 550 HV is standard for tensile specimens with a martensitic microstructure, leading to significant wear on serrated grips. Wear on the grips limits the amount of testing that can be done and, more importantly, initiates slipping during testing. The slipping affects the load cell data in high-rate tests and is responsible for under-calculated stress values. Two methods were implemented to reduce the wear on the grips and improve the quality of the testing.

The first change to the grips was machining new wedge inserts specially heat-treated to a hardness greater than 700 HV. The wedges were manufactured starting with unhardened, O1 tool steel and roughly

machining them. The roughly machined wedges were then fully hardened and finished using a wire EDM. Roughing in the wedges helps ensure the serrations are not tempered when they are manufactured so that they remain fully hardened. The wedge design is shown in Figure 34.

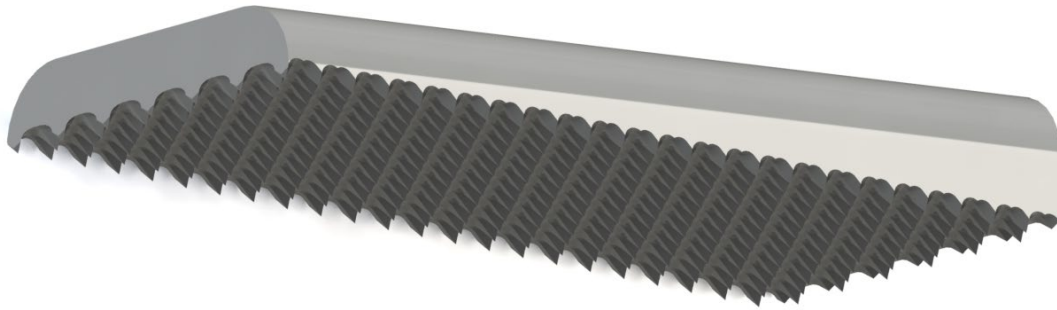


Figure 34 - Split Hopkinson pressure bar modified grip wedge.

The second change was to the tensile samples. Tensile samples were submerged in water, as shown in Figure 35. A propylene gas torch was used to heat the exposed gripping section for 300 seconds for each gripping side. Using this heating method, the gripping section could be tempered to a bainitic microstructure while maintaining its original microstructure for the gauge section. Since the gauge section was submerged in water, the temperature remained below 100 °C.

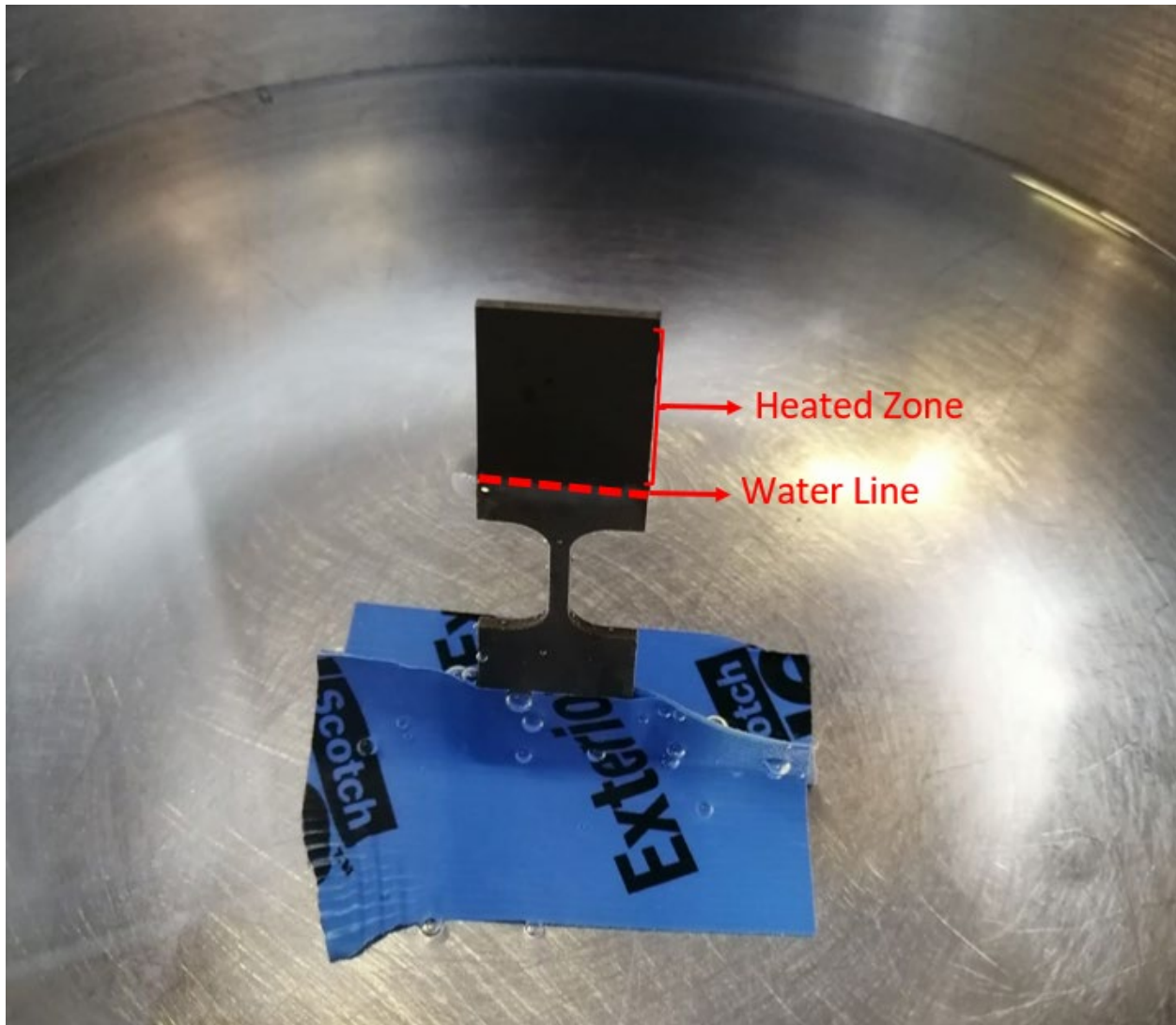


Figure 35 - Split Hopkinson bar specimen grip tailoring procedure.

A destructive test was performed on the tensile samples to ensure that the heat treatment did not affect the gauge section. The gauge section was cut off from the gripping section, and the parts were mounted in two-part epoxy along with an un-tempered tensile specimen. The Vickers hardness was tested every 1 mm for both specimens and compared against each other.

The specimen was mounted using a fixture that holds the grips and the sample in the desired orientation while the grips are tightened using threaded rods. The specimen and the grips were moved to a hydraulic press where each side received 10000 kgf individually to preload the grips. The preload improved the response of the testing and eliminated slipping. The mounting fixture is shown in Figure 36. After preloading the grips, the specimen was mounted in the mounting fixture again to avoid being damaged

as it was threaded between the incident bar and the transmission bar. The final mounted specimen is shown in Figure 37.



Figure 36 - Split Hopkinson specimen mounting fixture.

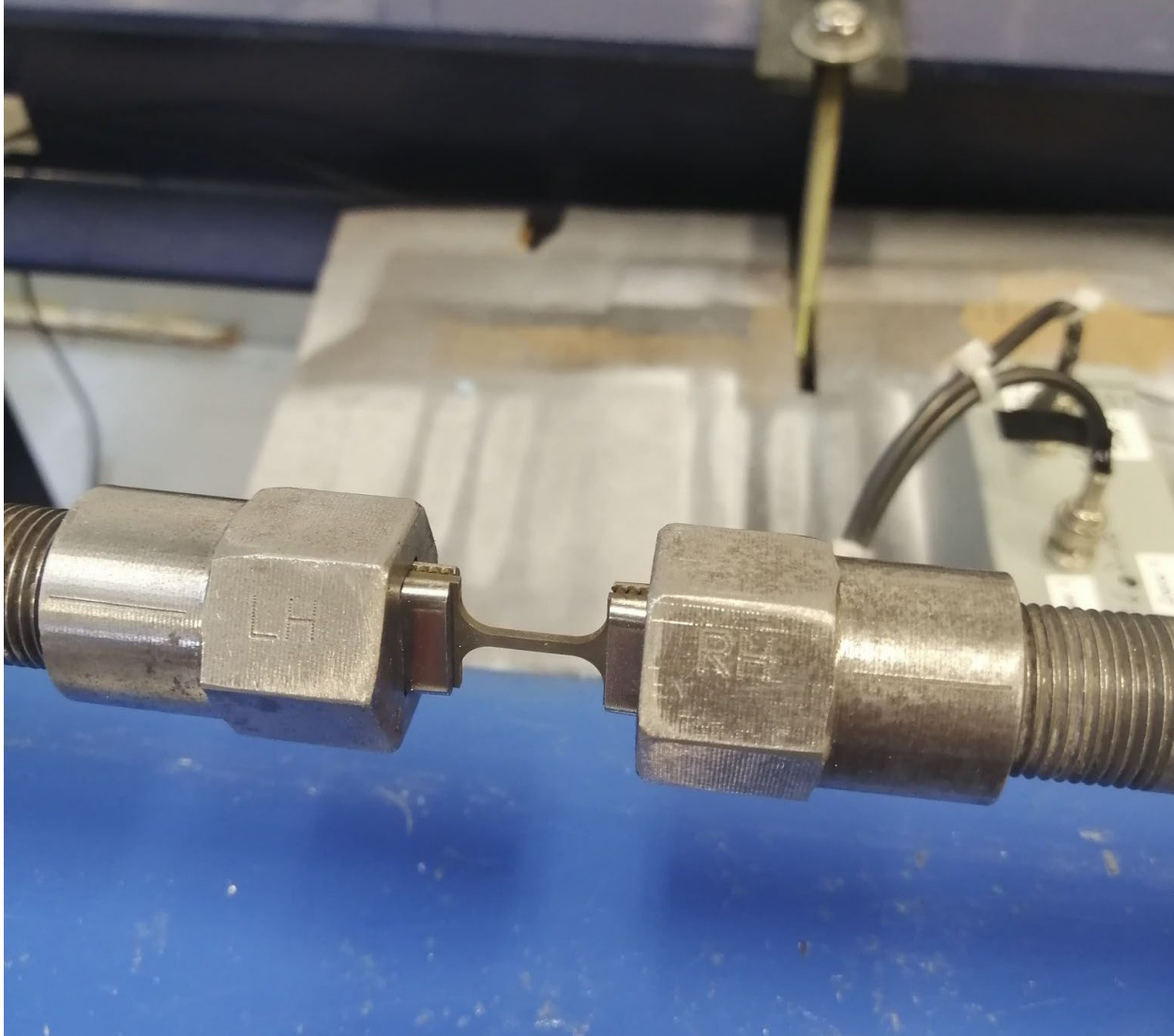


Figure 37 - Split Hopkinson pressure bar with the mounted specimen.

Two strain gauges were attached using OMEGA® TT300 cement 2-part epoxy adhesive on each bar. The glue used to attach the strain gauges is left to air dry for 15 minutes before placing the strain gauge on the bar, then was heated initially at a rate of 10 °C per second until it reached 150 °C. The gauges were kept at 150 °C and monitored using a K-type thermocouple for 120 minutes. This method of gluing the strain gauges created a stiffer response compared to using cyanoacrylate glue and lasted for approximately 3 times the number of tests.

A calibrated linear load cell was mounted inline to the split Hopkinson bar to calibrate the strain gauges. The bars were gradually loaded using the hydraulic pump, and the strain gauge voltage against the load cell load is used to calculate a calibration coefficient. The ratio of strain measured from the strain gauges

to the calculated strain from the load cell gives a calibration to ensure the output of the strain gauges are validated.

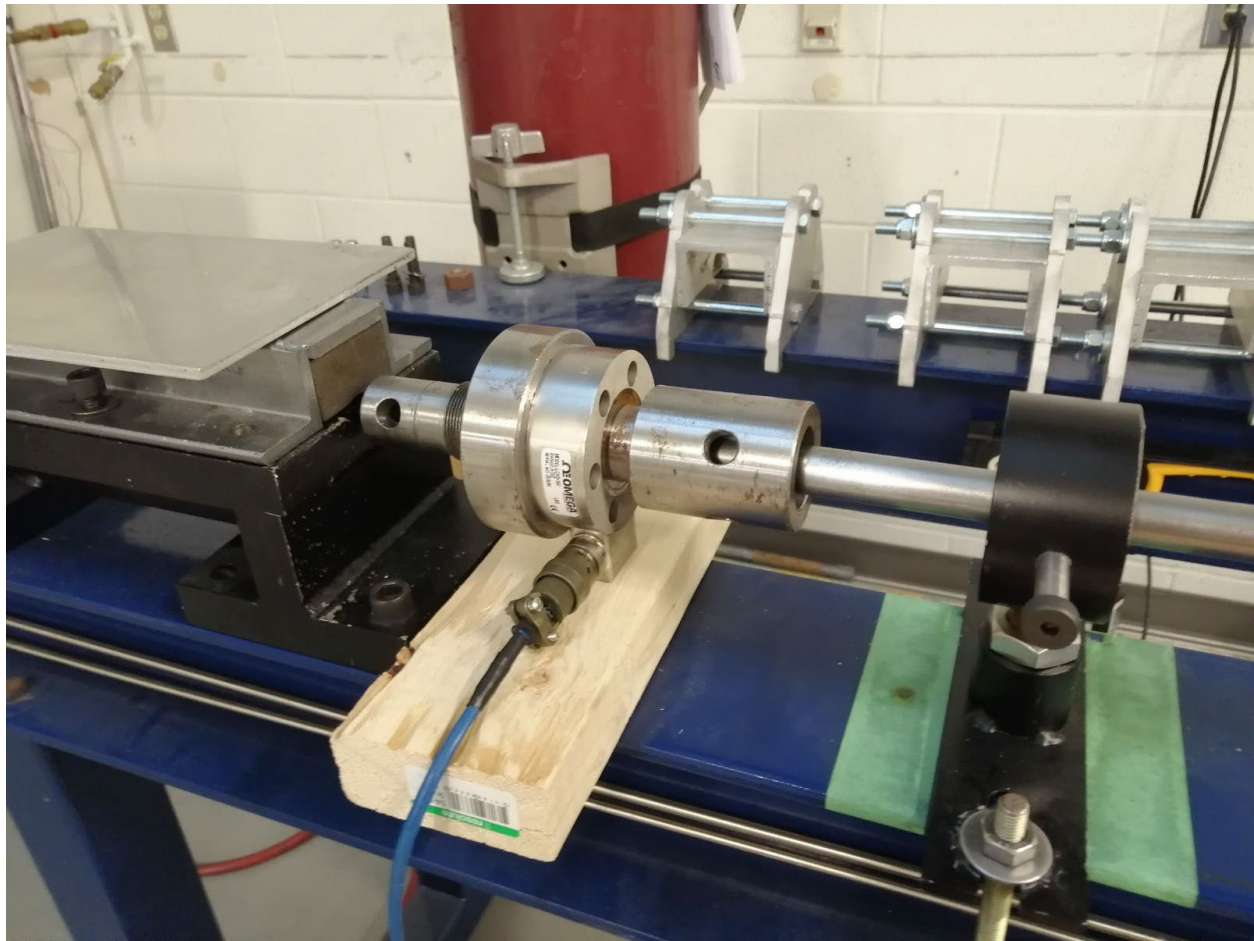


Figure 38 - Split Hopkinson bar load cell calibration.

3.4 Extended flow curves

The recorded stress-strain behavior is valid up to the ultimate stress value for each strain rate. In LS-DYNA, the extended portion of the flow curves is calculated using the slope of the last two data points in the effective plastic strain and true stress table. In this work, the last two points were calibrated using extended flow curves so that the large deformation hardening rate would be accurate. sheet specimens were therefore prestrained by cold rolling then loaded in uniaxial tension to obtain extended flow curves.

A fully bainitic microstructure can be cold rolled to the desired level, so the 1500 MPa PHS and the 2000 MPa PHS were tailored by quenching using heated dies at 550 °C. A large strain domain needs to be covered for a crash scenario, so pre-strain values of 25%, 50%, and 75% were targeted. Pre-strain values were targeted using equation 15:

$$\varepsilon_{\text{pre}} = \sqrt{\frac{2}{3}[\varepsilon_T^2 + (-\varepsilon_T)^2]} = \frac{2}{\sqrt{3}}|\varepsilon_T| \quad (15)$$

Using equation 15 thickness values corresponding to the targeted values were calculated and shown in Table 5.

| <i>Strain</i> | <i>Thickness (mm)</i> | <i>Thickness (mm)</i> |
|---------------|-----------------------|-----------------------|
| <i>0</i> | <i>1.4</i> | <i>1.36</i> |
| <i>0.25</i> | <i>1.127458</i> | <i>1.087192</i> |
| <i>0.5</i> | <i>0.907973</i> | <i>0.875546</i> |
| <i>0.75</i> | <i>0.731216</i> | <i>0.705101</i> |

Table 5 – Thickness of tensile specimens for targeted pre-strain values.

After reaching the targeted strain, the rolled samples were cut to the mini dog bone geometry using a wire EDM. The tensile samples were then tested at a strain rate of 0.003 s^{-1} using a 50 kN MTS universal testing machine with digital image correlation to calculate the strain.

3.5 Determination of Work Hardening Model

A Voce hardening function was assessed for the 1500 MPa PHS and the 2000 MPa PHS. Sarraf [67][65] found the Voce hardening function was an effective choice when considering flow curves such as boron steel. The hardening parameters are calculated using nonlinear regression.

The goodness of fit metrics used are:

- Normalized and relative mean square
- Pearson's chi-square test
- R-squared and Adjusted R-squared values

The R-squared value was the most widely used goodness of fit metric throughout the work and is defined as:

$$R^2 = 1 - \frac{\sum_{i=1}^n (\sigma - \hat{\sigma})^2}{\sum_{i=1}^n (\sigma - \bar{\sigma})^2} \quad (16)$$

- σ = experimental stress (MPa)
- $\hat{\sigma}$ = predicted stress (MPa)
- $\bar{\sigma}$ = mean stress (MPa)

3.6 Description of Hot Stamping Channel Die

The hot stamping die was used to produce channel sections that can be subjected to impact. These channel sections are analogous to a generic automotive structural component such as a front rail.

The channel die uses 3 separately heated and cooled zones equally spaced along the length of the channel (Figure 39). Each zone has the option to be heated using heating elements inserted into the sections of the die set and controlled using built-in thermocouples. An external chiller cools each of the zones separately. The chiller cannot be run simultaneously as a heating element in each zone.

The temperature controls added to the die allow the production of channel sections that have different mechanical properties along the channel. It is also possible to produce channels with similar properties for repeat testing. The three zones of the channel die have the same length, which makes it possible for the middle zone to be a long transition zone between a soft zone (quenched slowly using the heating elements) and the hard zone (keeping the zone at room temperature). The gradient of microstructures and corresponding mechanical properties along the length of the transition zone will allow verification of numerical models that predict the as-quenched properties along the hot stamped channel section.



Figure 39 - Hot stamping channel die (front view).



Figure 40 - Hot stamping channel die (side view).

3.7 Channel Spot Welding

Spot welding is required to create channel sections out of two hat sections so that the steels crash performance can be analyzed.

3.7.1 Determination of Spot-Welding Parameters

The tailoring of boron steel creates a unique set of welding challenges. The weld parameters change along the length of the channel due to the changing microstructure. The channel die can be controlled from room temperature to 550 °C, so the range of hardness produced by the material can be associated with optimal weld parameters. Weld parameters were determined by modifying the weld schedule and using destructive coupon testing simultaneously on each material and microstructure. The welds were tested using two 50 mm x 100 mm coupons. The coupons were welded together then, using the ISO 10447 standard [73] for chisel-testing resistance spot welds. The welding parameter is deemed acceptable once

the average nugget diameter is consistently greater than 5 mm regardless of the quenching rate and consequent microstructure that may have developed in the flanges of a tailored channel.

3.8 Axial Crush Fixture

To achieve repeatable and safe impact testing, there was a need to properly constrain one end of the channels to the crash barrier. The axial crush fixture needed to be substantial enough to ensure an axial crushing that can be simulated using the assumption that the part is rigidly clamped. However, the fixture also needs to be as light as possible to reduce the clamp's inertial effects on the load cells.

The fixture uses four Dytran 1210V7 ring style IEPE force sensors with a 0.05 mV/lb sensitivity. The load cells were mounted using custom machined, slippery UHMW polyethylene rings. The rings were added to the fixture to position the force sensors concentrically around the 19.05 mm (0.75 in) socket head screws with fine threads (16 per inch) that preloaded the force sensors. A torque bar applied the preload of 126 ft-lbs using the ASTM A307 standard for clamp load of grade A fasteners. The torque is calculated using:

$$T = KdP \tag{17}$$
$$T = 0.20 * 0.0625 \text{ in} * 10070 \text{ lbs}$$
$$T = 126 \text{ ft} - \text{lbs}$$

- T = torque
- K = torque coefficient (dimensionless)
- d = nominal diameter (inches)
- P = bolt clamp load (lb)

The fixture utilizes clamping rings to fix the crush rail to the internal boss, and a combination of machine screws and shoulder bolts shown in Figure 42 locate and constrain the parts together. The clamp blocks were secured using a slotted shoulder bolt to constrain them when fully compressed with the clamping rings. The bolts constrained the blocks to slide and rotate on the impact plate while the clamp rings secure the channel and clamp blocks around the inner boss.

The fixture is made from 4140 steel for its machinability and ability to be oil-hardened. All parts in contact with the channel were heat-treated to a hardness of 58 HRC.

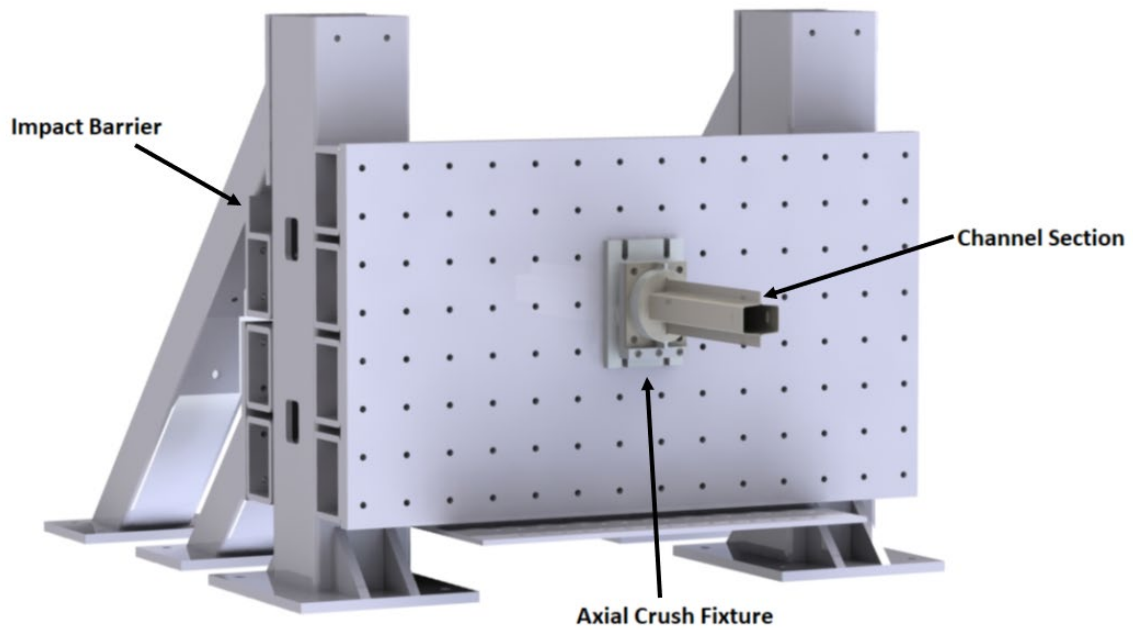


Figure 41 - Axial crush fixture with channel mounted to impact barrier.

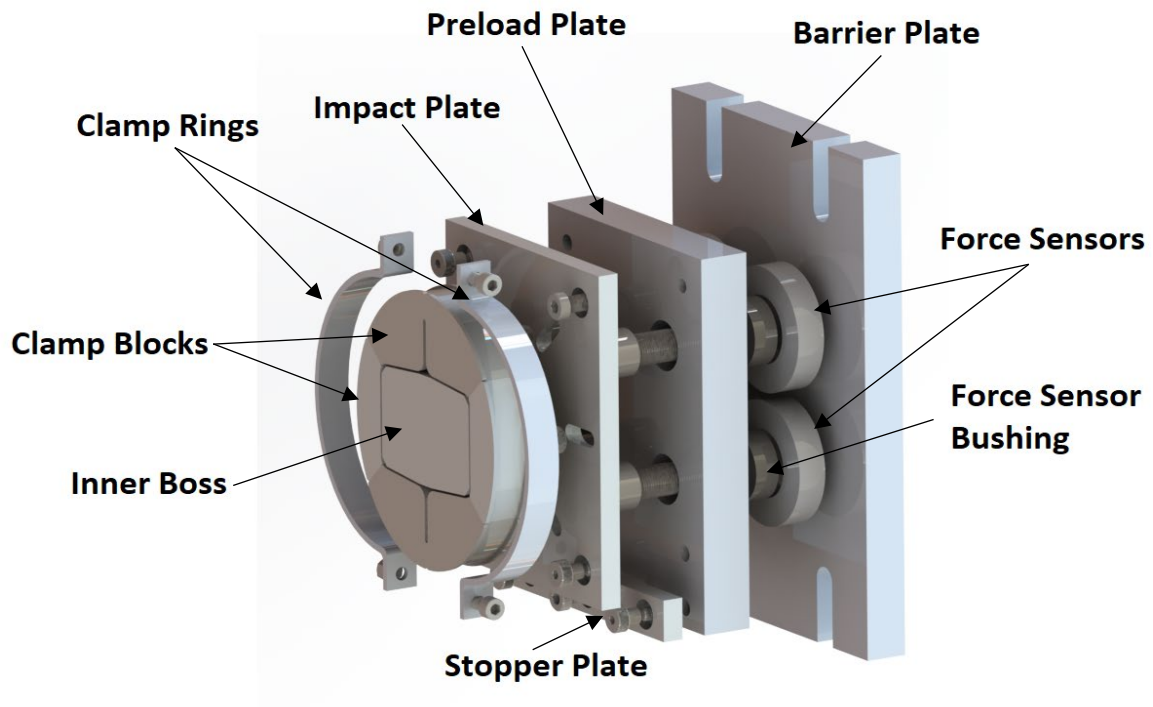


Figure 42 - Detailed axial crush fixture.

The assembly has a removable section (Figure 43) designed to improve the ease of repeat testing. The channel section can be clamped and unclamped from the removable section without the need to remove the fixture from the impact barrier. The removable section is positioned to the preload plate using machine screws and shoulder bolts for two points of four-way positioning. The stopper plate was included to improve the ease of installation by giving the removable section a positioned lip to rest on as it is fastened.

The purpose of the preload plate is to preload the load cell prior to impact. For each Dytran 1210V7 load cell, a preload of 8.9 kN is required.

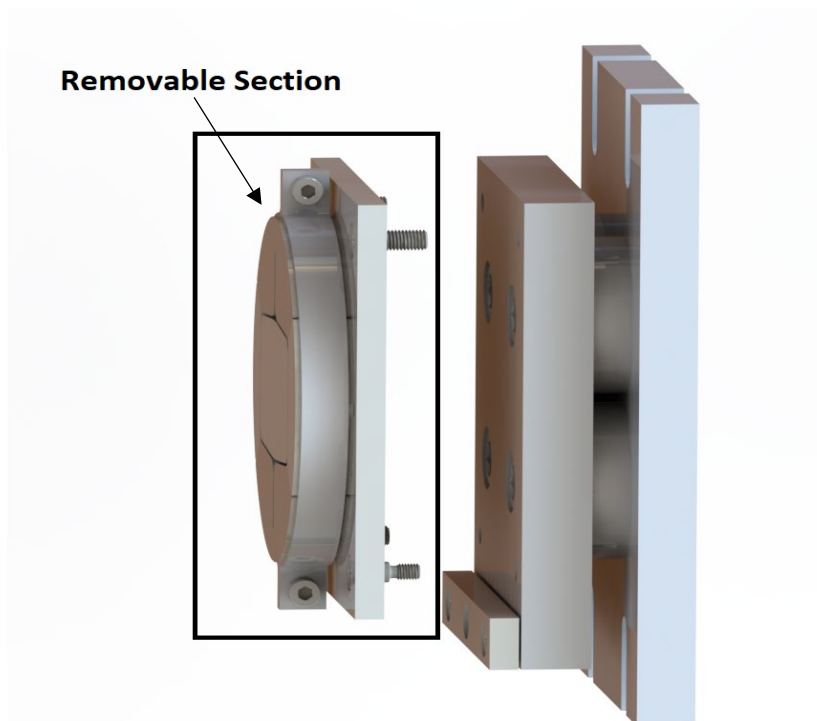


Figure 43 - Removable section of axial crush fixture.

4. Numerical Simulation Models

This chapter describes the approach used to model the experiments. All numerical modeling was performed using LS-DYNA R10.0. The models were pre-processed using LS-PrePost.

4.1 Uniaxial Tensile Test Numerical Model

To study the material models' accuracy and validate the experimental work, uniaxial tensile tests were simulated using LS-DYNA. The specimens used in the numerical model are shown in Figure 44. The specimen uses the same geometry as the mini dog bone tensile specimen without the hole in the gripping region. A half geometry that was cut parallel to the loading direction was used to reduce computational time in each simulation. Quarter geometry was not used as the same numerical model was used for each strain rate with minor adjustments and the dynamic models experience a different force equilibrium with respect to the two gripping regions, so both must be considered.

The numerical models were modeled with 8 node hexahedron solid elements with a size of 0.25 mm by 0.25 mm by 0.25 mm. The elements use a 8 point hexahedron selectively reduced integrated brick formulation (element formulation 2 in LS-DYNA) to remove volume locking and hourglass stabilization issues.

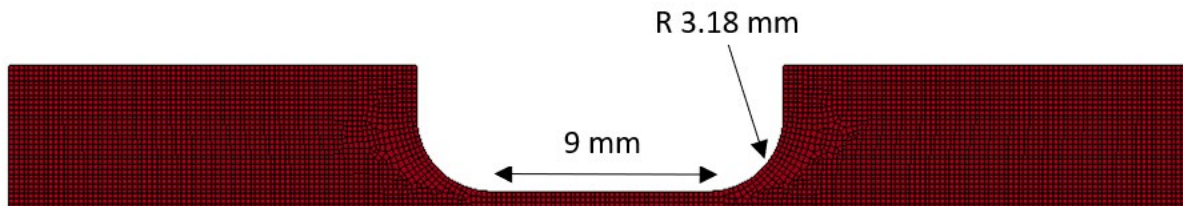


Figure 44 - Mini dogbone FEA mesh (half geometry).

The material model used is implemented in LS-DYNA as *MAT_24_PIECEWISE_LINEAR_PLASTICITY_LOG_INTERPOLATION. MAT_24 allows for the input of tabular data in the form of effective stress versus effective plastic strain to input a load curve. Multiple strain rates were defined for each material to account for rate effects. The logarithmic interpolation was selected as the strain rate effects of 1500 MPa PHS was found to be logarithmic [27]. Figure 45 shows a schematic [46] of how multiple material strain rates were incorporated into a single table. Curves 1 through 5 are inputs to the material model with different strain rates. The numerical solver interpolates logarithmically between the inputted flow curves.

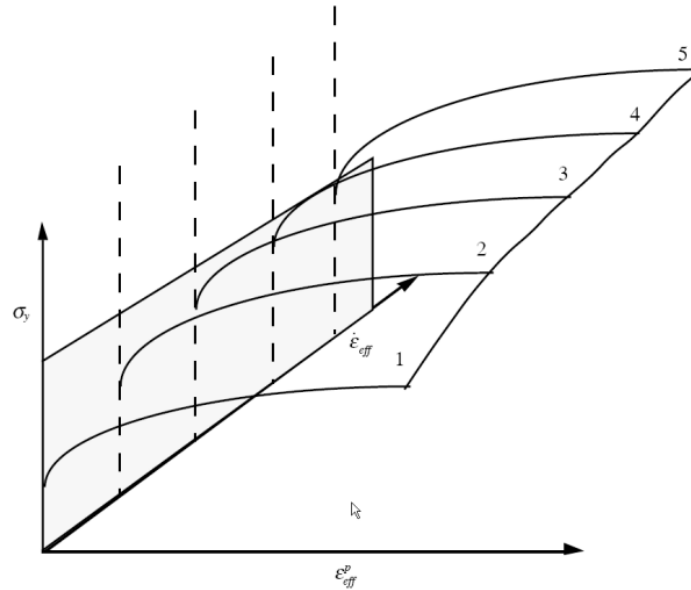


Figure 45 - Strain rate logarithmic interpolation [46].

4.1.1 Boundary Condition of Uniaxial Numerical Model

The first boundary condition was applied to the nodes along the longitudinal line of symmetry to prevent any nodal displacement perpendicular to it. The symmetry reduced computational time. The second boundary condition fully constrained the nodes from any translational or rotational motion. The boundary condition was used to model the fixed end of the grips. Lastly the third boundary condition imparted a constant velocity on the moving grip. The velocity was calculated from the experimental tests.

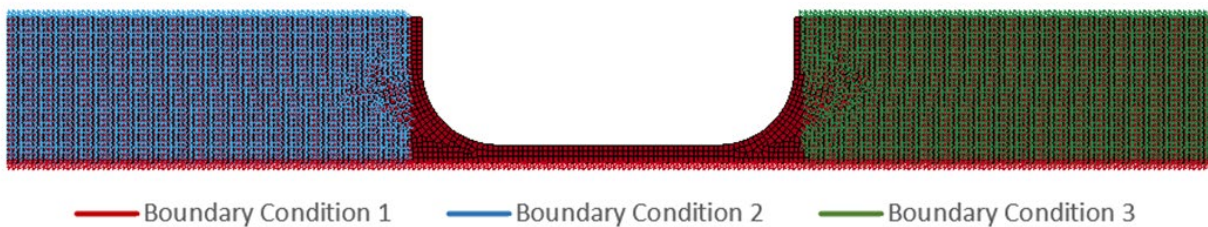


Figure 46 - Mini dogbone boundary conditions.

4.2 Channel Clamping Model

Modeling the axial crush experiments consisted of a two-stage simulation. The first stage involved clamping the crush channel into the fixture. The second stage simulated the dynamic crush. The clamp was modeled using six external clamp blocks situated around an internal boss, shown in Figure 47. All the parts shown in Figure 47 were modeled using 8 node hexahedron solid elements with an elastic material

model. The material properties of the steel that were required for the simulations are displayed in Table 6. All solid elements were modeled using selectively reduced integrated brick formulation (element formulation 2 in LS-DYNA). The clamp blocks were modeled using 2 mm tetrahedral elements, and the inner boss was modeled using 8 node hexahedron solid elements with a size of 2.5 mm by 2.5 mm by 2.5 mm. An implicit time integration scheme was utilized in the clamping model. The elements associated with the channel were 2.5 mm fully integrated shell formulation with 7 through-thickness integration points. The fold initiator was created by deleting 4 rows of 12 elements 55 mm from the impacted end of the channel section (Figure 49).

The clamping numerical model was remade to accommodate the thicker 2000 MPa PHS. The clamping blocks were translated 0.04 mm radially outward from the channel. The inner boss had no change as the nature of the hot stamping forming press only changes the outside geometry of the channel when a thicker material is used.

| <i>Property</i> | <i>Value</i> |
|------------------------|------------------------------|
| <i>Density</i> | <i>7890 kg/m³</i> |
| <i>Elastic Modulus</i> | <i>200 GPa</i> |
| <i>Poisson's Ratio</i> | <i>0.3</i> |

Table 6 – Properties of steel [74].

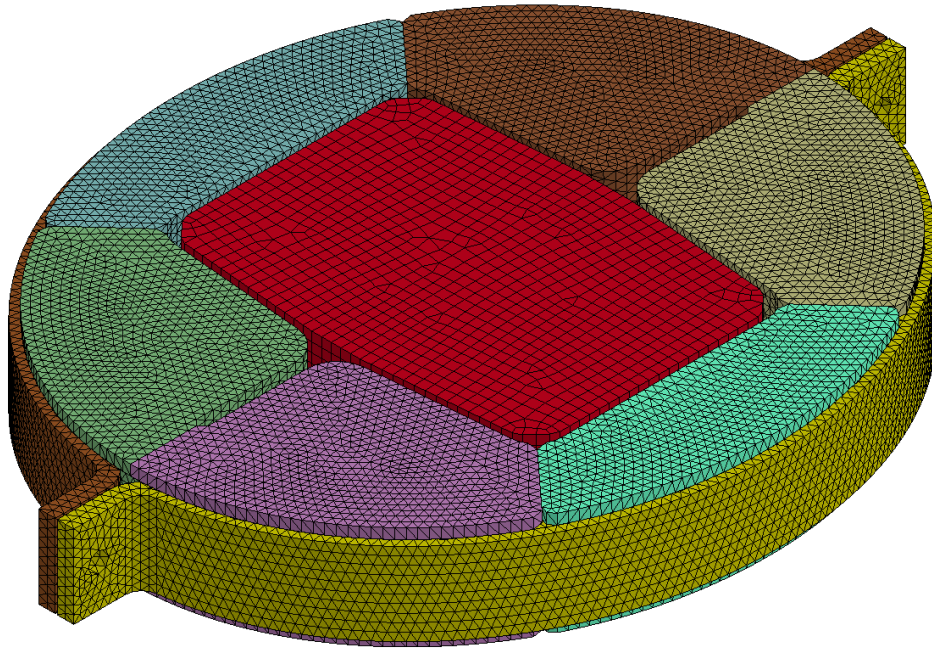


Figure 47 - Meshed clamping fixture for a double hat channel section.

The channel section was added to the clamping simulations by meshing the predicted hat section using 2.5 mm by 2.5 mm deformable quadrilateral shell elements. Next, the elements for the fold initiator were deleted. The geometry to form the channel section was then reflected and material properties were assigned. Lastly, Beam elements were created between nodes on the flanges

4.2.2 Spot Weld Model

The channels were constrained together using spot welds modeled as beam elements using the standard elastic properties of steel taken from [74] and shown in Table 6. The material model used was the *MAT_SPOTWELD option within LS-DYNA. The provided diameter was 5 mm from the weld testing with Marwood International. Spot welds were located every 25 mm along the centre of each flange and down the full length of the channel sections (shown in Figure 48). A failure criterion for the spot welds was not included. The contact between the spotwelds and the channel was created using the tied contact algorithm in LS-DYNA.

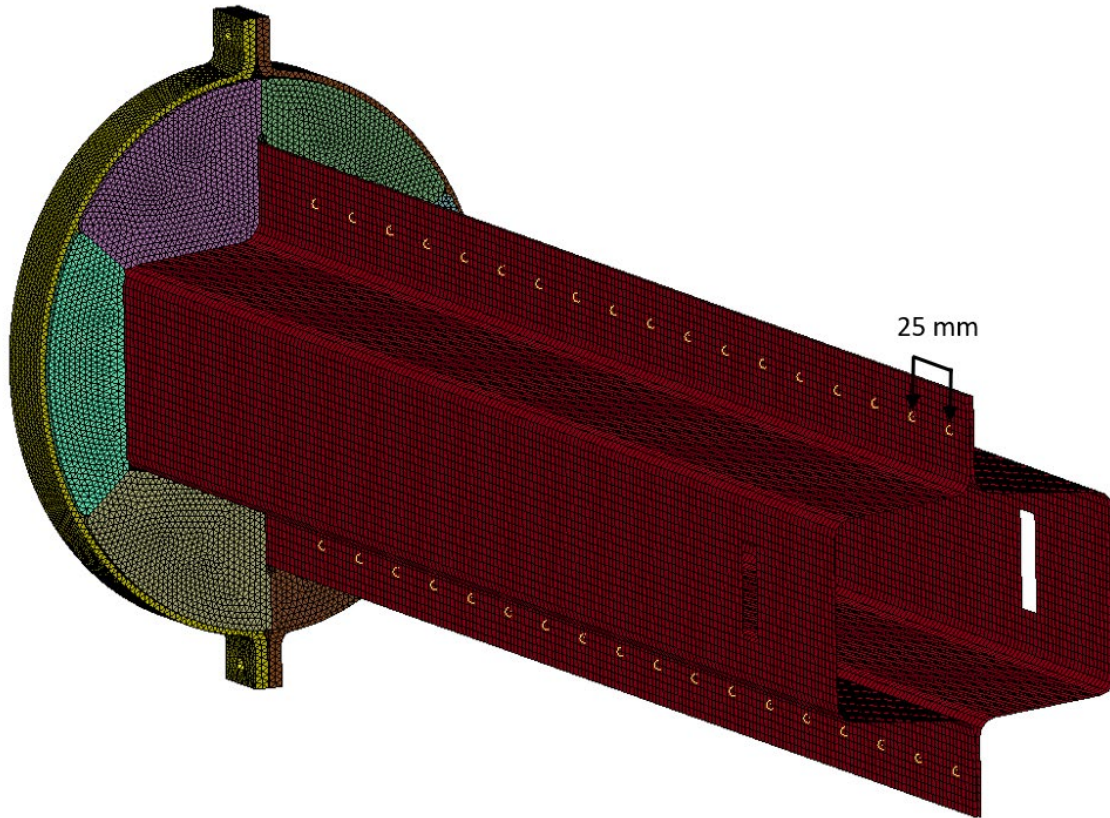


Figure 48 - Numerical model of the welded double-hat channel sections mounted in the clamp.

Two semi-circular clamp rings applied a preload to the system during the simulation by simulating a 0.25 mm displacement to the tabs of the clamp ring shown in Figure 49. This displacement simulated a preload applied to the experimental system by tightening the machine screws in the clamp ring flanges.

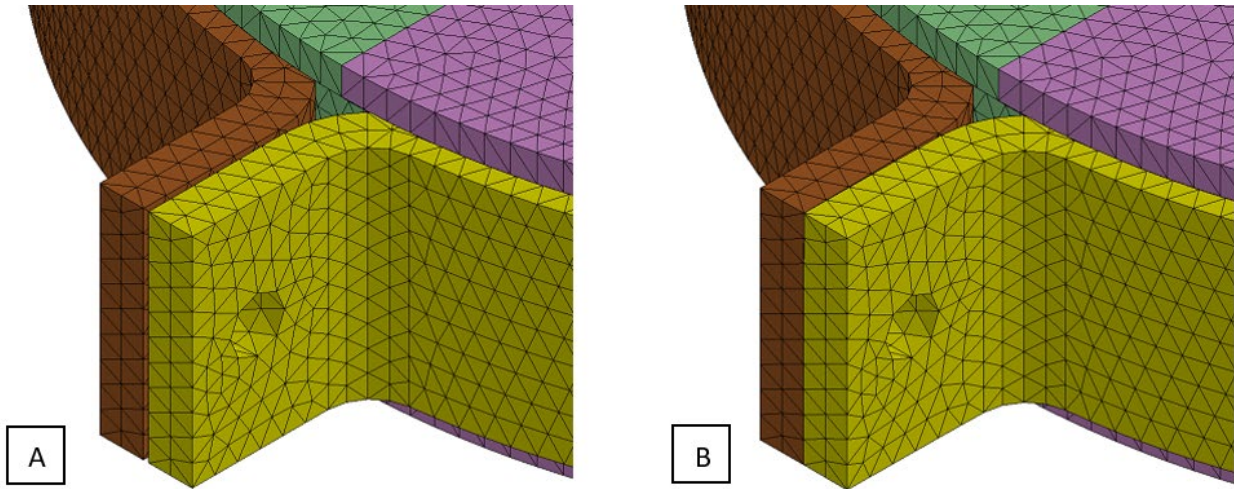


Figure 49 - Flange displacement for clamping simulation.

4.2.3 Boundary Conditions

During the clamping simulation, all elements in the inner boss were fully constrained. The inner boss was fixed directly to the clamping surface and has no motion. Figure 50 shows the second boundary condition applied to the numerical model. Each clamp block had node sets that were constrained to move in the bottom plane. This boundary condition allowed for the clamp to be tightened while remaining in the plane of the base plate.

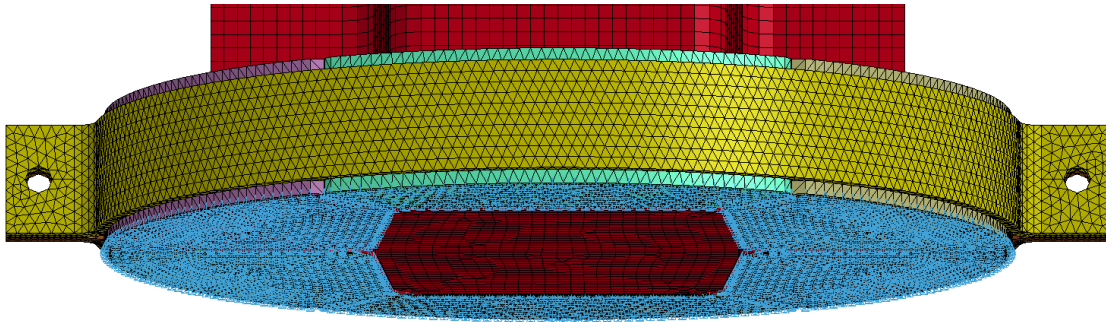


Figure 50 - Clamping simulation boundary conditions.

4.3 Numerical Model of the Axial Crush Test

All history variables, including stress state, position, and strain of the parts in the clamping simulation, were used as an input to the axial crush simulation. All boundary conditions were removed from the

clamping simulation and new boundary conditions were imposed. The remaining parts of the axial crush fixture were modelled using elastic elements and the pneumatic impactor was modeled using rigid solid elements. The pneumatic impactor was modeled as a rectangular prism having the same mass as the impactor used in the experimental crush tests. The fold initiator was positioned using a parametric study to determine where the greatest amount of localized damage occurred. The fold initiator was positioned 57.5 mm from the end of the channel section.

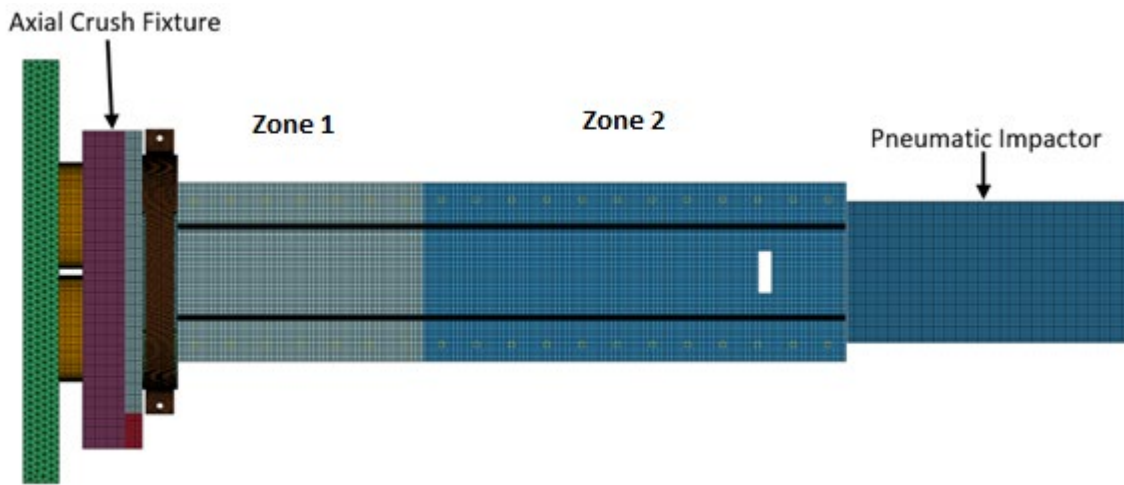


Figure 51 – Axial crush numerical model.

4.3.1 Load Cell Modeling

The four Dytran 1210V7 load cells were modeled using the critical dimensions provided by the manufacturer. The load cell connectors were omitted for simplicity. The material parameters used were consistent with steel except for the elastic modulus, which was set as 376 GPa to account for the piezoelectric material. The elastic modulus was calculated using the load cell stiffness and load cell geometry provided by the manufacturer.

4.3.2 Boundary conditions

The nodes at the end of the barrier plate that would be in contact with the impact barrier were constrained in all six degrees of freedom. The pneumatic impactor was constrained to translation in the z-axis (direction of crushing) since the pneumatic impactor cannot rotate in any direction due to the barrel having a square cross-section.

The clamping blocks, clamping rings, and inner boss used the default keyword, *DEFORMABLE_TO_RIGID, to maintain the clamping pressure on the channel section for the axial crush simulation. The rigid components and the remaining parts of the clamping fixture were constrained to each other using the tied surface-to-surface contact algorithm in LS-DYNA. A single surface contact algorithm was used to contact the channel section to itself.

4.3.3 Tailored Model

To model a tailored channel for both the 1500 MPa PHS and the 2000 MPa PHS, two material models were applied. Figure 51 shows the two material zones with the first zone starting from the clamped end of the channel and propagating 200 mm down the channel. The remaining shell elements made up the second zone. The material model for Zone 1 was modelled using the fully hardened flow curves from material quenched in a die at 20 °C. Elements in Zone 2 used a material model using flow curves from the material quenched at 550 °C.

Numerical simulations were also run using channels with a single, fully hardened material model to observe the effects of tailoring channels.

5. Mechanical Test Results

5.1 Hardness Tests

5.1.1 Tensile Specimen Hardness

The tailored sheets of 1500 MPa PHS and 2000 MPa PHS were hardness tested five times on each mini dogbones gauge section. The hardness of each steel grade and each as-quenched condition was determined as the average of five repeat hardness measurements. Each repeat test was done 2 mm apart in the y direction shown in Figure 53 to see the influence on the sheet's microstructure gradient. The average standard deviation of all the hardness tests was 10.3 HV, accounting for 2.3% of the average hardness. Therefore, the variation in the gauge hardness was considered negligible.

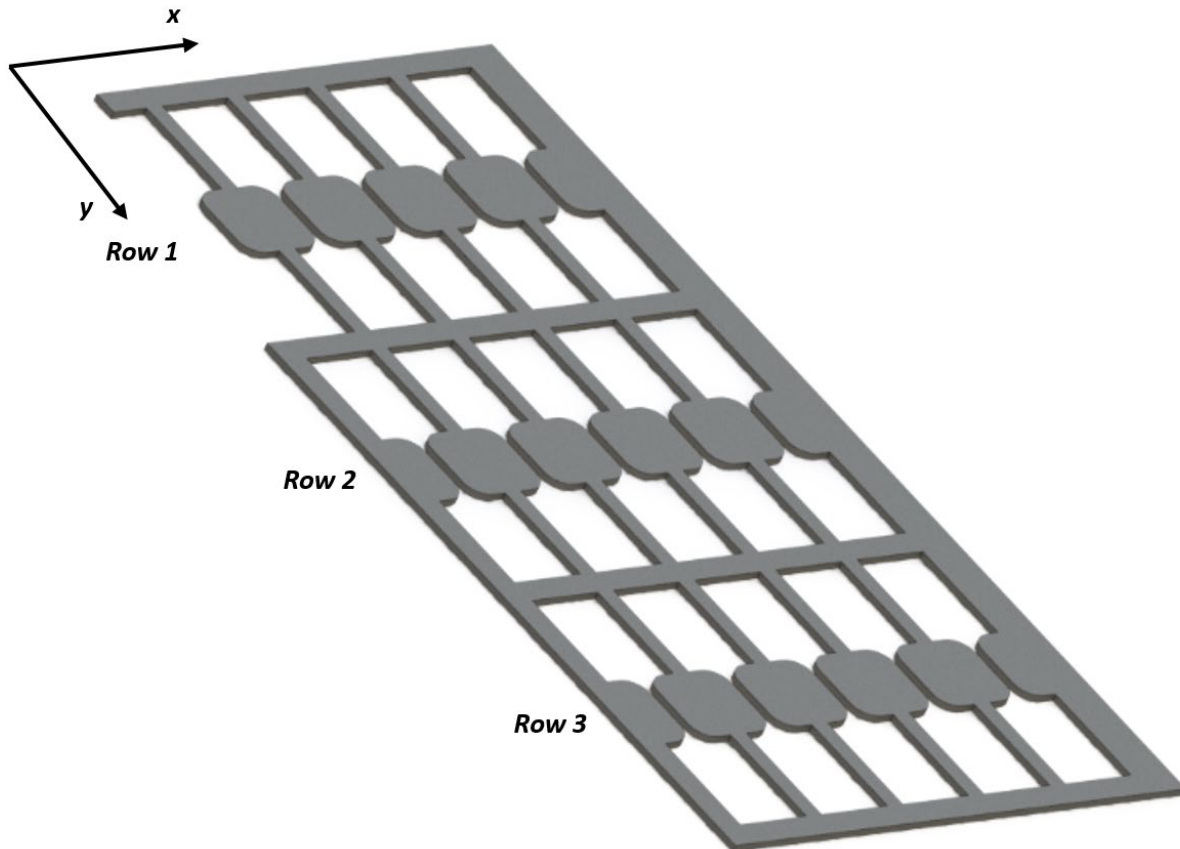


Figure 52 - Specimen layout cut from tailored sheets.

The tailored sheets were tested in the y-direction to ensure material homogeneity. The results of the hardness testing are shown in Tables 7 and 8.

| <i>Die Quenching Temperature</i> | <i>Row Number</i> | <i>Vickers Hardness (HV)</i> | <i>Average (HV)</i> | <i>Standard Deviation (HV)</i> |
|----------------------------------|-------------------|------------------------------|---------------------|--------------------------------|
| 20 °C | 1 | 469.5 | 472.6 | 2.22 |
| | 2 | 473.8 | | |
| | 3 | 474.6 | | |
| 250 °C | 1 | 442.3 | 444.1 | 6.95 |
| | 2 | 436.6 | | |
| | 3 | 453.3 | | |
| 350 °C | 1 | 381.8 | 405.9 | 17.49 |
| | 2 | 413.3 | | |
| | 3 | 422.7 | | |
| 550 °C | 1 | 218.1 | 224.9 | 7.56 |
| | 2 | 221.1 | | |
| | 3 | 235.4 | | |

Table 7 - Average specimen hardness for rows in tailored sheets of 1500 MPa PHS.

| <i>Die Quenching Temperature</i> | <i>Row Number</i> | <i>Vickers Hardness (HV)</i> | <i>Average (HV)</i> | <i>Standard Deviation (HV)</i> |
|----------------------------------|-------------------|------------------------------|---------------------|--------------------------------|
| 20 °C | 1 | 577.8 | 574.3 | 3.09 |

| | | | | |
|--------|----------|-------|-------|-------|
| | 2 | 570.3 | | |
| | 3 | 574.9 | | |
| | 1 | 533.4 | | |
| 250 °C | 2 | 548.4 | 526.2 | 21.67 |
| | 3 | 496.8 | | |
| | 1 | 500.7 | | |
| 350 °C | 2 | 470.6 | 477.9 | 16.46 |
| | 3 | 462.3 | | |
| | 1 | 301.4 | | |
| 550 °C | 2 | 332.2 | 297.1 | 10.83 |
| | 3 | 311.4 | | |

Table 8 - Average specimen hardness for rows in tailored sheets of 2000 MPa PHS.

The final set of hardness tests determined if the hardness was consistent in the y-direction of the sheets shown in Figure 52. Two different cooling conditions for the 1500 MPa PHS and 2000 MPa PHS were tested, and the results are shown in Table 9 and Table 10. The hardness testing results showed that the sheets have a negligible change in hardness in the sheet's x-direction and throughout the gauge length of each sample.

| Quenching Condition | Specimen Hardness (HV) | | | | | Average (HV) | Standard Deviation (HV) |
|----------------------------|-------------------------------|----------|----------|----------|----------|---------------------|--------------------------------|
| | 1 | 2 | 3 | 4 | 5 | | |
| 250 °C | 445.9 | 451.5 | 447.2 | 449.5 | 446.8 | 448.2 | 2.04 |
| 550 °C | 218.1 | 216.8 | 213.6 | 216.3 | 214.2 | 215.8 | 1.65 |

Table 9 - Average specimen hardness across rows in tailored sheets of 1500 MPa PHS.

| Quenching Condition | Specimen Hardness (HV) | Average (HV) |
|----------------------------|-------------------------------|---------------------|
|----------------------------|-------------------------------|---------------------|

| | 1 | 2 | 3 | 4 | 5 | | <i>Standard Deviation (HV)</i> |
|--------|-------|-------|-------|-------|-------|-------|------------------------------------|
| 250 °C | 541.8 | 547.7 | 545.1 | 544.9 | 543.2 | 544.5 | 1.97 |
| 550 °C | 301.4 | 295.5 | 294.9 | 294.5 | 298.8 | 297.1 | 2.65 |

Table 10 - Average specimen hardness across rows in tailored sheets of 2000 MPa PHS.

5.1.2 Split Hopkinson Bar Specimen Hardness

The gripping ends of the split Hopkinson bar specimens were softened according to the procedure described in Section 3.4.3 shown in Figure 35 to avoid slipping in the grips during the tests. The hardness was measured along the length of two fully hardened (quenched with dies at 20 °C) 2000 MPa PHS tensile specimens, one of which had its gripping ends softened. Figure 53 shows the hardness measurements along the length of both specimens and demonstrates that the softening procedure was successful in reducing the hardness in the gripping ends without affecting the hardness in the gauge area.

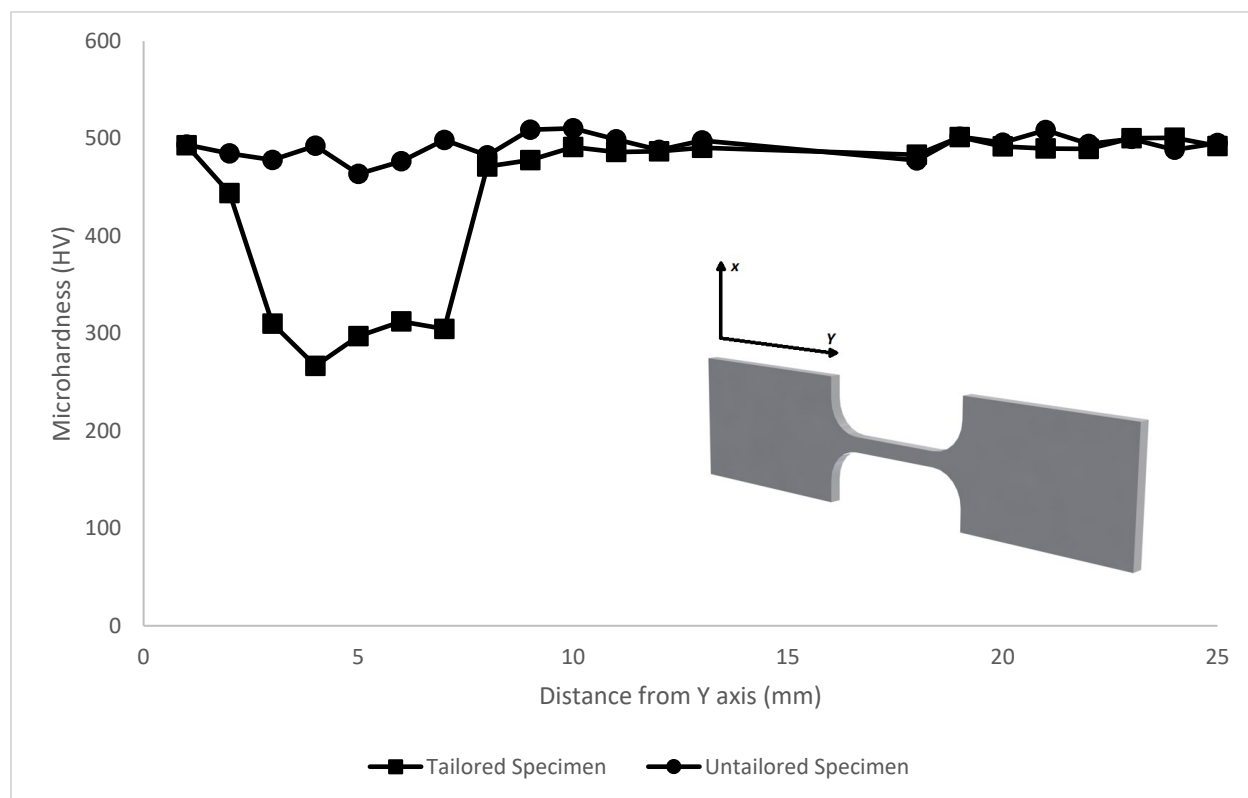


Figure 53 - Microhardness distribution of tailored and untailored specimens.

The hardness dropped to 266 HV at 4 mm from the end of the gripping region and then returned to the original hardness value of the specimen prior to the softening of the gripping ends. The untailored specimen had an average hardness of 492.2 HV across the entire specimen. After 10 mm, the tailored specimen had an average hardness of 492.0 HV. The difference in the hardness values after the tailored zone and in the untailored specimen shows that the softening of the grips did not affect the microstructure and mechanical properties of the gauge region. The control tensile sample had a uniform hardness along its entire length.

The tailoring technique helped reduce the hardness in the gripping region and was shown that it does not affect the specimen's hardness.

5.2 Quasi-Static Tensile Testing

Commercial 2D-DIC post-processing software was used to synchronize the strain to the video time. Figure 54 shows the DIC software calculating the strain of a mini dogbone specimen tested at 0.003 s^{-1} .

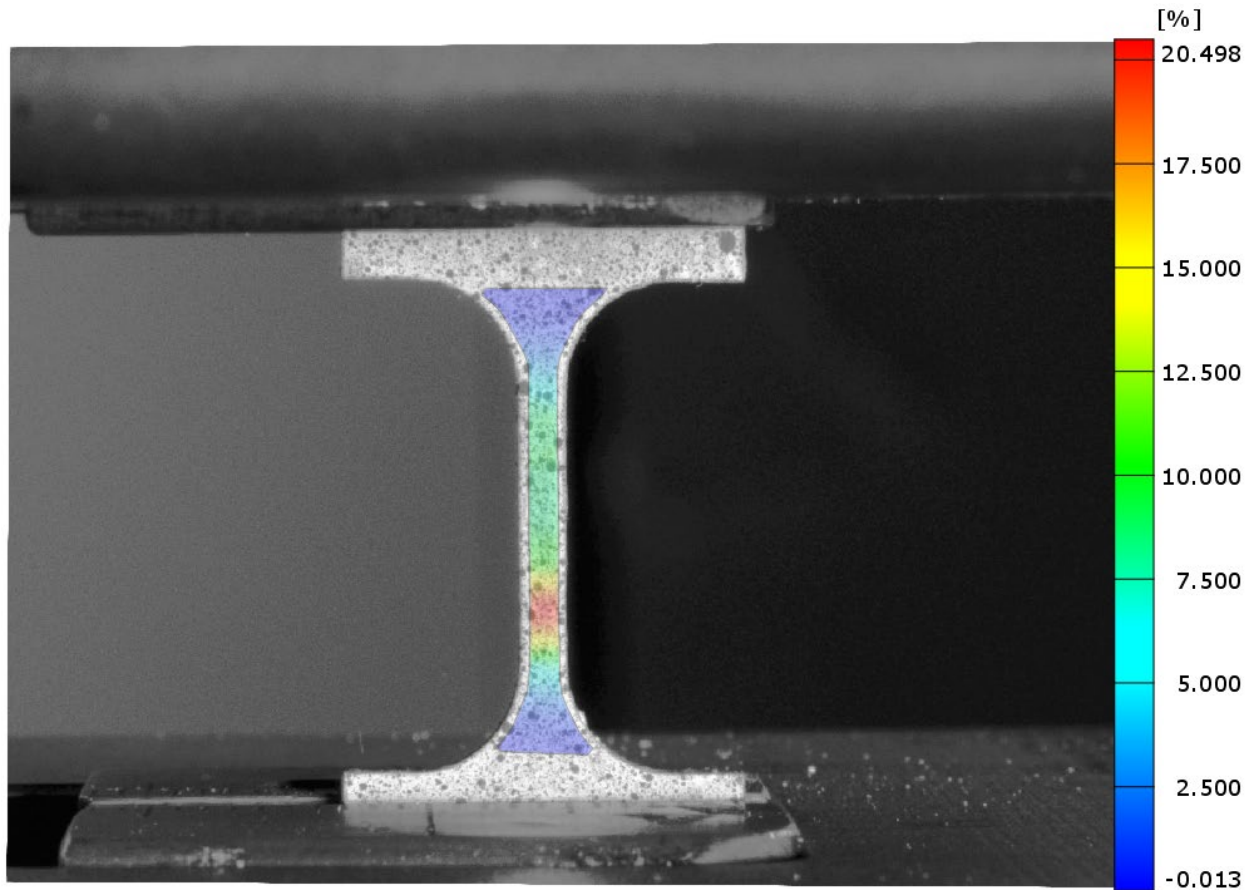


Figure 54 - DIC strain processing for 1500 MPa PHS.

Three repeat tests were performed for the 0.003 s^{-1} and 0.1 s^{-1} strain rate tensile tests. The results of the 1500 MPa PHS and the 2000 MPa PHS are shown in Figure 55 and Figure 56, respectively.

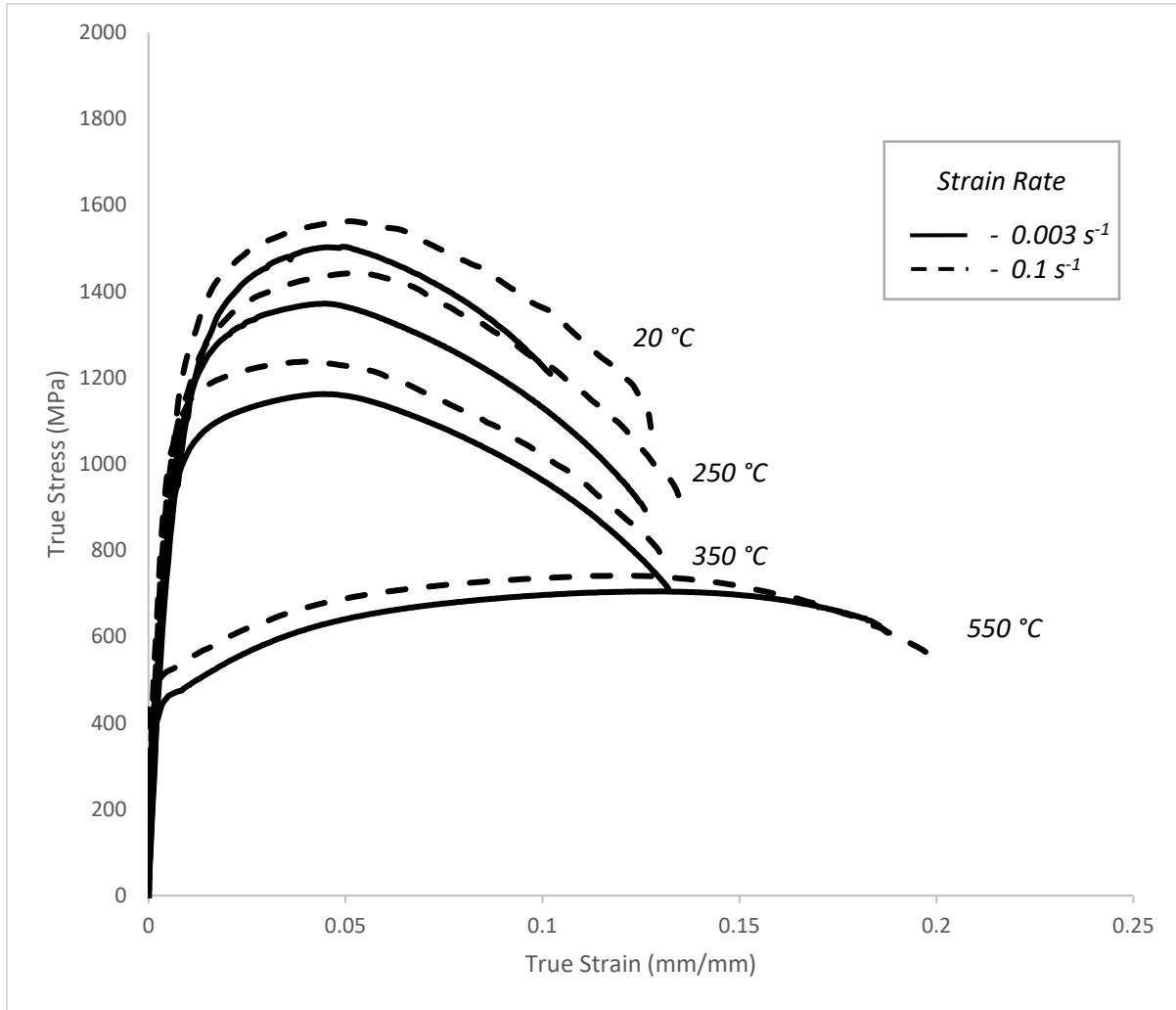


Figure 55 - True stress versus true strain for 1500 MPa PHS at strain rates of 0.003 s^{-1} and 0.1 s^{-1} .

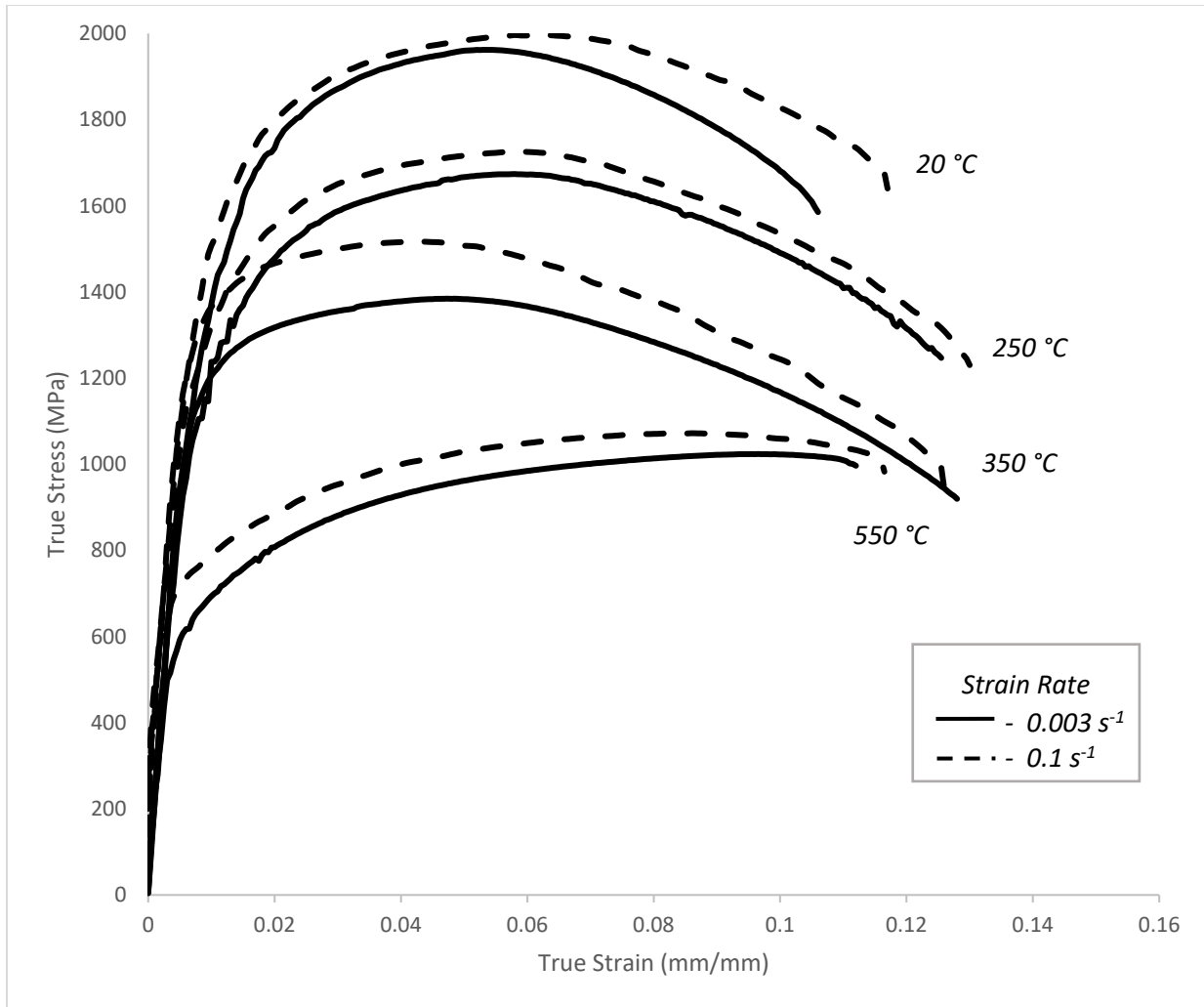


Figure 56 - True stress versus true strain for 2000 MPa PHS at strain rates of 0.003 s^{-1} and 0.1 s^{-1} .

5.3 Intermediate Rate Tensile Testing

The intermediate strain rate tensile testing was completed using three repeat tests for each quenching condition. The strain of each test was post-processed using ProAnalyst Motion Analysis Software. Figure 57 shows the tracking of the strain using a two-dimensional analysis. The undeformed specimen was marked using a white paint marker to create dots that the high-speed camera can track.

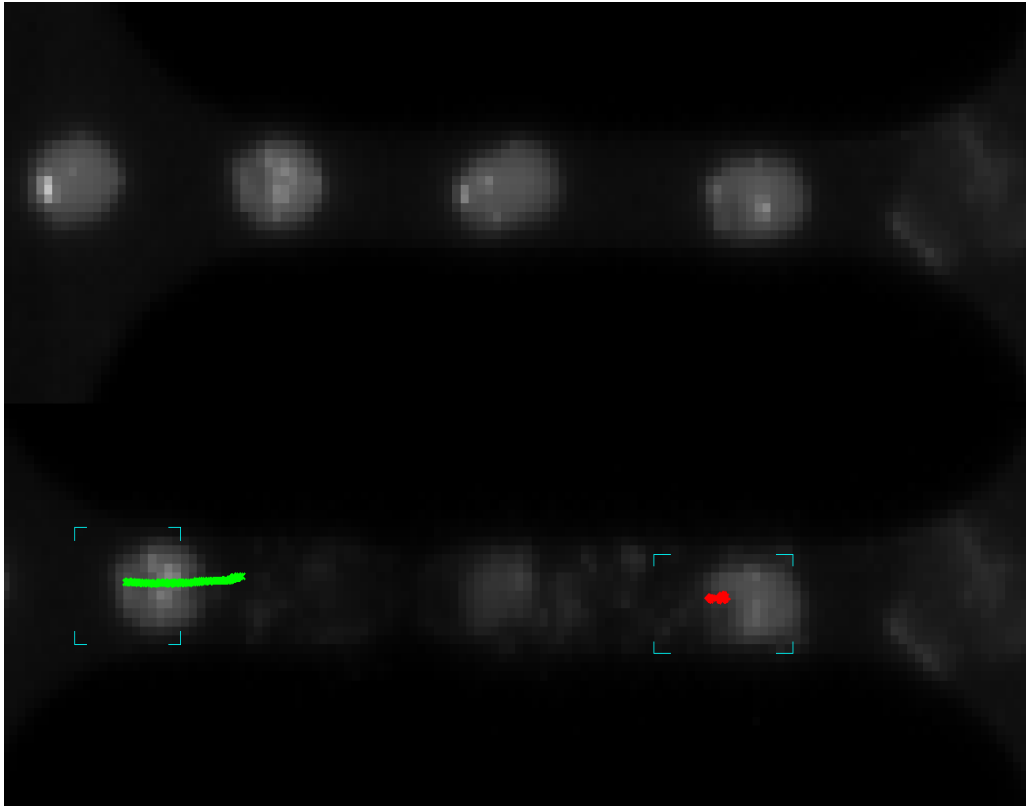


Figure 57 -Strain calculation using motion tracking software.

The load cell data was filtered using a 2kHz filter to remove oscillations created by inertial effects in the system. Each test was validated against unfiltered data using a zero experimental measurement error validation metric [75]. The validation metric used the absolute relative error between the experimental values ($Y(x_i)$) and the filtered values ($y(x_i)$)

$$V = 1 - \frac{1}{I} \sum_{i=1}^{i=1} \tanh \left| \frac{y(x_i) - Y(x_i)}{Y(x_i)} \right| \quad (18)$$

A validation metric of 1.0 indicates a perfect fit between the filtered and unfiltered results, and a validation metric of 0 indicates the filtered results do not correlate with the unfiltered results. A comparison between a test with inertial effects present and the same test using a 2 kHz filter is shown in Figure 58. The validation metric results are shown in Table 11.

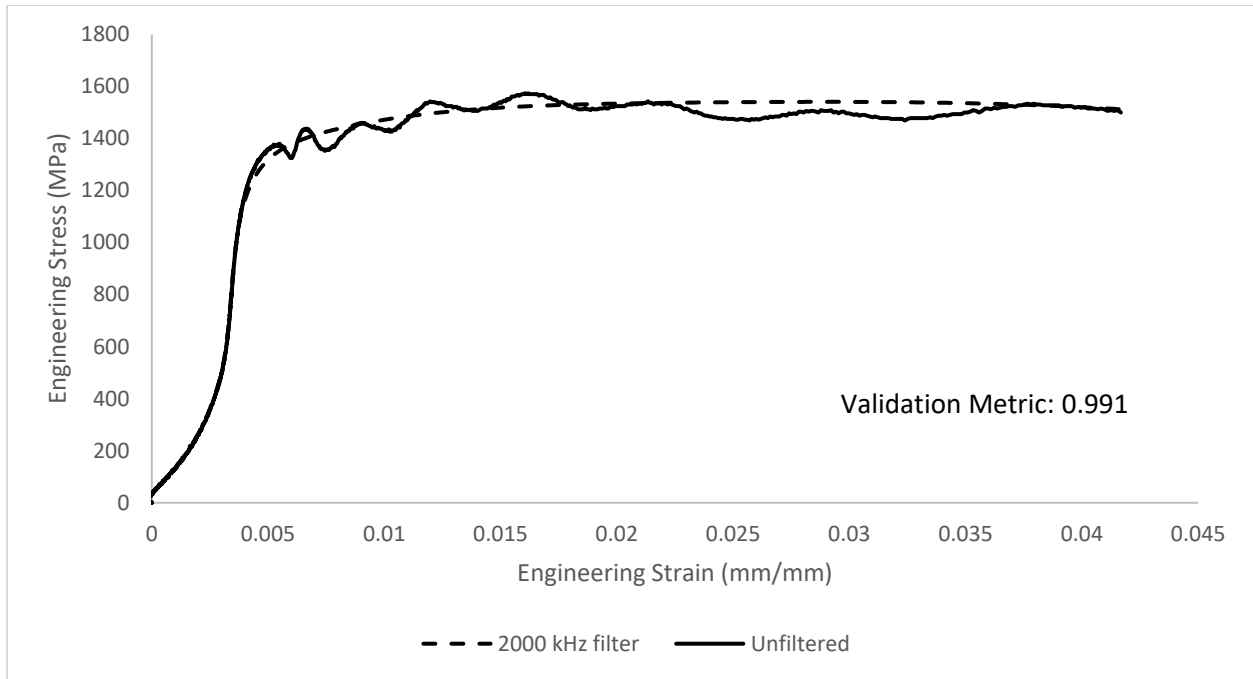


Figure 58 - 1500 MPa PHS quenched at 350 °C comparison of filtering at 2000 kHz at a strain rate of 100 s⁻¹.

| 1500 MPa PHS | | 2000 MPa PHS | |
|--------------------------------|--------------------------|--------------------------------|--------------------------|
| Quench Temperature (°C) | Validation Metric | Quench Temperature (°C) | Validation Metric |
| 20 | 0.9884 | 20 | 0.9808 |
| 250 | 0.9563 | 250 | 0.9925 |
| 350 | 0.9876 | 350 | 0.9911 |
| 550 | 0.9708 | 550 | 0.983 |

Table 11 - 100 s⁻¹ strain rate validation metric results.

The lowest validation metric was 0.9563 for 1500 MPa PHS quenched at 250 °C, and the average value was 0.9813. The results indicate that the filtered results strongly correlate with the unfiltered results. The filtered results were averaged in the same manner as the quasi-static experiments and are shown in Figures 59 and 60. The quenching temperatures are displayed for each material on the figures.

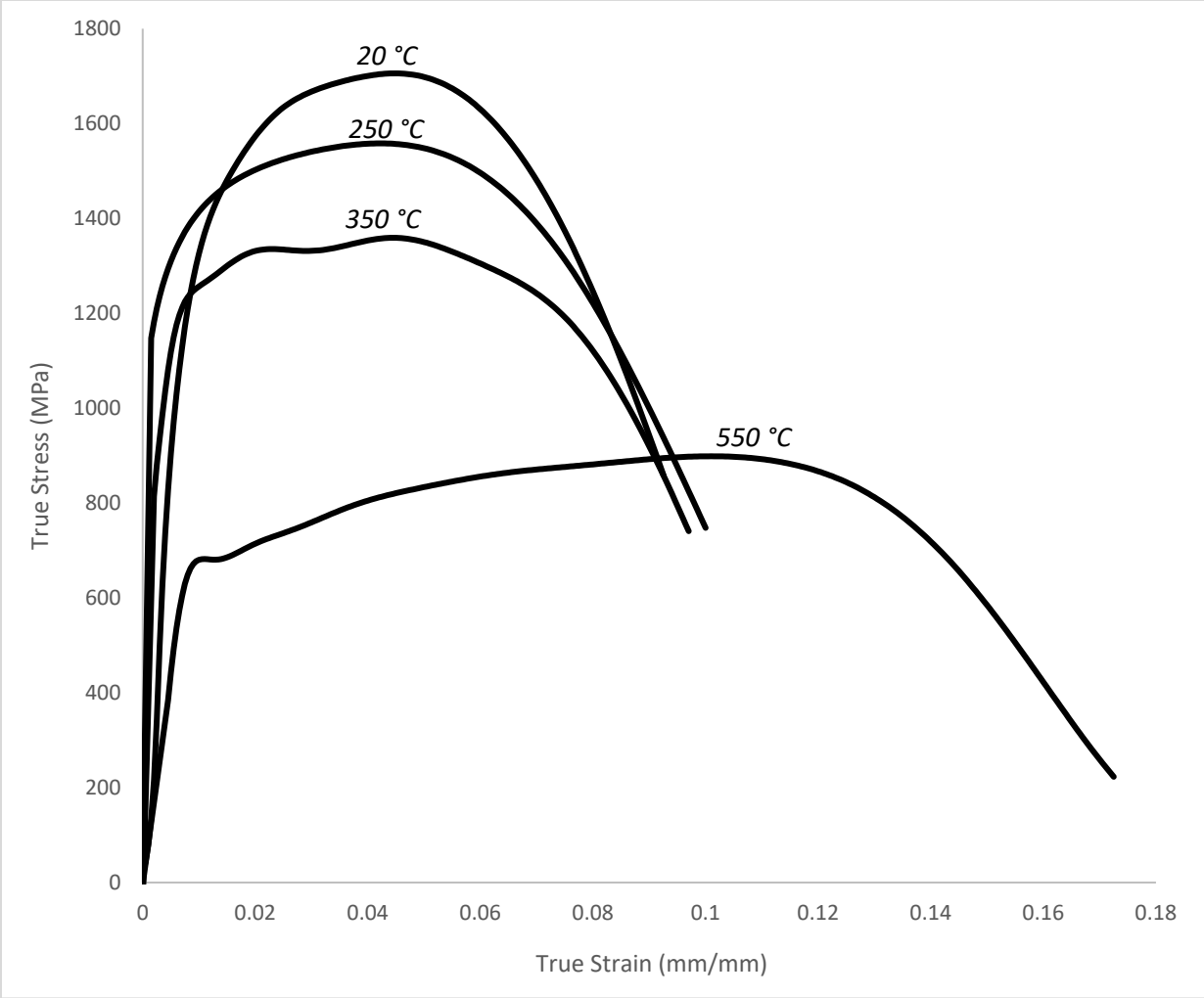


Figure 59 - Average intermediate strain rate tensile testing for 1500 MPa PHS at a strain rate of 100 s⁻¹.

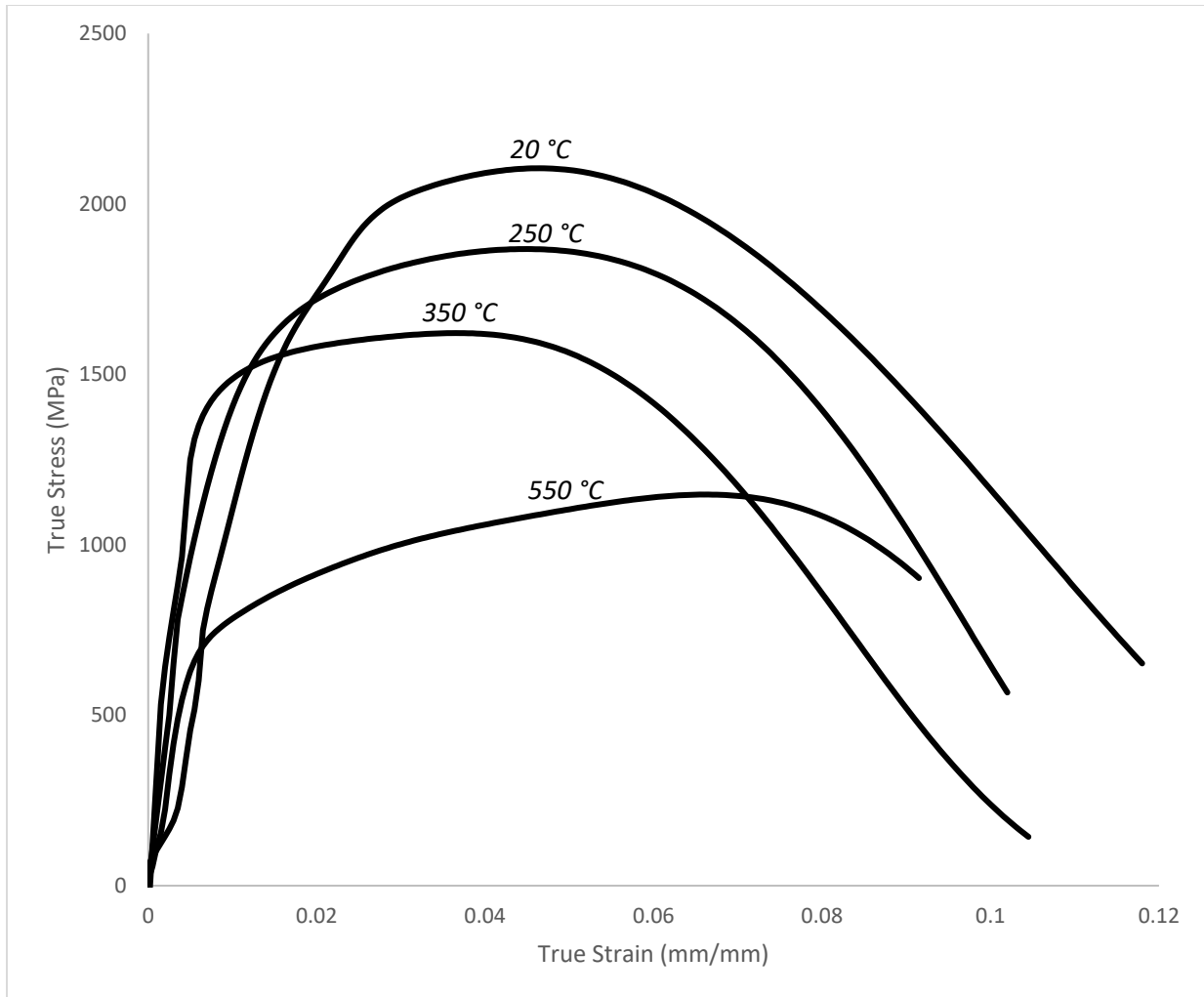


Figure 60 - Average intermediate strain rate tensile testing for 2000 MPa PHS at a strain rate of 100 s^{-1} .

5.4 High-Rate Tensile Testing

The split Hopkinson bar testing was done using three repeat tests for each test condition. Testing the high-strength materials in this study created challenges involving breaking the specimen at the first stress wave through the specimen. If the specimen broke on any subsequent wave, the test yielded a lower-than-expected value for the material's ultimate stress. Therefore, the tanks pressure of the split Hopkinson bar was increased from 414 kPa to 551kPa to ensure the ultimate stress was accurate. Using equation 19, the striker velocity of 21.2 m/s was estimated—the higher air pressure resulted in an average strain rate of 1500 s^{-1} . In equations 19 x represents striker velocity (m/s) and y represents tank pressure (kPa).

$$y = 0.0165x^3 + 0.2433x^2 + 11.342x + 5.0761 \quad (19)$$

The high rate (1500 s^{-1}) tensile tests were processed using a 250 kHz filter to reduce the high frequencies in the data. The tensile testing results for each quenching condition are shown below in Figures 61 and 62.

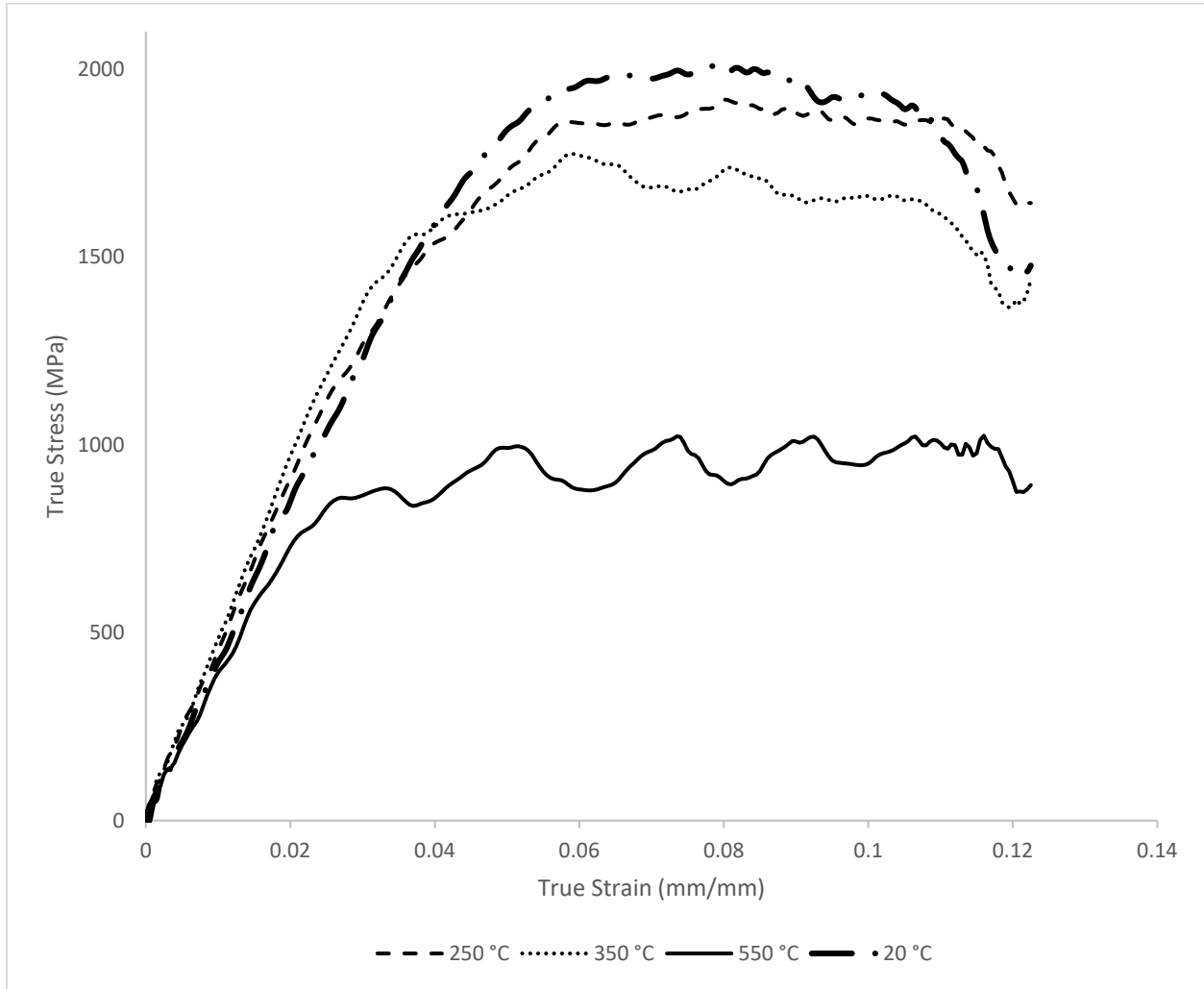


Figure 61 - Average high strain rate tensile testing for 1500 MPa PHS at a strain rate of 1500 s^{-1} .

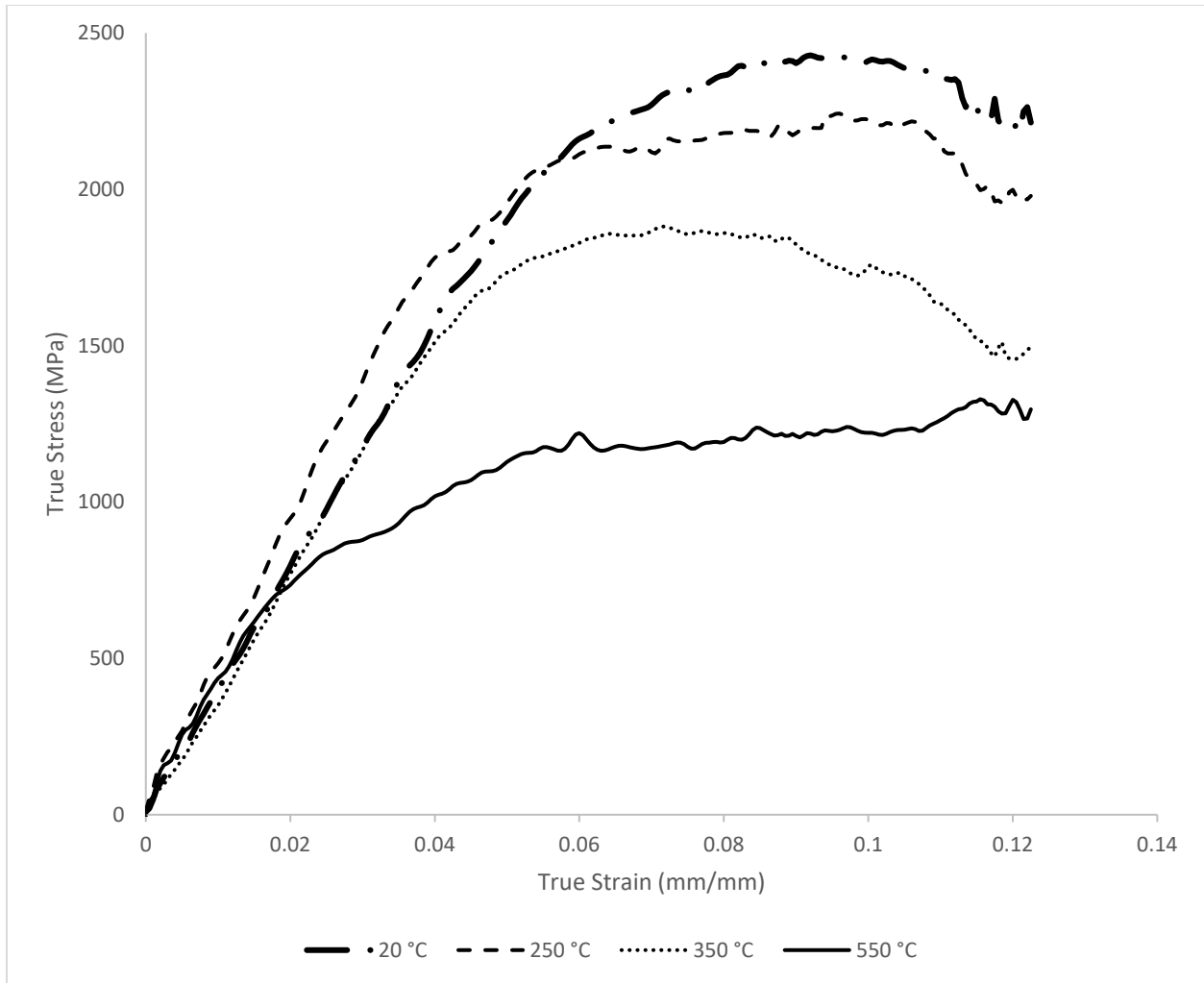


Figure 62 - Average high strain rate tensile testing for 2000 MPa PHS at a strain rate of 1500 s^{-1} .

There appears to be a stress wave recorded in the testing that is most prevalent in the 1500 MPa PHS that was quenched at 550 °C. The stress wave was still present in the other tests, but the effects were less noticeable. The elastic region of split bar testing is often neglected as the elastic modulus is underestimated. The cause of low elastic modulus was discussed by Harrigan et al. [76] and Miao et al. [77]. Factors that influence the lower elastic modulus include ramp-up time for the system as well as the specimen reaching dynamic equilibrium. The stress in the split Hopkinson bar specimen reached equilibrium after the test was initiated and the specimen deformed elastically. For this work, only the plastic region was considered as it is required as an input to the numerical models.

5.5 True Strain Rate

The true strain rate versus true strain for an individual test at each chosen strain rate is shown in Figure 63. The strain rate curves are for the 0.003 s^{-1} , 1.0 s^{-1} , 100 s^{-1} , and 1500 s^{-1} tests.

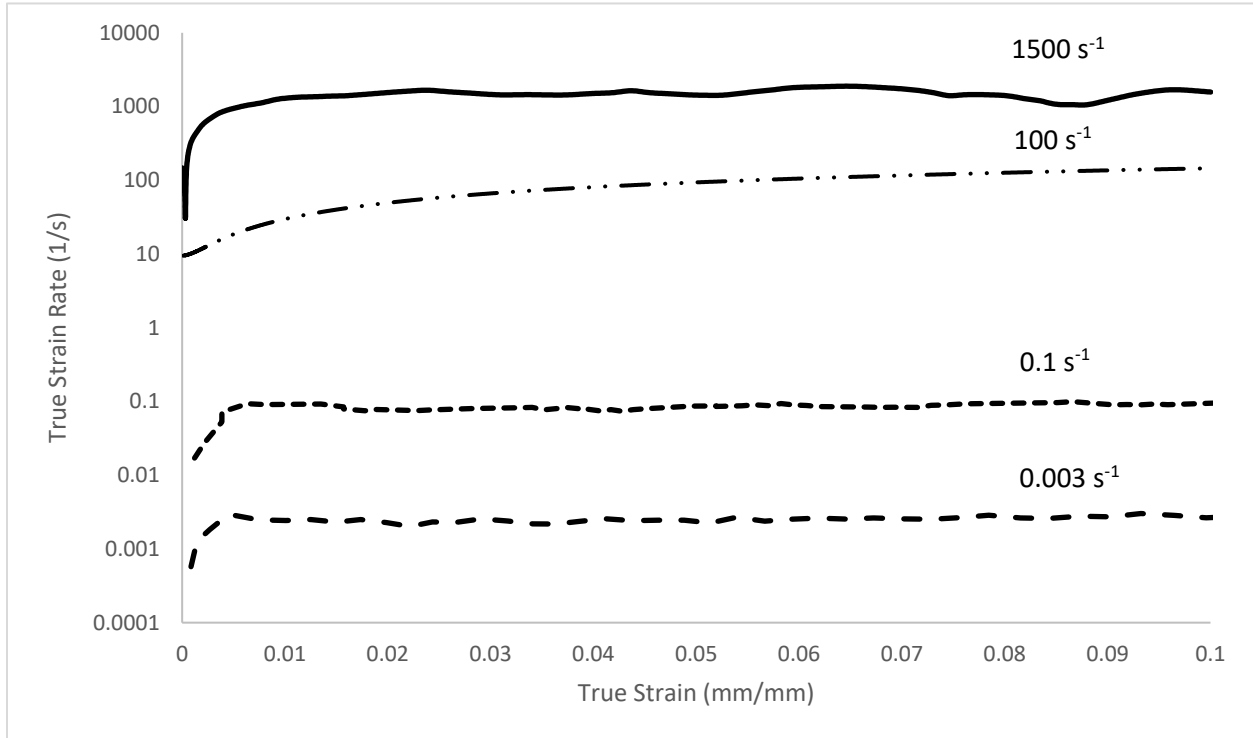


Figure 63 - True strain rate versus true strain curves.

The true strain rate was calculated in the plastic strain region, and the average rate in each test is taken. The tests were averaged to give quasi-static strain rates of 0.028 s^{-1} and 0.912 s^{-1} . The average intermediate true strain rate is 96.98 s^{-1} , and the average high true strain rate is 1496 s^{-1} .

5.6 Hardening Function Fitting

All repeat tests for each set of tensile tests were down sampled using a cubic spline interpolation between each data point to set every test to the same strain domain. The repeat tests were then averaged to create an engineering stress versus engineering strain curve shown in Figure 64. Results are discretized using 200 points of data for each test. Finally, the curves were converted to true stress versus true strain using equations which was applicable over the effective plastic strain domain:

$$\sigma_{\text{true}} = \sigma_{\text{engineering}} * (1 + \epsilon_{\text{engineering}}) \quad (20)$$

$$\epsilon_{\text{true}} = \ln(1 + \epsilon_{\text{engineering}}) \quad (21)$$

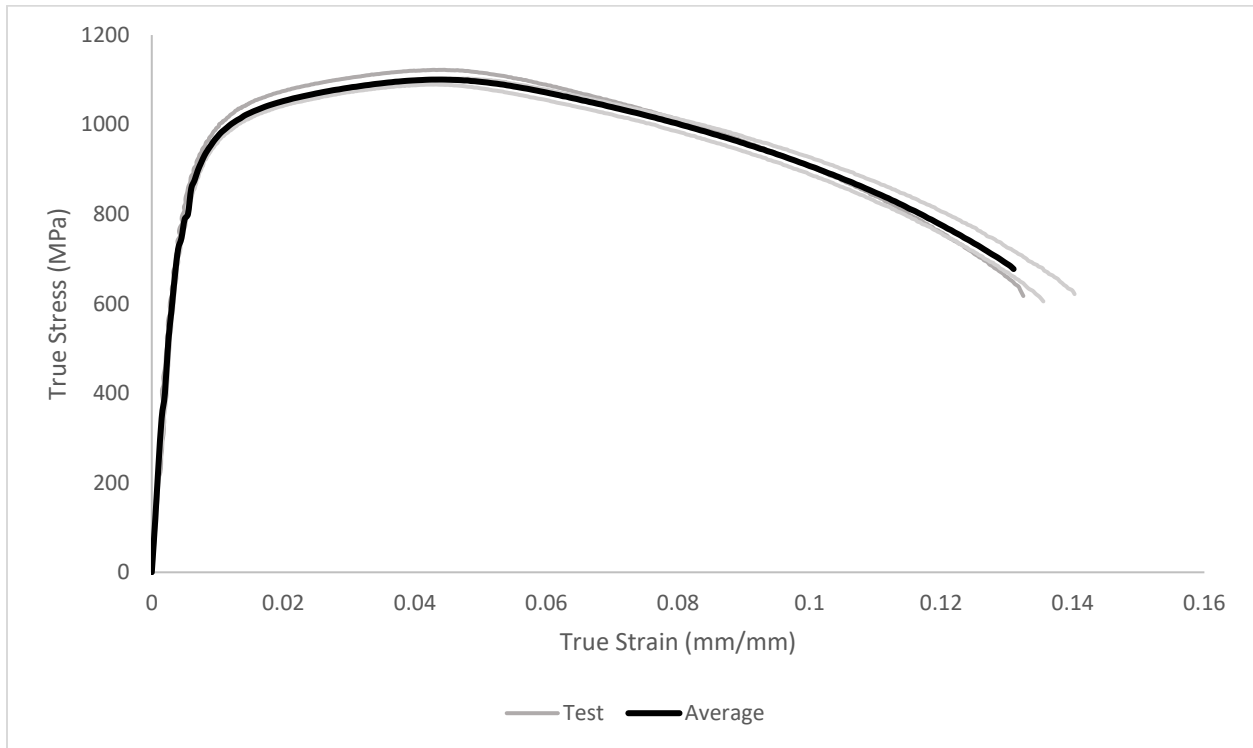


Figure 64 - Average true stress versus true strain curves for 1500 MPa PHS quenched at 350 °C at strain rates of 0.003 s⁻¹.

After removing the elastic portion and the post-ultimate stress regions, actual experimental stress versus effective plastic strain curves were produced. The 1500 and 2000 MPa PHS data are shown in Figures 66 and 67. The 250 °C quenching condition was omitted from the figures for clarity as they overlap the 350 °C and 20 °C curves. The solid curves in Figures 65 and 66 shows some oscillations due to ringing of the SHPB apparatus at high rates.

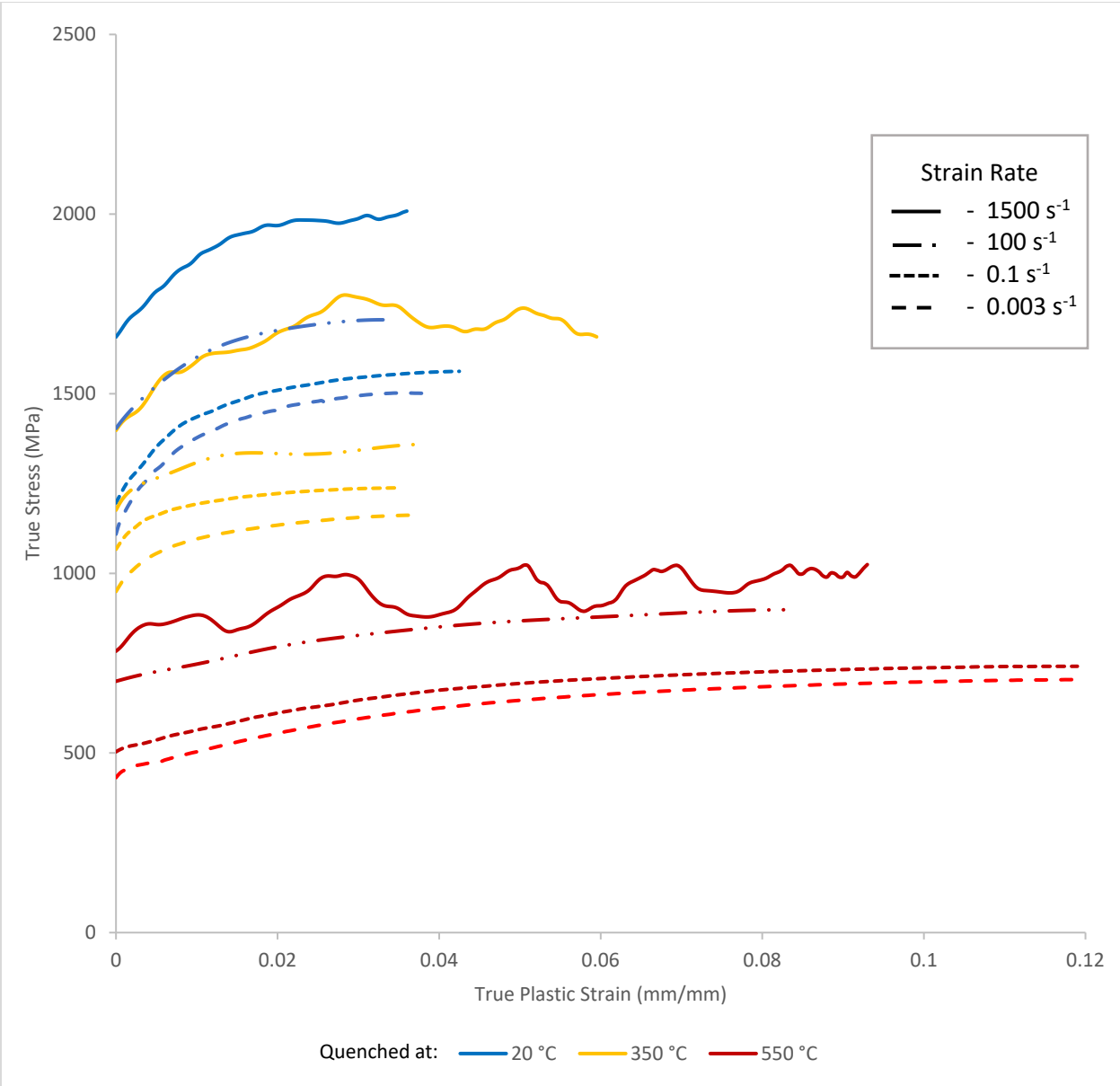


Figure 65 - Experimental flow curves for 1500 MPa PHS at all strain rates and material hardness values (250 °C curves are omitted for clarity).

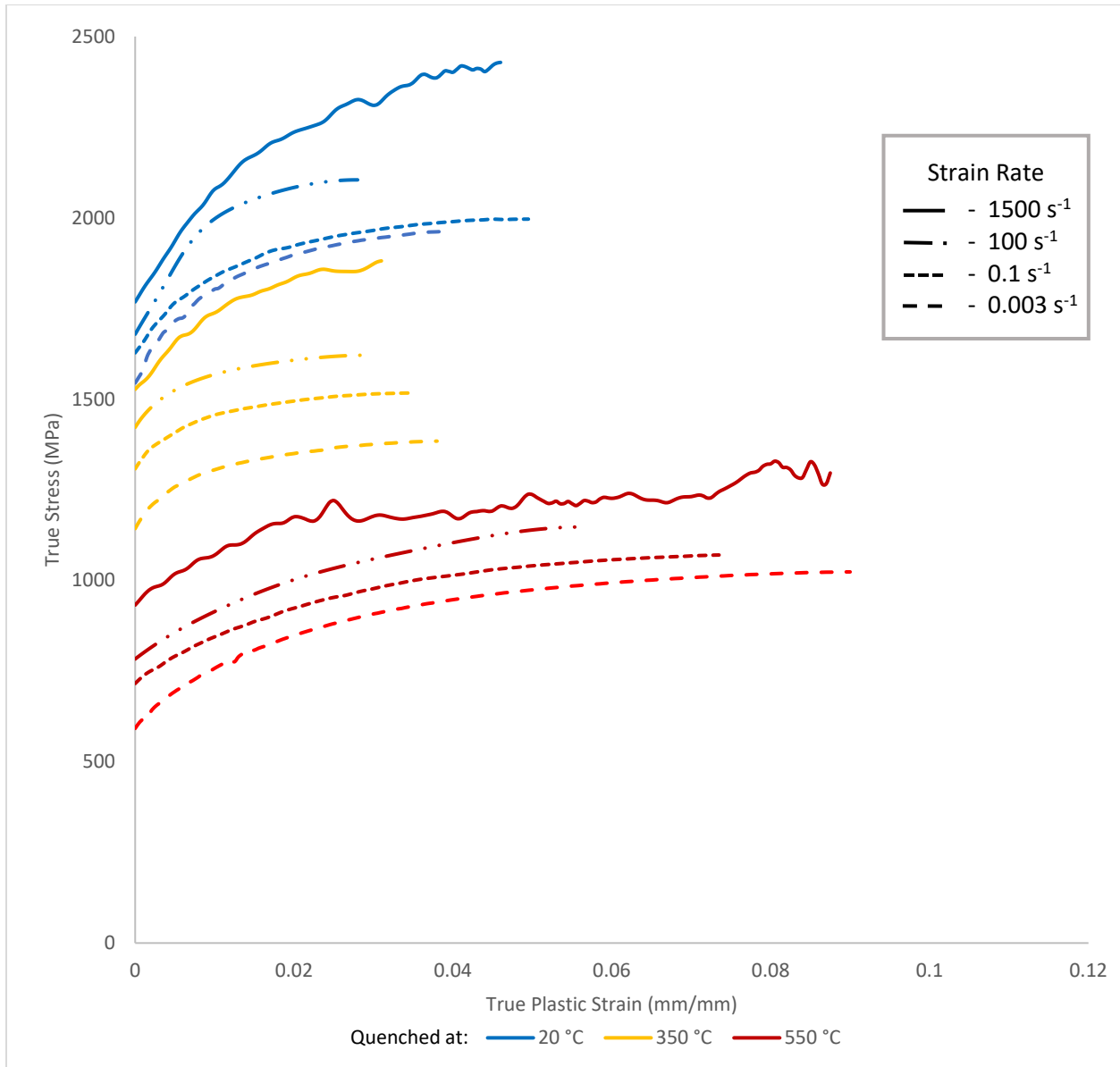


Figure 66 - Experimental flow curves for 2000 MPa PHS at all strain rates and material hardness values (250 °C curves are omitted for clarity).

A Voce hardening function was fitted to the experimental data using linear regression. The R squared values for each fitted function are shown in Table 12 and Table 13. Strain-rate sensitive functions were not necessarily due to the chosen numerical model. LS-DYNA’s material model MAT_24_LINEAR_PLASTICITY uses tabular data for each chosen strain rate to apply a simpler hardening function. The Voce hardening function strongly agreed with the experimental data at all strain rates. The fitted hardening functions are shown in Figures 67 to 74.

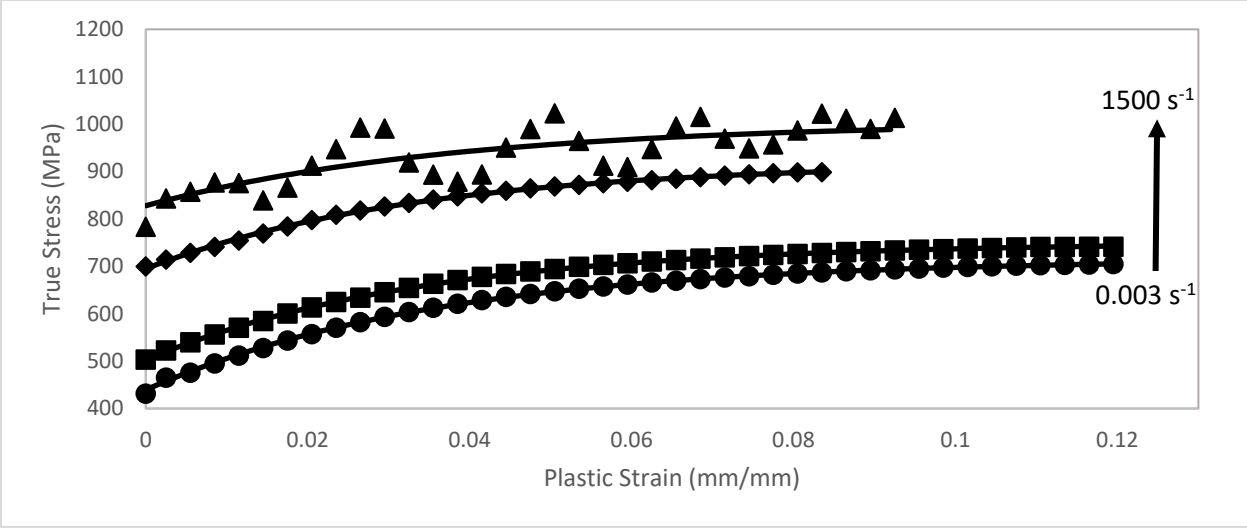


Figure 67 - Voce flow curves quenched at 550 °C for 1500 MPa PHS.

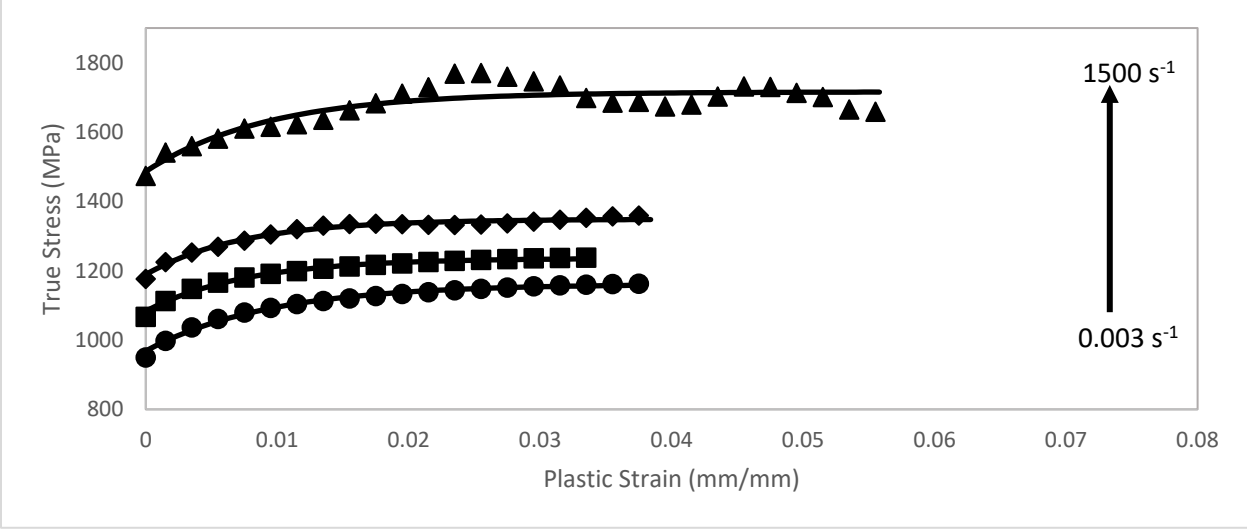


Figure 68 - Voce flow curves quenched at 350 °C for 1500 MPa PHS.

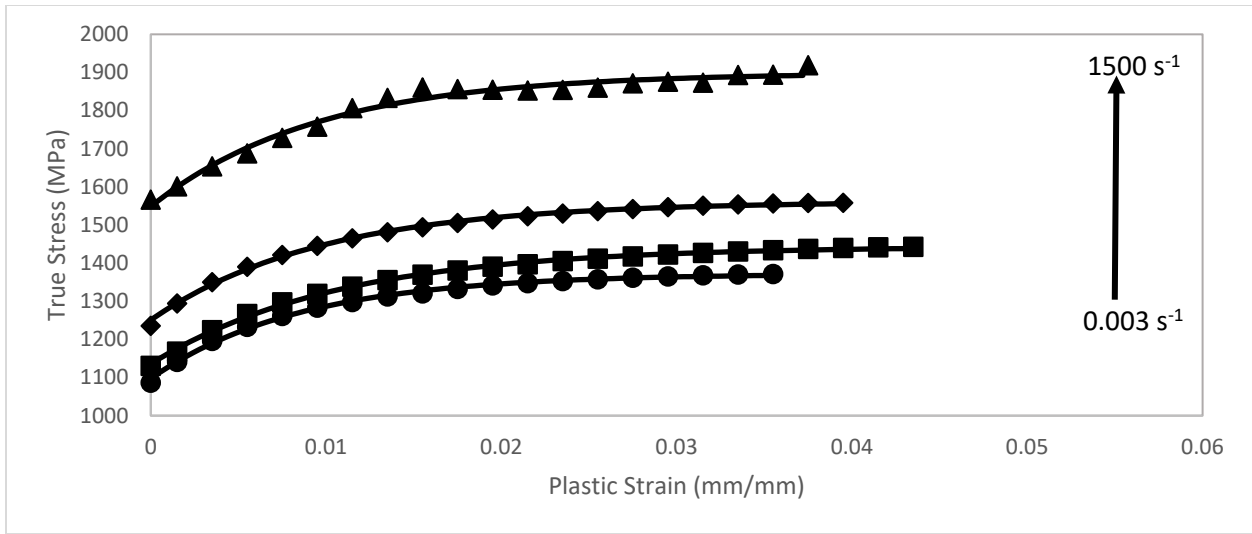


Figure 69 - Voce flow curves quenched at 250 °C for 1500 MPa PHS.

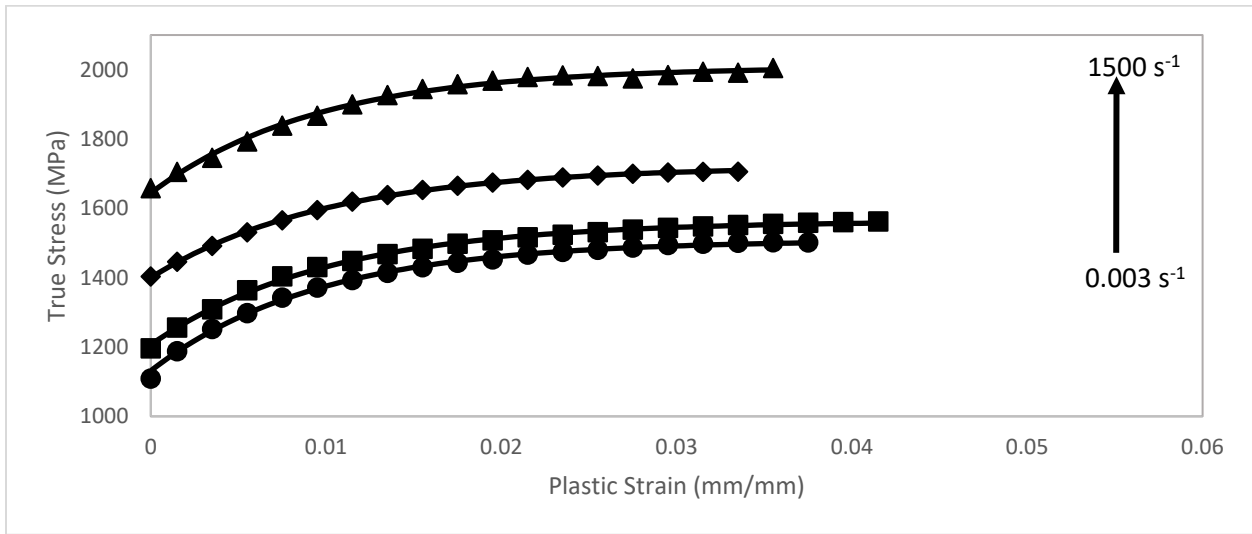


Figure 70 - Voce flow curves quenched at 20 °C for 1500 MPa PHS.

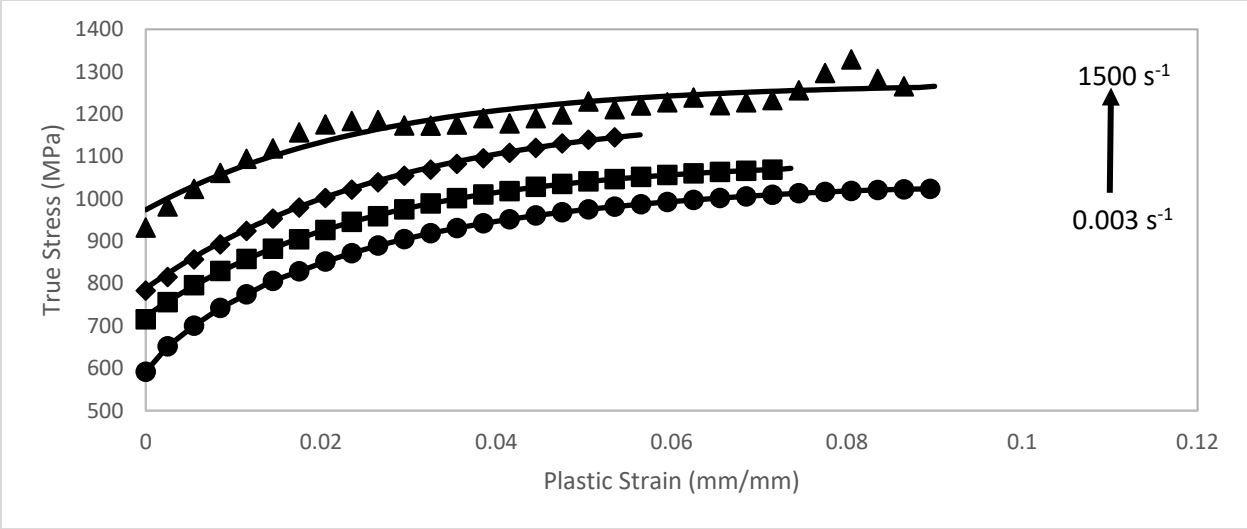


Figure 71 - Voce flow curves quenched at 550 °C for 2000 MPa PHS.

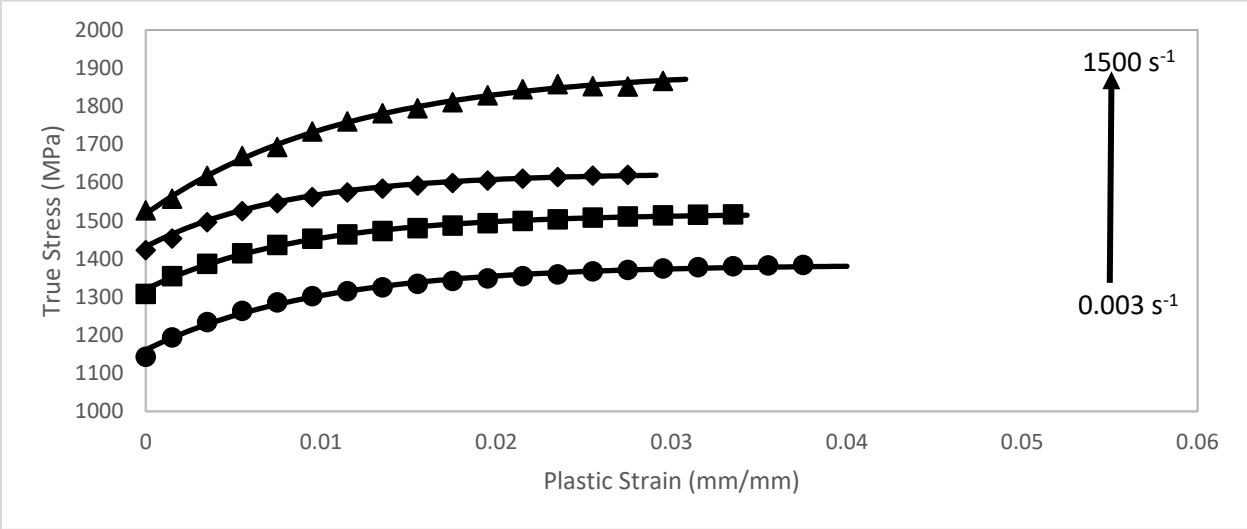


Figure 72 - Voce flow curves quenched at 350 °C for 2000 MPa PHS.

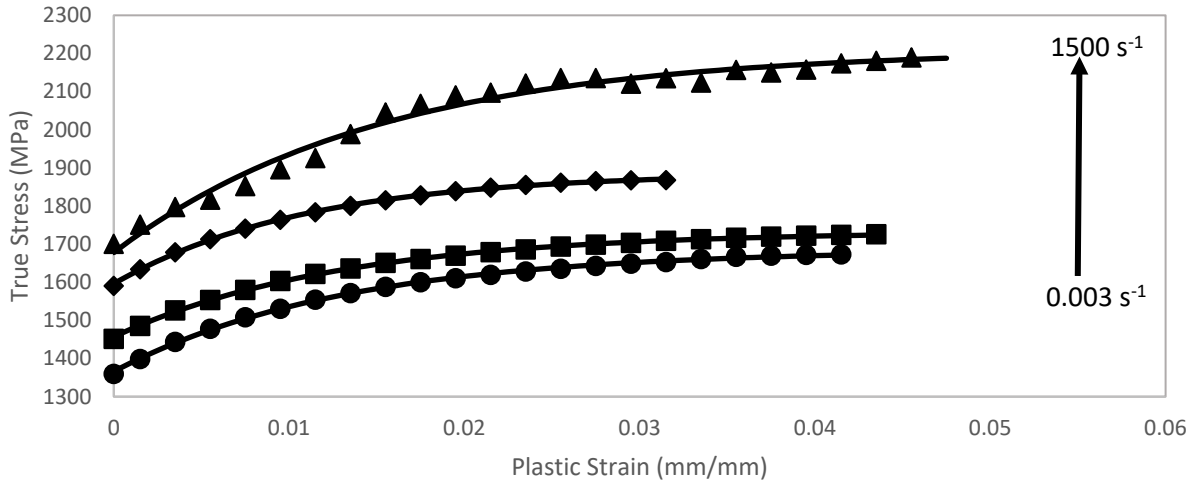


Figure 73 - Voce flow curves quenched at 250 °C for 2000 MPa PHS.

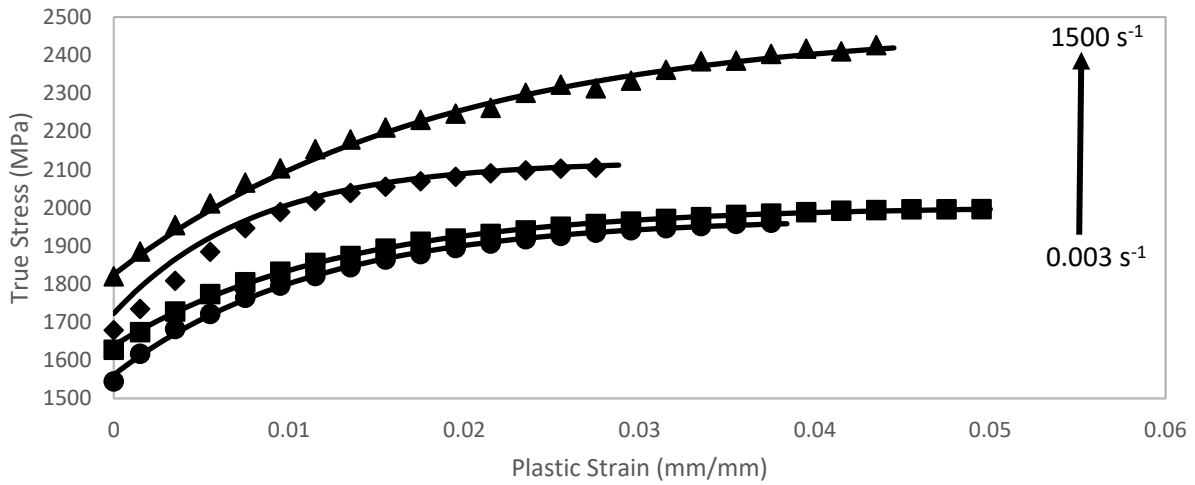


Figure 74 - Voce flow curves quenched at 20 °C for 2000 MPa PHS.

The 1500 MPa PHS shows a near constant rate of hardening for all quenching conditions and strain rates. The 2000 MPa PHS shows an increased rate of hardening for the 1500 s⁻¹ strain rate testing compared to the other strain rates in the specimens quenched at 350 °C, 250 °C and 20 °C. The increased rate of hardening suggests that 2000 MPa PHS does not have a uniform rate of hardening for the more martensitic microstructures.

| Quenching Temperature (°C) | Strain rate (s⁻¹) | R² |
|-----------------------------------|-------------------------------------|----------------------|
| 550 | 0.003 | 0.999 |
| | 0.1 | 0.999 |
| | 100 | 0.994 |
| | 1500 | 0.596 |
| 350 | 0.003 | 0.992 |
| | 0.1 | 0.991 |
| | 100 | 0.705 |
| | 1500 | 0.871 |
| 250 | 0.003 | 0.997 |
| | 0.1 | 0.998 |
| | 100 | 0.991 |
| | 1500 | 0.978 |
| 20 | 0.003 | 0.998 |
| | 0.1 | 0.998 |
| | 100 | 0.996 |
| | 1500 | 0.994 |

Table 12 - R squared values for fitted Voce hardening functions of 1500 MPa PHS.

| Quenching Temperature (°C) | Strain rate (s⁻¹) | R² |
|-----------------------------------|-------------------------------------|----------------------|
| 550 | 0.003 | 0.998 |
| | 0.1 | 0.999 |
| | 100 | 0.960 |
| | 1500 | 0.891 |
| 350 | 0.003 | 0.994 |
| | 0.1 | 0.997 |
| | 100 | 0.990 |
| | 1500 | 0.997 |
| 250 | 0.003 | 0.999 |
| | 0.1 | 0.999 |
| | 100 | 0.995 |
| | 1500 | 0.982 |
| 20 | 0.003 | 0.998 |
| | 0.1 | 0.999 |
| | 100 | 0.990 |
| | 1500 | 0.997 |

Table 13 - R squared values for fitted Voce hardening functions of 1500 MPa PHS.

The ultimate true stress versus the strain rate of the associated tests is plotted in Figures 75 and 76. The slope of the logarithmic plots of ultimate true stress versus the strain rate showed that the 1500 MPa PHS and the 2000 MPa PHS had an average slope of 18.9 MPa/s and 17.0 MPa/s respectively, in the quasi-static to intermediate rate domain. In the quasi-static to intermediate rate domain, there exists a sensitivity to strain rate in both materials at all quenching conditions. In the high-rate domain, the average

slope increased to 110.6 MPa/s and 91.4 MPa/s, showing an increasingly strong strain rate sensitivity above 100 s⁻¹.

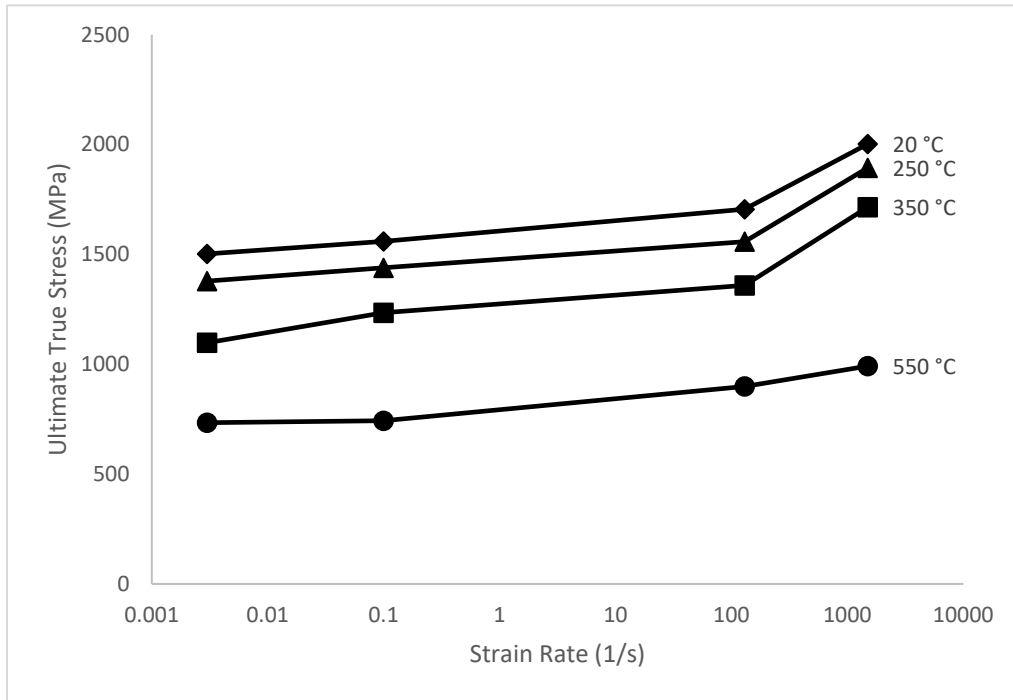


Figure 75 - Ultimate true stress versus strain rate for 1500 MPa PHS.

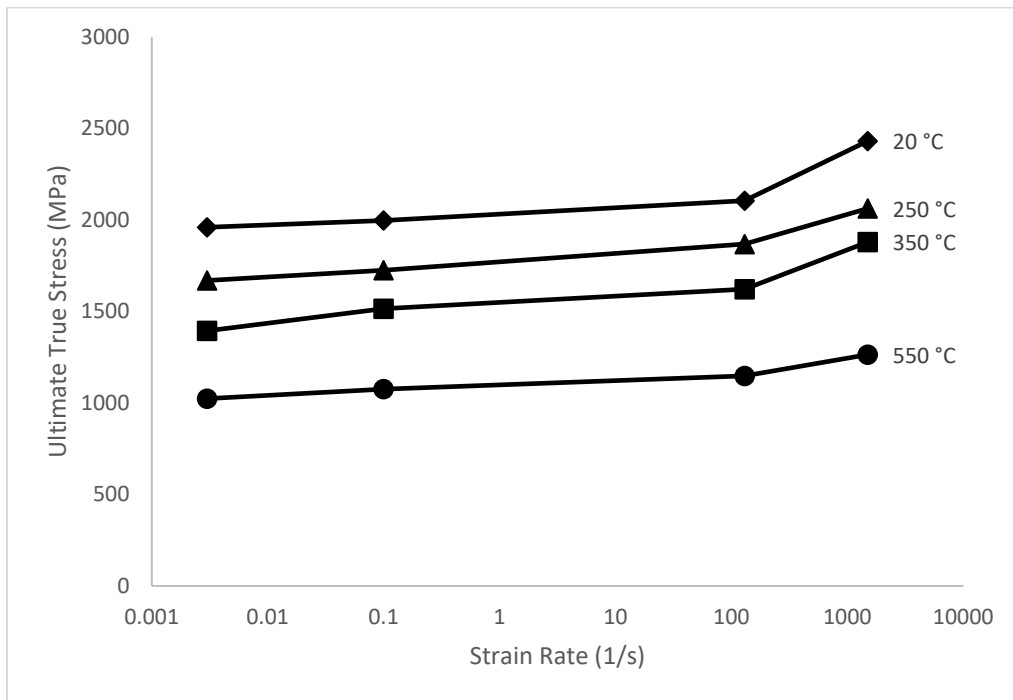


Figure 76 - Ultimate true stress versus strain rate for 2000 MPa PHS.

The flow curves needed to be extended to account for the regions of large deformation in an axial crush test where localized folding occurs. The equivalent strains in regions with localized folding were far beyond those measured in tensile tests; therefore, sheet specimens were prestrained by cold-rolling then tested in uniaxial tension to extend the flow curves. Specimens quenched at 550 °C were used as they can be cold rolled to a much greater degree than any other quenching condition. Figures 77 and 78 show the average results from this series of tensile tests after various levels of prestrain.

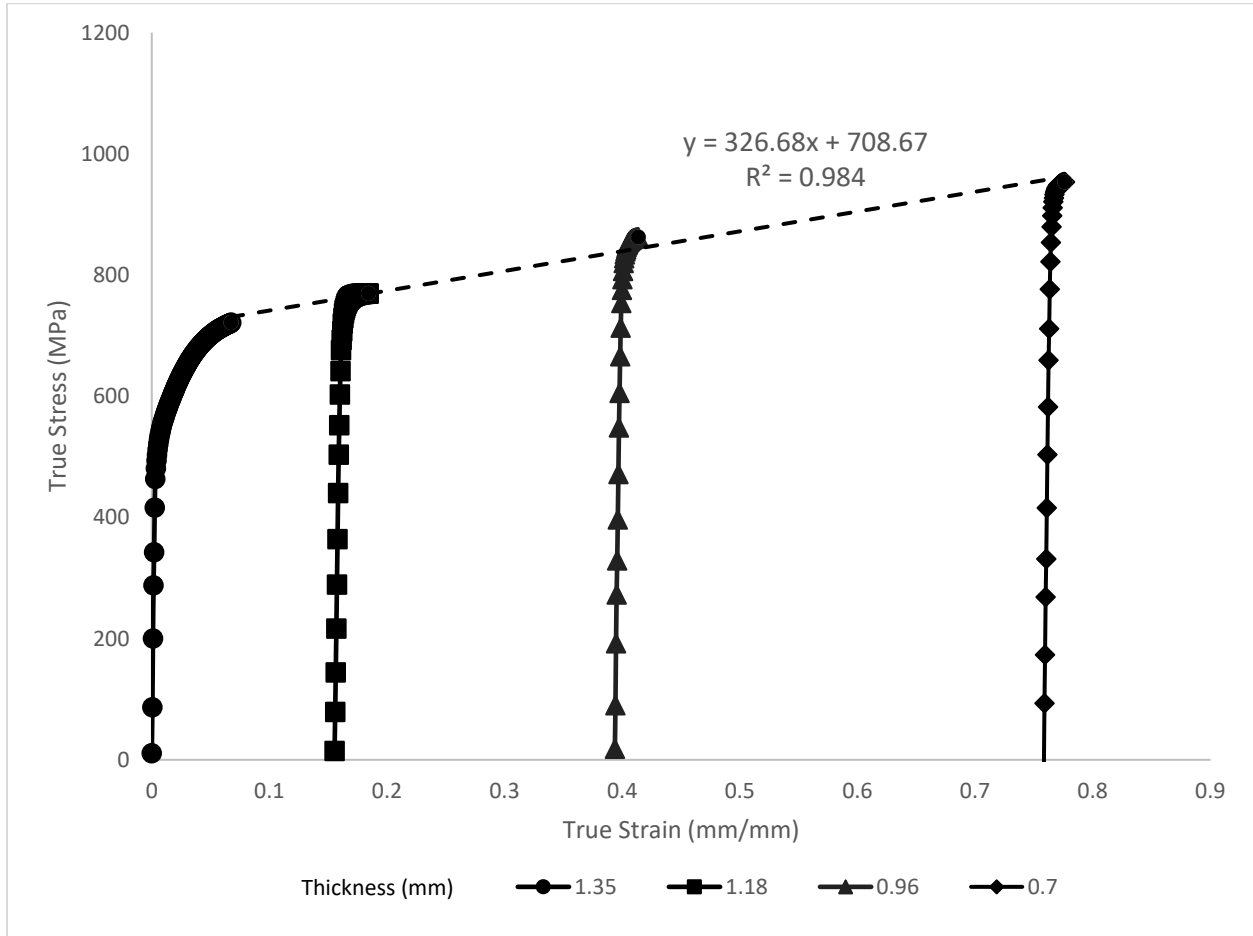


Figure 77 - Extended hardening behaviour of 1500 MPa PHS fitted to a linear function.

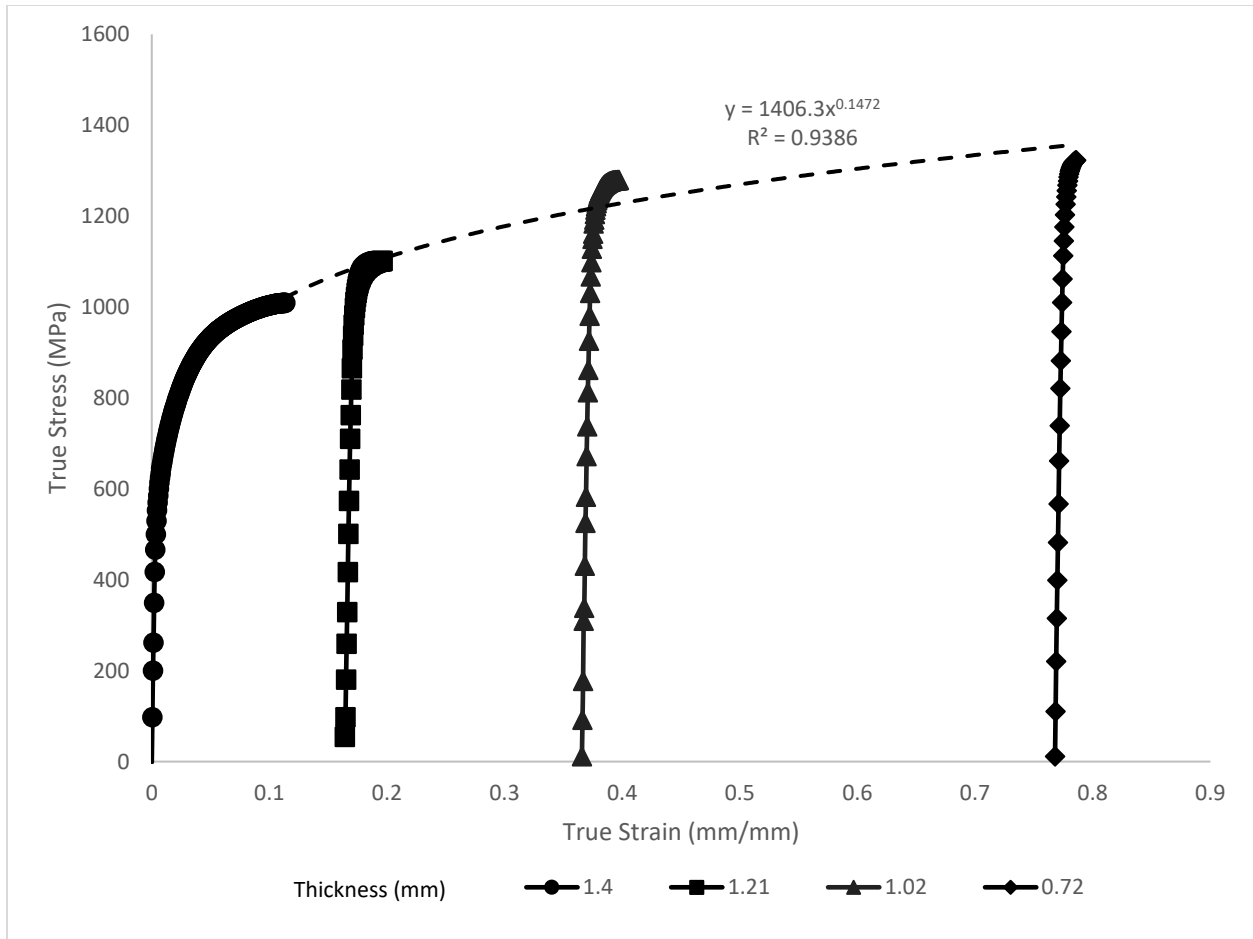


Figure 78 - Extended hardening behaviour of 2000 MPa PHS fitted to an exponential function.

A fitted function was used to fit the extended hardening behaviour of 2000 MPa PHS. Figures 79 and 80 show the final fitted Voce hardening functions and the extended power-law function added to them.

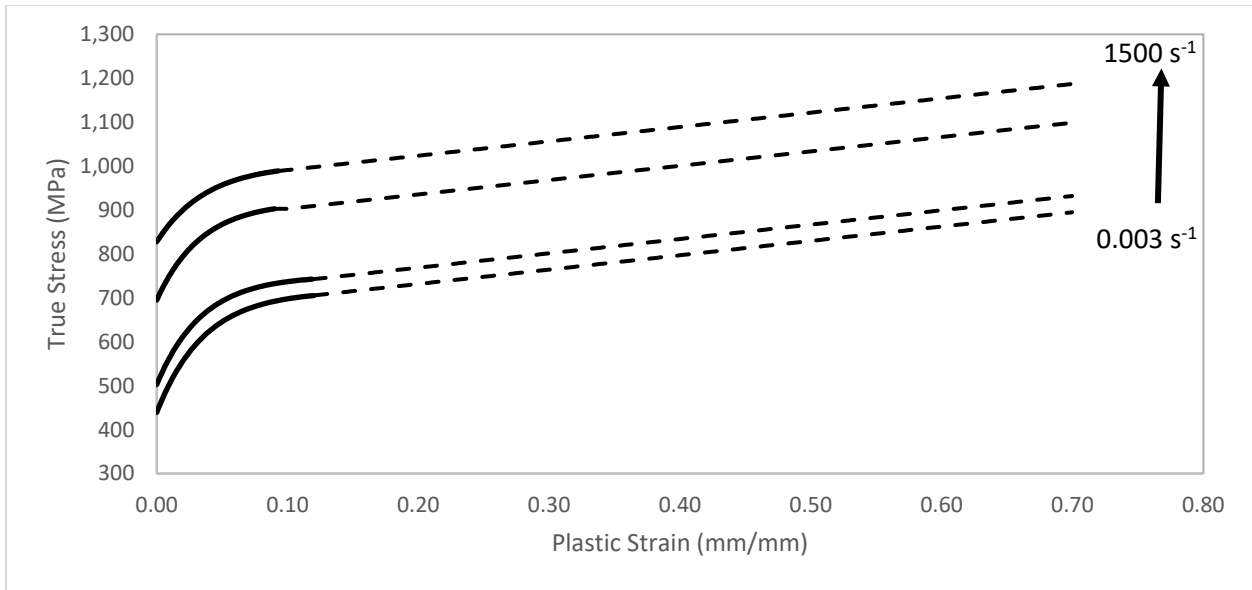


Figure 79 - Extended flow curves for 1500 MPa PHS quenched at 550 °C.

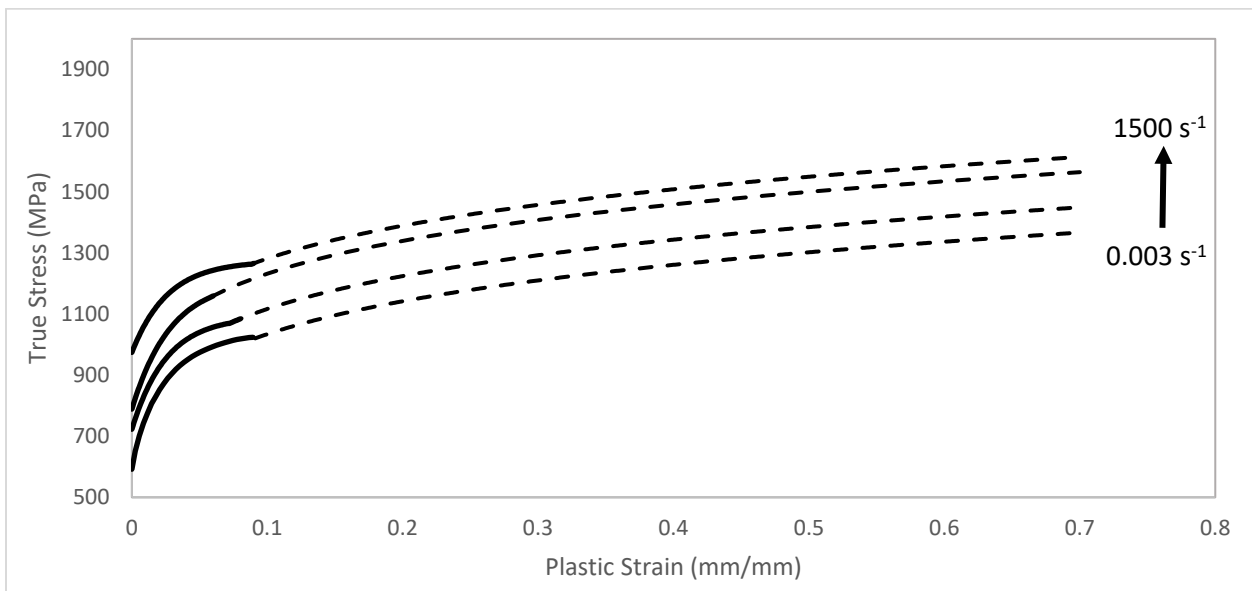


Figure 80 - Extended flow curves for 2000 MPa PHS quenched at 550 °C

5.7 Weld Parameters

The weld trials began using existing weld schedules of 1500 MPa PHS. Alternating changes to the weld schedule and destructive testing were performed, and a final set of weld parameters was obtained which included squeeze time, pre-weld settings, weld settings, hold time, and clamp force. The final parameters are shown in Table 14.

The targeted weld nugget size was 5 mm due to similar industry applications using this value. The average nugget size for the 1500 and 2000 MPa PHS achieved during the welding trials is shown in Tables 15 and 16, respectively.

| <i>Clamp Time (ms)</i> | <i>Pre-weld</i> | | <i>Weld</i> | | <i>Hold Time (ms)</i> | <i>Clamp Force (N)</i> |
|------------------------|-----------------|--------------------|-----------------|--------------------|-----------------------|------------------------|
| 30 | <i>Time (s)</i> | <i>Current (A)</i> | <i>Time (s)</i> | <i>Current (A)</i> | 100 | 2943 |
| | 8 | 12000 | 240 | 8500 | | |

Table 14 - Final weld parameters for 1500 MPa and 2000 MPa PHS.

| <i>Material Quenching Condition</i> | 20 °C | | 250 °C` | | 350 °C | | 550 °C | |
|-------------------------------------|------------|------------|------------|------------|------------|------------|------------|------------|
| <i>Average Nugget Size Extremes</i> | <i>Max</i> | <i>Min</i> | <i>Max</i> | <i>Min</i> | <i>Max</i> | <i>Min</i> | <i>Max</i> | <i>Min</i> |
| | | 6.1 | 5.4 | 6.0 | 5.3 | 6.1 | 5.2 | 6.9 |
| <i>Overall Average Nugget Size</i> | 5.75 | | 5.65 | | 5.65 | | 6.3 | |

Table 15 - Weld nugget sizes of 1500 MPa PHS.

| <i>Material Quenching Condition</i> | 20 °C | | 250 °C` | | 350 °C | | 550 °C | |
|-------------------------------------|------------|------------|------------|------------|------------|------------|------------|------------|
| <i>Average Nugget Size Extremes</i> | <i>Max</i> | <i>Min</i> | <i>Max</i> | <i>Min</i> | <i>Max</i> | <i>Min</i> | <i>Max</i> | <i>Min</i> |
| | | 5.7 | 5.1 | 5.7 | 5.2 | 5.6 | 5.2 | 5.4 |
| <i>Overall Average Nugget Size</i> | 5.4 | | 5.45 | | 5.4 | | 4.95 | |

Table 16 - Weld nugget sizes of 1500 MPa PHS.

The 1500 MPa PHS had a similar nugget size for the 20 °C, 250 °C, 350 °C quenching temperature and a larger nugget size for the 550 °C quenching temperature. The 2000 MPa PHS had a similar trend; however, the 550 °C had a slightly smaller average nugget size.

6. Numerical Model Results

6.1 Uniaxial Tension Model Results

The uniaxial tension model was run at all tested strain rates to validate the material model and the experimental results. In addition, strain rates between the experimental rates were also simulated to show the logarithmic effect of the material model. Figure 81 shows the flow curves of the uniaxial tension model.

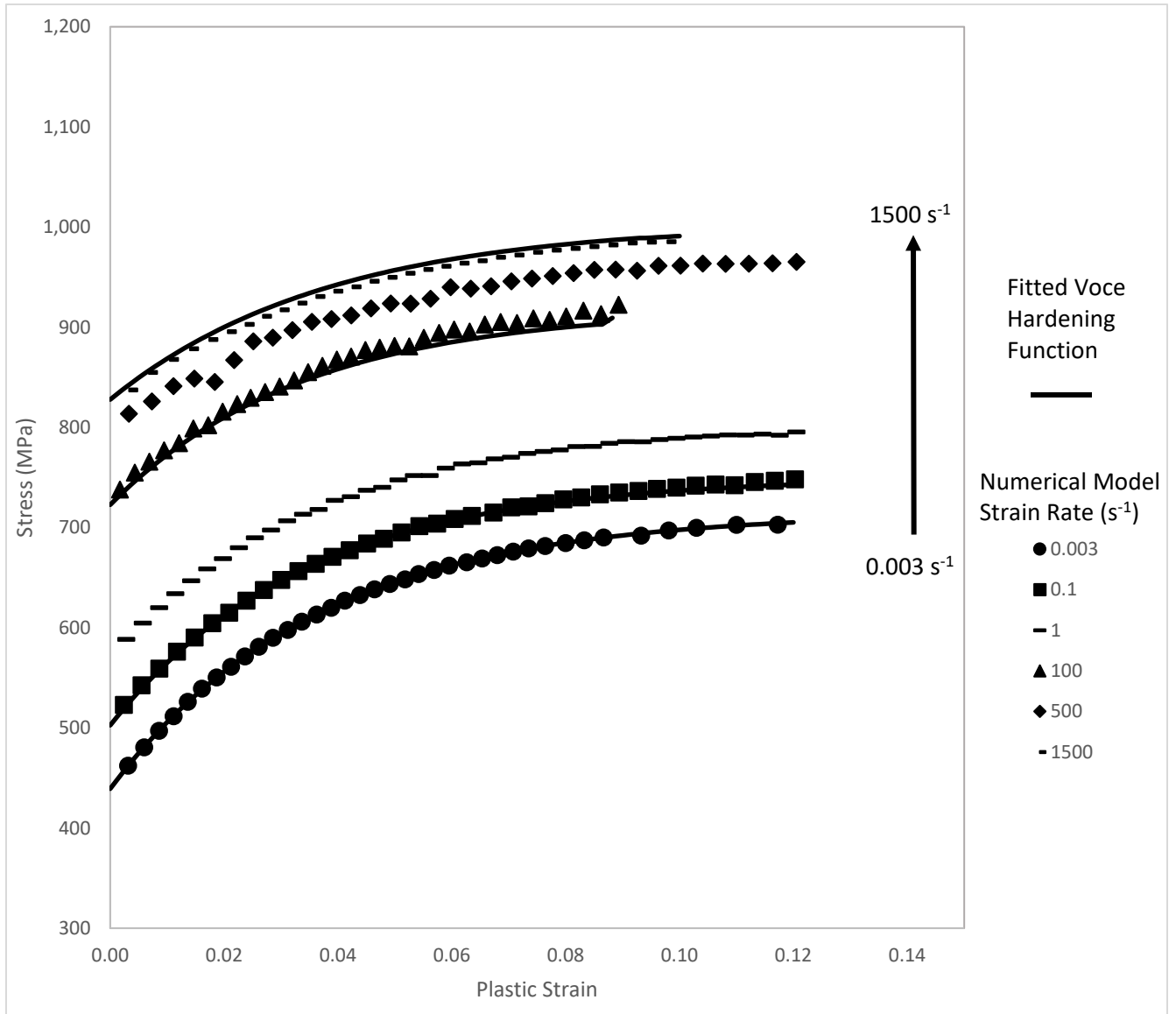


Figure 81 - Numerical predictions of the flow curves of 1500 MPa PHS quenched at 550C in uniaxial tension fitted with a rate-dependent Voce hardening function.

A zero experimental measurement error validation metric was assigned to each set of fitted Voce curves to the numerical result with the same strain rate. The validation metric uses the assumption that the experimental data has no errors in the measurement as to be able to directly compare experimental data to a numerical model. All validation metrics are shown in Table 17. The lowest validation metric was for the 100 s⁻¹ results with a value of 0.9778, indicating a strong correlation between the results of the numerical simulations and the experimental tensile flow curves.

| <i>Strain Rate (s⁻¹)</i> | <i>Validation Metric</i> |
|--|---------------------------------|
| <i>0.003</i> | <i>0.9988</i> |
| <i>0.1</i> | <i>0.9816</i> |
| <i>100</i> | <i>0.9778</i> |
| <i>1500</i> | <i>0.9945</i> |

Table 17 – Validation metric of 1500 MPa PHS.

6.2 Channel Clamping Model Results

To accurately simulated the axial crushing, a preload was first simulated using the channel clamping model. The channel clamping numerical model predicted a different pressure on the 1.4 mm thick 2000 MPa PHS to the 1.36 mm 1500 MPa PHS. The effective stress distribution at the end of each numerical simulation is shown below in Figures 82 and 83.

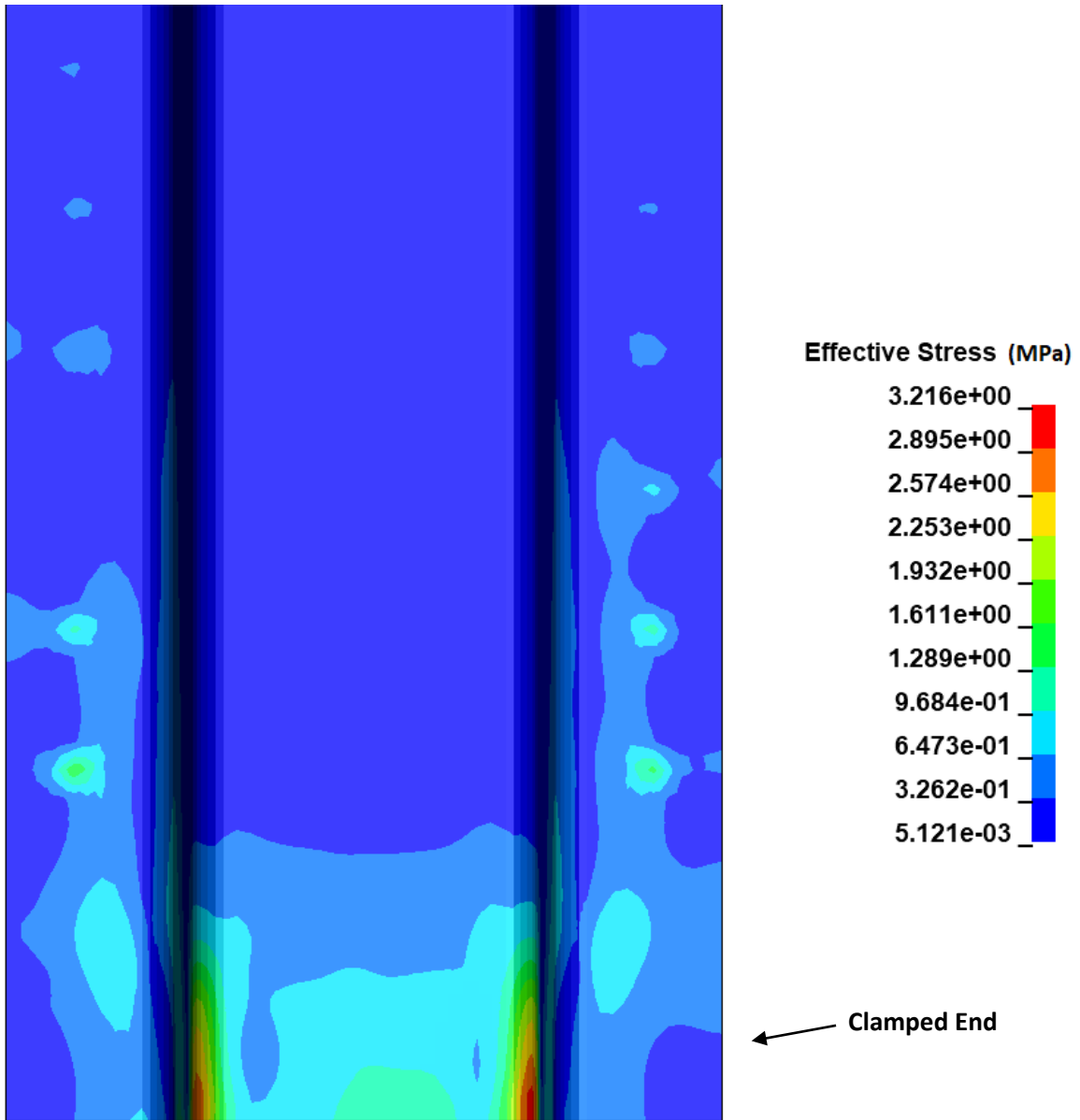


Figure 82 - Clamping simulation effective stress for 1500 MPa PHS.

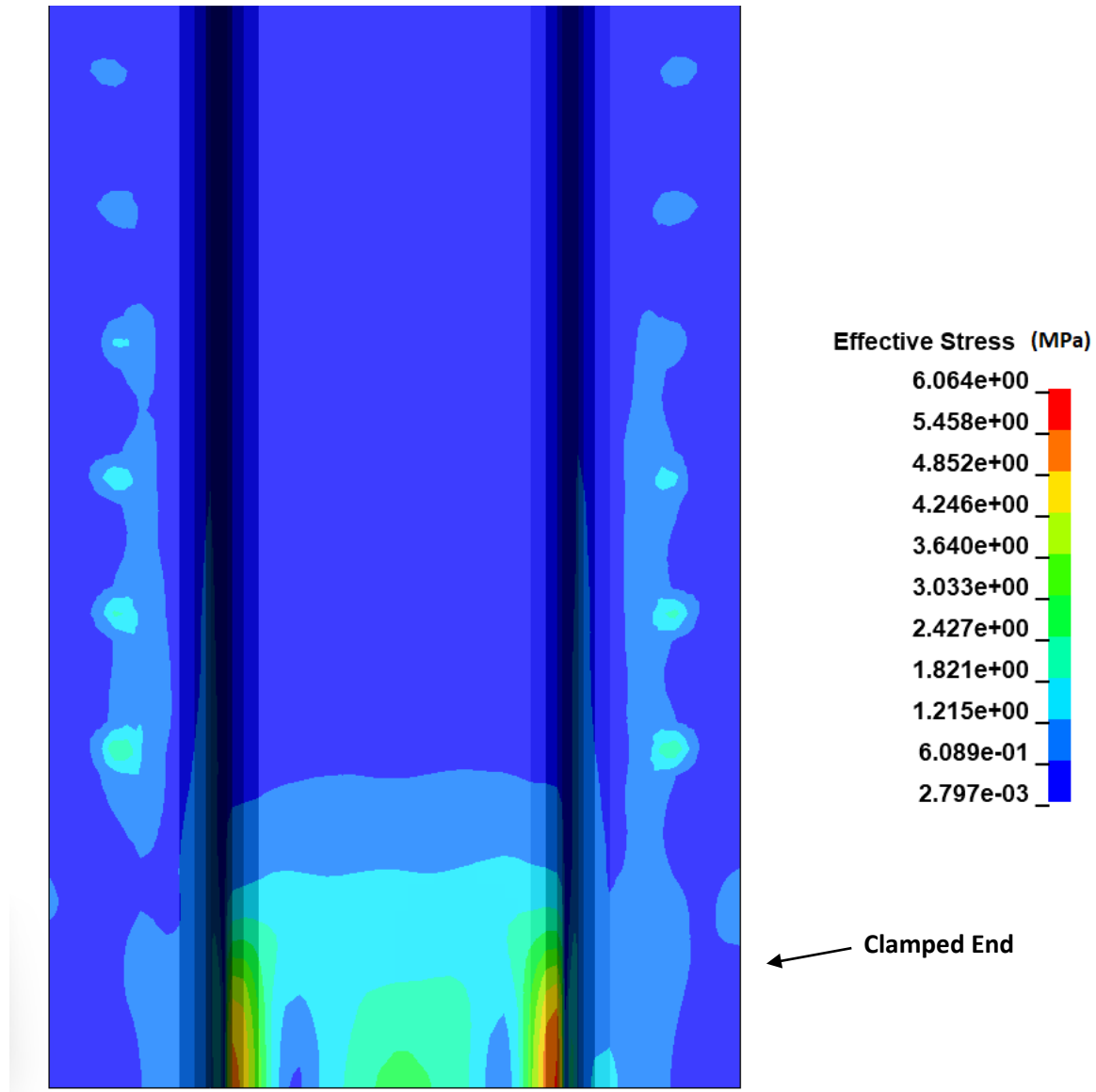


Figure 83 - Clamping simulation effective stress for 2000 MPa PHS.

The thicker 2000 MPa PHS was clamped tighter by the fixture at 606.4 kPa compared to the 1500 MPa PHS that has a maximum clamping pressure of 321.6 kPa. The higher pressure of the 2000 MPa PHS was due to the geometry of the clamping fixture. Since the clamping blocks were made to fit the 1.36 mm thick material, the 1.4 mm material adds a 0.04 mm gap at the flanges and allowed for more deformation of the channel section.

6.3 Axial Crush Model Results

Figure 84 shows a force-displacement curve for the 1500 MPa PHS with a projectile velocity of 25 m/s (4.93 kJ) for the tailored and fully hardened specimens and the absorbed energy during the deformations.

The fully hardened 1500 MPa PHS model exhibited the highest peak force with a value of 977.4 kN, 24.9% higher than the tailored specimen. However, the hardened and tailored specimens exhibited similar absorbed energies being 4.84 kJ and 4.88 kJ, respectively.

Similar to Figure 84, Figure 85 shows the force-displacement curves for the 2000 MPa PHS with a projectile velocity of 25 m/s. The fully hardened 2000 MPa PHS model results exhibited the highest peak force with a value of 1040.1 kN, which was 15.5% higher than the tailored specimen. The hardened and tailored specimens exhibited similar absorbed energies being 4.92 kJ and 4.98 kJ, respectively.

The tailored 2000 MPa PHS results predicted a displacement of 3.29% (16.45 mm) of the length of the original channel section. The full hardened results predicted a displacement of 2.21% (11.05 mm).

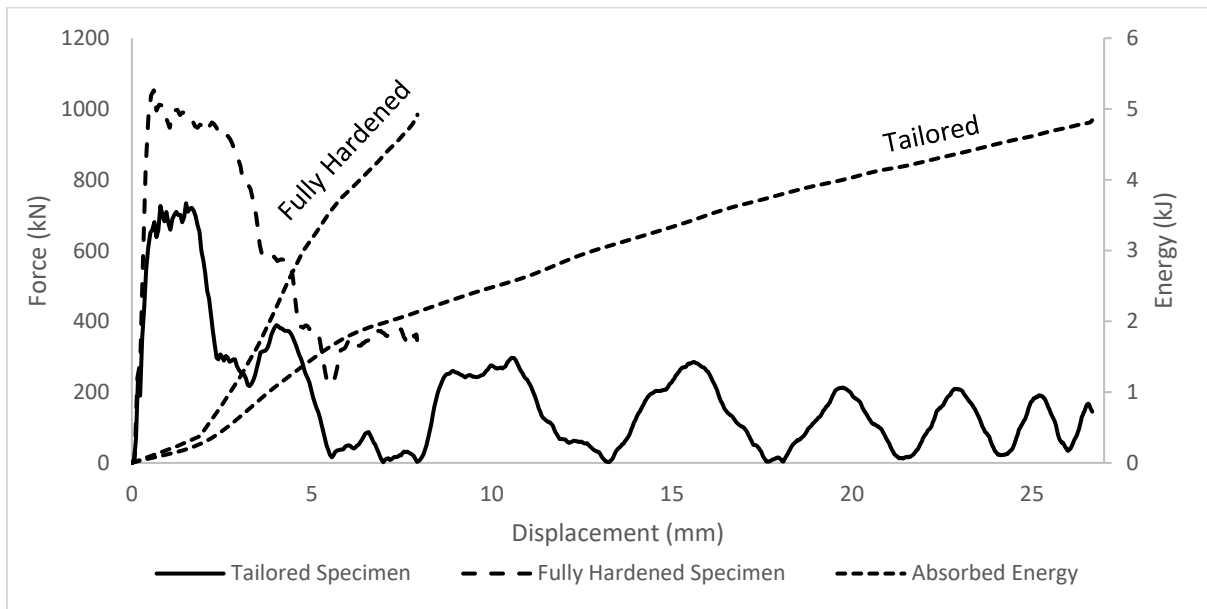


Figure 84 - Predicted force-displacement and energy absorption results for two 1500 MPa PHS channel sections that were quenched differently.

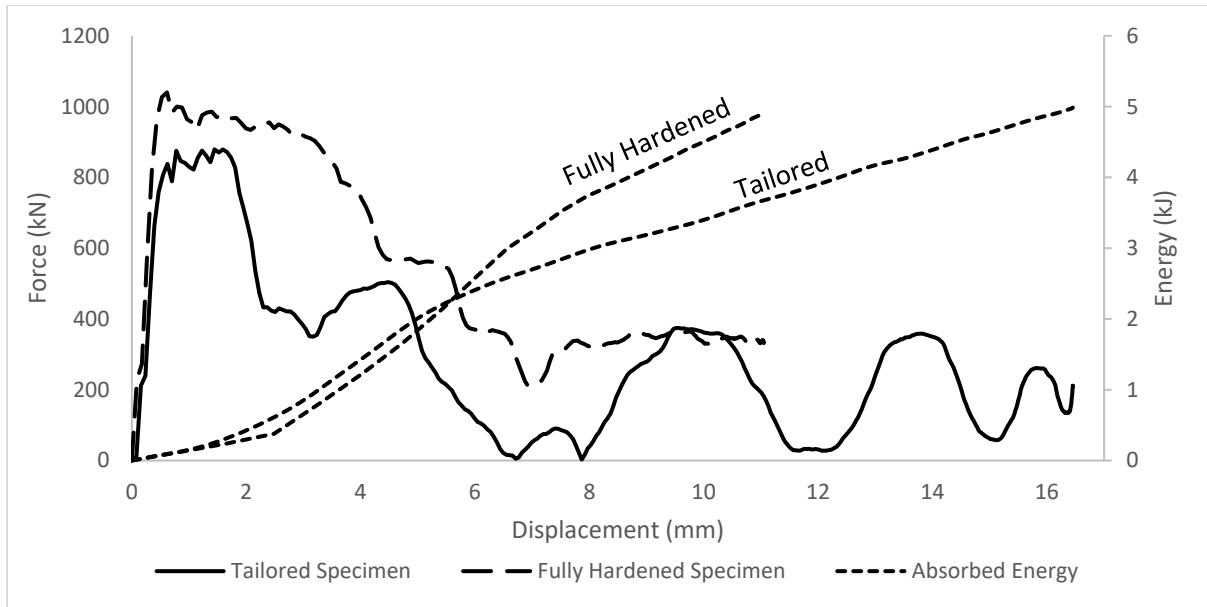


Figure 85 - Predicted force-displacement and energy absorption results for two 2000 MPa PHS channel sections that were quenched differently.

Table 18 shows the crash performance parameters for the numerical models with a 25 m/s projectile speed. The fully hardened models exhibited higher peak forces than the tailored models. The fully hardened 1500 MPa PHS experienced a peak force that was 30.3 % higher than the tailored model of the same material. Likewise, the 2000 MPa PHS experienced a peak force that was 15.5 % higher than the tailored model of the same material. The crush force efficiency was higher for the fully hardened models as the mean forces of the fully hardened models was much higher than the tailored models.

| <i>Specimen</i> | <i>F_{peak} (kN)</i> | <i>TEA (kJ)</i> | <i>SEA(kJ/kg)</i> | <i>F_{mean} (kN)</i> | <i>CFE (%)</i> |
|------------------------------------|------------------------------|-----------------|-------------------|------------------------------|----------------|
| <i>1500 MPa PHS Tailored</i> | <i>733.5</i> | <i>4.84</i> | <i>2.26</i> | <i>126.4</i> | <i>17.2</i> |
| <i>1500 MPa PHS Fully Hardened</i> | <i>1052.7</i> | <i>4.92</i> | <i>2.30</i> | <i>345.3</i> | <i>32.8</i> |
| <i>2000 MPa PHS Tailored</i> | <i>879.1</i> | <i>4.98</i> | <i>2.26</i> | <i>185.1</i> | <i>21.1</i> |
| <i>2000 MPa PHS Fully Hardened</i> | <i>1040.1</i> | <i>4.91</i> | <i>2.23</i> | <i>333.6</i> | <i>32.1</i> |

Table 18 – 25 m/s crash performance parameters.

Figure 86 shows the channels after they have been impacted by the projectile. The legend shows the stress concentrations in each model. The fully tailored channels experienced a localized deformation in the soft zone – specifically around the fold initiator. The fully hardened channels experienced deformation around the fold initiator as well as near the clamped section. Figure 87 shows the channels after a 40 m/s impact.

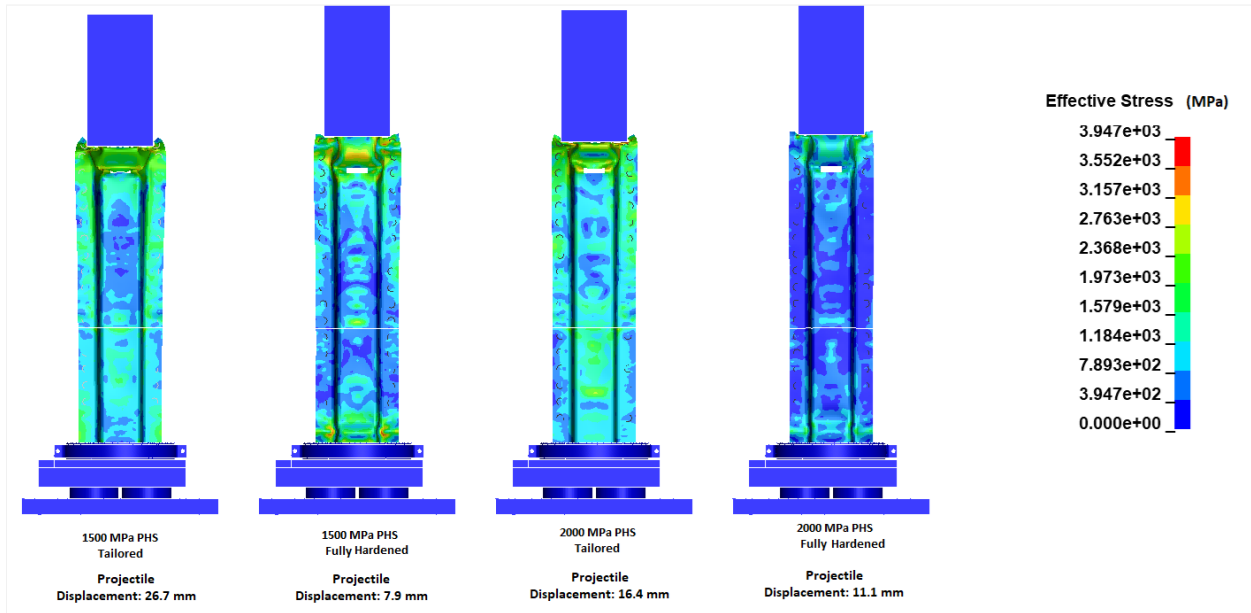


Figure 86 - 25 m/s projectile speed stress results.

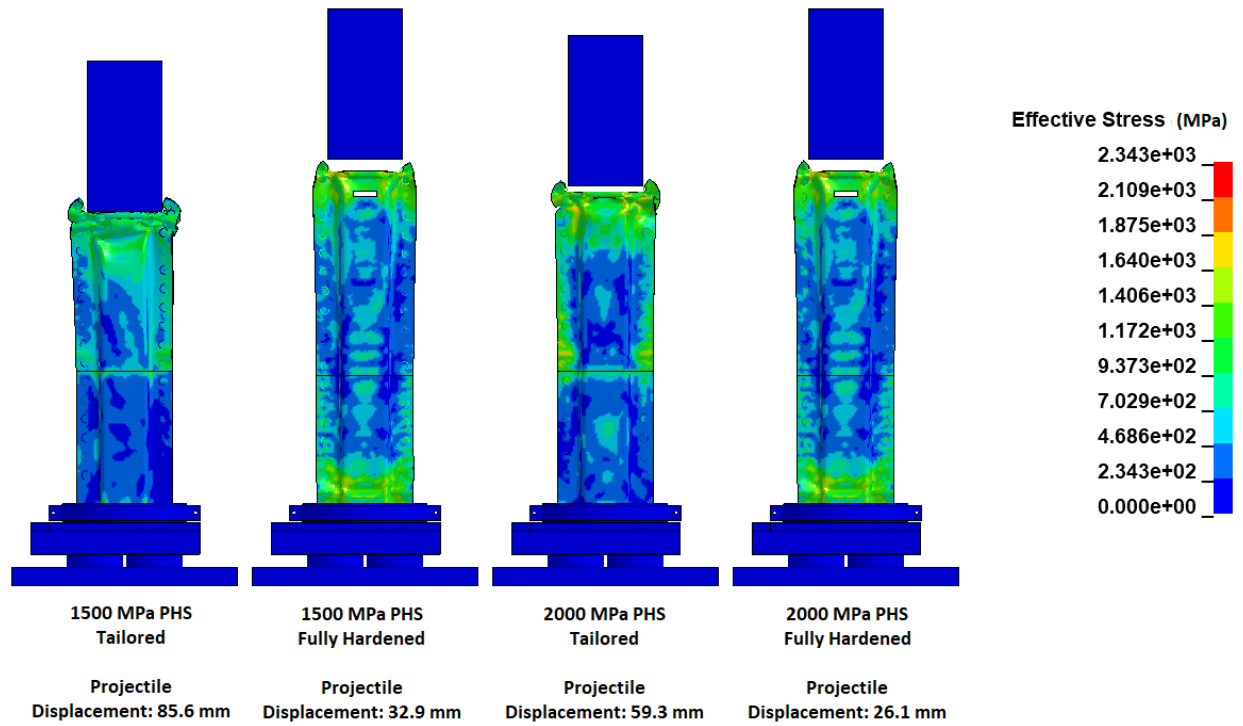


Figure 87 - 40 m/s projectile speed stress results.

Figures 88 and 89 show the force-displacement and energy absorption for the tailored 1500 MPa PHS and 2000 MPa PHS with a projectile speed of 40 m/s (12.59 kJ). For the 1500 MPa PHS, the increased projectile speed produced a peak force of 760.6 kN, which is only a 3.6% increase in force from the 25 m/s projectile speed. There was a significantly higher deformation of 85.6 mm for the 40 m/s projectile speed.

The tailored 2000 MPa PHS model with a projectile speed of 40 m/s observed a peak force of 945.7 kN, a 7.04% increase from the 25 m/s projectile speed. The model predicted a 59.3 mm deformation.

The 1500 MPa and the 2000 MPa predicted similar absorbed energies in all cases. The absorbed energy for the tailored 25 m/s projectile speed was 4.81 kJ and 4.98 kJ, respectively. For the tailored 40 m/s results, the absorbed energies were 12.3 kJ and 12.33 kJ, respectively.

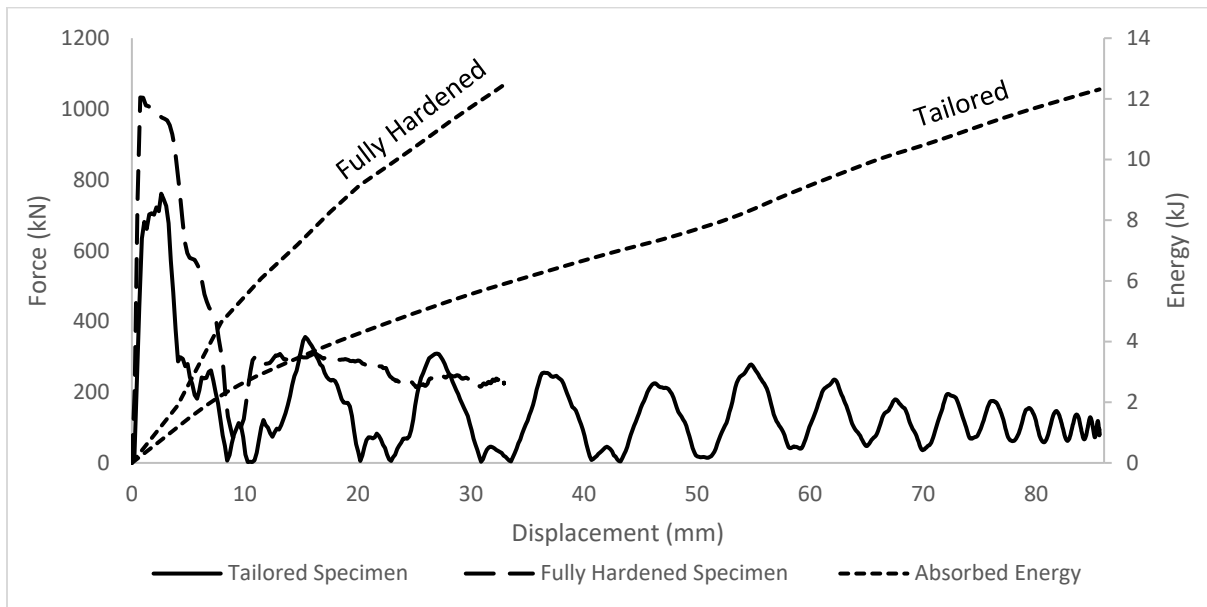


Figure 88 - Force-displacement and energy absorption numerical results with a 40 m/s projectile speed for tailored 1500 MPa PHS.

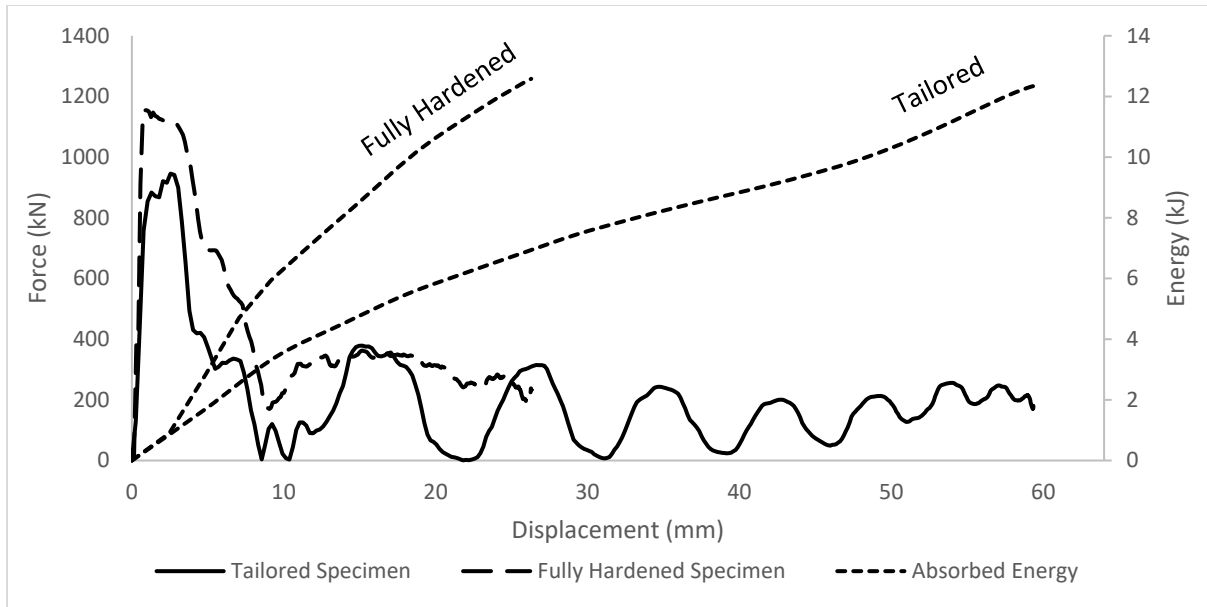


Figure 89 - Force-displacement and energy absorption numerical results with a 40 m/s projectile speed for tailored 2000 MPa PHS.

Table 19 shows the crash performance parameters for the numerical models with a 40 m/s projectile speed. The same general trends were followed from the 25 m/s projectile speed. The fully hardened models exhibited higher peak forces than the tailored models. The fully hardened 1500 MPa PHS experienced a peak force that was 26.3 % higher than the tailored model of the same material. Likewise, the 2000 MPa PHS experienced a peak force that was 18.1 % higher than the tailored model of the same material. The crush force efficiency was higher for the fully hardened models as the mean forces of the fully hardened models was much higher than the tailored models.

| <i>Specimen</i> | <i>F_{peak} (kN)</i> | <i>TEA (kJ)</i> | <i>SEA(kJ/kg)</i> | <i>F_{mean} (kN)</i> | <i>CFE (%)</i> |
|------------------------------------|------------------------------|-----------------|-------------------|------------------------------|----------------|
| <i>1500 MPa PHS Tailored</i> | <i>760.6</i> | <i>12.31</i> | <i>5.74</i> | <i>119.6</i> | <i>15.7</i> |
| <i>1500 MPa PHS Fully Hardened</i> | <i>1032.6</i> | <i>12.45</i> | <i>5.81</i> | <i>250.3</i> | <i>24.2</i> |
| <i>2000 MPa PHS Tailored</i> | <i>945.7</i> | <i>12.34</i> | <i>5.59</i> | <i>172.3</i> | <i>18.2</i> |
| <i>2000 MPa PHS Fully Hardened</i> | <i>1154.5</i> | <i>12.58</i> | <i>5.70</i> | <i>276.1</i> | <i>23.9</i> |

Table 19 – 40 m/s crash performance parameters.

The numerical models were all verified using the total energy of the model as well as the kinetic energy, the internal energy, and the sliding energy. The energy levels were compared (Appendix B.1) to make sure the sum of the kinetic, internal, and sliding energy equals the total energy as well as making sure the total energy of the system remained constant. Lastly the contact energy was monitored to verify that it was

minimal throughout the simulation of the crush test; this confirmed that the contact phenomena were adequately modeled.

7. Conclusions and Recommendations

7.1 Conclusions

The materials, 1500 MPa PHS and 2000 MPa PHS, were characterized by a range of hardness values and strain rates. The experimental results were fitted using hardening functions and used to model axial crush experiments numerically. In general, the axial crush models demonstrated the differences between tailored and nontailored PHS with respect to its crash performance. The tailored channels had lower average crushing force while absorbing similar amounts of energy. The tailored channels localized the deformation much better than the fully hardened channels.

The different microstructures developed for the 1500 MPa PHS and the 2000 MPa PHS were quenched in conditions similar to an industrial hot stamping process. The quenching temperatures covered the operational range of the hot stamping die set (20 °C to 550° C).

For the 1500 MPa PHS, a quenching temperature of 20 °C resulted in a Vickers hardness of approximately 473 HV. The 250 °C, 350 °C, and 550 °C resulted in hardness values of approximately 444 HV, 406 HV, and 225 HV, respectively. For the 2000 MPa PHS, a quenching temperature of 20 °C resulted in a Vickers hardness of approximately 574 HV. The 250 °C, 350 °C, and 550 °C resulted in hardness values of approximately 526 HV, 478 HV, and 297 HV, respectively.

Tensile tests were conducted at strain rates of 0.003 s⁻¹, 0.1 s⁻¹, 100 s⁻¹ and 1500 s⁻¹. The ultimate tensile stress had a logarithmic relationship from quasi-static (0.003 s⁻¹) to intermediate rate tests (100 s⁻¹) with a non-uniform increase at the high rate (1500 s⁻¹) tests. The slope of the logarithmic plots of ultimate true stress versus the strain rate showed that the 1500 MPa PHS and the 2000 MPa PHS had an average slope of 18.9 MPa/s and 17.0 MPa/s respectively, in the quasi-static to intermediate rate domain. In the quasi-static to intermediate rate domain, there existed a sensitivity to strain rate in both materials at all quenching conditions. In the high-rate domain, the average slope increased to 110.6 MPa/s and 91.4 MPa/s, showed an increasingly strong strain rate sensitivity above 100 s⁻¹.

The average flow curves from the experimental results were well fitted and accurately represented by a Voce hardening function. The Voce fitted flow curves were extended beyond the experimental range using consecutive tensile tests and cold rolling to apply a pre-strain. The extended tensile behavior of the 1500 MPa PHS was fitted with a linear function up to a strain of 0.77. The extended tensile behavior of the 2000 MPa PHS was fitted with a power function up to a strain of 0.78.

The 1500 MPa PHS and the 2000 MPa PHS can be welded using the same welding parameters. The 1500 MPa PHS had an average weld nugget size of 5.7 mm for all quenching temperatures except for specimens quenched at 550 °C, which had an average weld nugget size of 6.3 mm. The softer microstructure consisting of ferrite and bainite proved to weld more favorably than the harder microstructures. The more favorable welding in the softer microstructures was not experienced with the 2000 MPa PHS. The 550 °C quenching condition had a nugget size 0.45 mm smaller than the average of the other quenching temperatures.

The numerical models predicted the crash performance of the 1500 MPa PHS and the 2000 MPa PHS at different quenching conditions and different crash speeds. At 25 m/s, the fully hardened 1500 MPa PHS axial crush model predicted a peak force of 1040.1 kN, which was 15.5% higher than the tailored model. The average energy absorption followed the same trend at the peak force. The 2000 MPa PHS followed the same trends as the 1500 MPa PHS with respect to the peak force and average energy absorption.

Crashworthiness parameters were calculated using the numerical models. For the 25 m/s projectile speed the tailored and fully hardened 1500 MPa PHS had crushing force efficiencies of 17.2% and 32.8%, respectively. The tailored and fully hardened 2000 MPa PHS had crushing force efficiencies of 21.1% and 32.1%, respectively. Specific energy absorption was similar for all results at the same projectile velocity as well as the total energy absorption. Although the crushing force efficiency was higher for the fully hardened conditions, the peak force was also higher. The tailored and fully hardened 1500 MPa PHS had peak forces of 733.5 kN and 1052.7 kN, respectively. The tailored and fully hardened 2000 MPa PHS had peak forces of 879.1 kN and 1040.1 kN, respectively. All trends in the 25 m/s projectile velocity models were observed in the 40 m/s projectile velocity models.

7.2 Recommendations

A mechanical extensometer with a gauge length of 9 mm should be used with the video extensometer to characterize the materials at any rate higher than 0.1 s^{-1} . The current system captured the deformation at 75 Hz, which would not be sufficient to capture strain rates of 1 s^{-1} .

Post uniaxial tension behavior was categorized by extending the flow curves with cold rolling. However, cold rolling was not possible with microstructures harder than 300 HV with the rolling mill that was used. Nakazima [30] dome testing can be employed for the harder microstructures to validate the extended flow curve behavior.

Compression testing can be done to further characterize the material with the option of using the *MAT_PLASTICITY_COMPRESSION_TENSION keyword in LS-DYNA to model the compressive behaviour.

There is a significant increase in the ultimate tensile strength between the 100 s^{-1} and the 1500 s^{-1} strain rate tests. To better characterize this behavior, 500 s^{-1} strain rate testing can be performed using the IRTTA. Using equation 14, a tank pressure of 12 psi would result in a projectile speed of approximately 500 s^{-1} . A specimen with a longer gauge length may be implemented to reduce the strain rate of the intermediate rate testing as well as to validate the current mini dogbone tensile specimen to the E8 tensile specimen.

The split Hopkinson pressure bar testing may be further optimized using serrated grip inserts manufactured from a material with a higher hardness value than the hardened O1 tool steel. Tungsten carbide or diamond-coated tools may further reduce the sample from slipping. A sacrificial copper insert has been preliminarily tested and works similarly to the plastic sacrificial damper of the IRTTA. The copper insert reduces the possibility of a misalignment between the striker bar and the impactor.

A GISSMO damage model can be implemented by performing a series of shear, V-bend, and dome testing for both materials and at different hardness values to create failure curves for the same 1500 MPa PHS and 2000 MPa PHS as characterized in this work.

A validated and verified numerical model of the forming process will greatly improve the input geometry and material model to improve the axial crush model. The current model uses the optimally formed part. However, a real part has material thinning and pre-strains involved in the forming process. The forming simulation will also predict the post-forming hardness in each hat section element. Therefore, using a forming simulation as an input to the clamping simulation would be a more realistic input.

Finally, the spotweld material model can be improved by considering failure and the heat-affected zone. For spotweld failure to be characterized, shearing tests can be performed to create a failure curve.

REFERENCES/BIBLIOGRAPHY

- [1] P. Hein and J. Wilsius, "Status and Innovation Trends in Hot Stamping of USIBOR 1500 P," *steel Res. Int.*, vol. 79, no. 2, pp. 85–91, Feb. 2008, doi: 10.1002/SRIN.200806321.
- [2] M. Kleiner, M. Geiger, and A. Klaus, "Manufacturing of lightweight components by metal forming," *CIRP Ann. - Manuf. Technol.*, vol. 52, no. 2, pp. 521–542, 2003, doi: 10.1016/S0007-8506(07)60202-9.
- [3] M. Merklein, M. Wieland, M. Lechner, S. Bruschi, and A. Ghiotti, "Hot stamping of boron steel sheets with tailored properties: A review," *J. Mater. Process. Technol.*, vol. 228, pp. 11–24, Feb. 2016, doi: 10.1016/j.jmatprotec.2015.09.023.
- [4] M. Merklein and T. Svec, "Hot stamping: Manufacturing functional optimized components," *Prod. Eng.*, vol. 7, no. 2–3, pp. 141–151, 2013, doi: 10.1007/s11740-012-0429-z.
- [5] R. Neugebauer, T. Altan, M. Geiger, M. Kleiner, and A. Sterzing, "Sheet metal forming at elevated temperatures," *CIRP Ann. - Manuf. Technol.*, vol. 55, no. 2, pp. 793–816, 2006, doi: 10.1016/j.cirp.2006.10.008.
- [6] H. Karbasian and A. E. Tekkaya, "A review on hot stamping," *J. Mater. Process. Technol.*, vol. 210, no. 15, pp. 2103–2118, Nov. 2010, doi: 10.1016/j.jmatprotec.2010.07.019.
- [7] R. Kolleck, R. Veit, M. Merklein, J. Lechler, and M. Geiger, "Investigation on induction heating for hot stamping of boron alloyed steels," *CIRP Ann. - Manuf. Technol.*, vol. 58, no. 1, pp. 275–278, 2009, doi: 10.1016/j.cirp.2009.03.090.
- [8] G. Venturato, M. Novella, S. Bruschi, A. Ghiotti, and R. Shivpuri, "Effects of Phase Transformation in Hot Stamping of 22MnB5 High Strength Steel," in *Procedia Engineering*, Jan. 2017, vol. 183, pp. 316–321, doi: 10.1016/j.proeng.2017.04.045.
- [9] K. Mori, S. Maki, and Y. Tanaka, "Warm and hot stamping of ultra high tensile strength steel sheets using resistance heating," *CIRP Ann. - Manuf. Technol.*, vol. 54, no. 1, pp. 209–212, 2005, doi: 10.1016/S0007-8506(07)60085-7.

- [10] K. Mori and Y. Okuda, "Tailor die quenching in hot stamping for producing ultra-high strength steel formed parts having strength distribution," *CIRP Ann. - Manuf. Technol.*, vol. 59, no. 1, pp. 291–294, 2010, doi: 10.1016/j.cirp.2010.03.107.
- [11] W. Liang, L. Wang, Y. Liu, Y. Wang, and Y. Zhang, "Hot stamping parts with tailored properties by local resistance heating," in *Procedia Engineering*, 2014, vol. 81, pp. 1731–1736, doi: 10.1016/j.proeng.2014.10.222.
- [12] T. Maeno, K. ichiro Mori, T. Ogihara, and T. Fujita, "Blanking immediately after heating and ultrasonic cleaning for compact hot-stamping systems using rapid resistance heating," *Int. J. Adv. Manuf. Technol.*, vol. 97, no. 9–12, pp. 3827–3837, Aug. 2018, doi: 10.1007/s00170-018-2232-2.
- [13] K. I. Mori, T. Maeno, M. Sakagami, M. Ukai, and Y. Agatsuma, "2-stage progressive-die hot stamping of ultra-high strength steel parts using resistance heating," in *Procedia Engineering*, 2017, vol. 207, pp. 681–686, doi: 10.1016/j.proeng.2017.10.1041.
- [14] K. Mori, T. Maeno, and K. Mongkolkaji, "Tailored die quenching of steel parts having strength distribution using bypass resistance heating in hot stamping," *J. Mater. Process. Technol.*, vol. 213, no. 3, pp. 508–514, 2013, doi: 10.1016/j.jmatprotec.2012.10.005.
- [15] C. Peister *et al.*, "Forming of an axially tailored automotive channel section through hot stamping of tailor-welded blanks," *J. Phys. Conf. Ser.*, vol. 896, no. 1, p. 012052, Sep. 2017, doi: 10.1088/1742-6596/896/1/012052.
- [16] R. George, "Hot Forming of Boron Steels with Tailored Mechanical Properties Experiments and Numerical Simulations," *Thesis, Univ. Waterloo*, 2011.
- [17] M. Merklein, M. Wieland, M. Lechner, S. Bruschi, and A. Ghiotti, "Hot stamping of boron steel sheets with tailored properties: A review," *J. Mater. Process. Technol.*, vol. 228, pp. 11–24, 2016, doi: 10.1016/j.jmatprotec.2015.09.023.
- [18] S. S. Lenze, F. J., J. Banik, "Applications of hot formed parts for body in white," in *International Deep Drawing Research Group IDDRG 511*, 2008, p. 519.
- [19] M. Nikraves, M. Naderi, and G. H. Akbari, "Influence of hot plastic deformation and cooling rate on martensite and bainite start temperatures in 22MnB5 steel," *Mater. Sci. Eng. A*, vol. 540, pp. 24–29, Apr. 2012, doi: 10.1016/j.msea.2012.01.018.

- [20] T. K. Eller *et al.*, "Plasticity and fracture modeling of quench-hardenable boron steel with tailored properties," *J. Mater. Process. Technol.*, vol. 214, no. 6, pp. 1211–1227, 2014, doi: 10.1016/j.jmatprotec.2013.12.015.
- [21] B. Buchmayr and J. S. Kirkaldy, "Mechanical Response of Low Alloy Steels during Cooling from the Austenite Region," *J. Heat Treat*, pp. 127–136, 1990.
- [22] A. Abdollahpoor, X. Chen, M. P. Pereira, N. Xiao, and B. F. Rolfe, "Sensitivity of the final properties of tailored hot stamping components to the process and material parameters," *J. Mater. Process. Technol.*, vol. 228, pp. 125–136, 2016, doi: 10.1016/j.jmatprotec.2014.11.033.
- [23] A. Bardelcik, M. J. Worswick, S. Winkler, and M. A. Wells, "A strain rate sensitive constitutive model for quenched boron steel with tailored properties," *Int. J. Impact Eng.*, vol. 50, pp. 49–62, Dec. 2012, doi: 10.1016/j.ijimpeng.2012.06.007.
- [24] A. C. Thompson, "High Strain Rate Characterization of Advanced High Strength Steels," *Thesis, Univ. Waterloo*, p. 227, 2006.
- [25] A. Bardelcik, "High Strain Rate Behaviour of Hot Formed Boron Steel with Tailored Properties," *Thesis, 2012*.
- [26] M. B. Shkolnikov, "Strain rates in crashworthiness," *Proc. 8th Int. LS-Dyna Users Conf. Troy, MI, USA*, no. 1, pp. 9–20, 2004.
- [27] C. O'Keefe, "Investigation of Resistance Spot Weld Failure in Tailored Hot Stamped Assemblies," *Thesis, Univ. Waterloo*, p. 183, 2018.
- [28] Standard Test Methods for Tension Testing of Metallic Materials, "Astm E8-04," vol. i, pp. 1–24, 2004, [Online]. Available: www.astm.org.
- [29] F. F. Li, M. W. Fu, J. P. Lin, and X. N. Wang, "Experimental and theoretical study on the hot forming limit of 22MnB5 steel," *Int. J. Adv. Manuf. Technol.*, vol. 71, no. 1–4, pp. 297–306, Mar. 2014, doi: 10.1007/s00170-013-5468-x.
- [30] K. H. Nakazima, Koe, Toshio Kikuma, "Study on the formability of steel sheets," *YAWATA TECH REP*, no. 264-- , pp. 8517–8530.

- [31] L. ten Kortenaar, "Failure Characterization of Hot Formed Boron Steels with Tailored Mechanical Properties," *Thesis, Univ. Waterloo*, 2016, Accessed: Nov. 02, 2021. [Online]. Available: <https://uwspace.uwaterloo.ca/handle/10012/10351>.
- [32] T. K. Eller *et al.*, "Plasticity and fracture modeling of the heat-affected zone in resistance spot welded tailor hardened boron steel," *J. Mater. Process. Technol.*, vol. 234, pp. 309–322, Aug. 2016, doi: 10.1016/j.jmatprotec.2016.03.026.
- [33] M. Pouranvari, "Fracture toughness of martensitic stainless steel resistance spot welds," *Mater. Sci. Eng. A*, vol. 680, pp. 97–107, Jan. 2017, doi: 10.1016/j.msea.2016.10.088.
- [34] Y. Zhao, Y. Zhang, and X. Lai, "Analysis of Fracture Modes of Resistance Spot Welded Hot-Stamped Boron Steel," *Metals (Basel)*, vol. 8, no. 10, p. 764, Sep. 2018, doi: 10.3390/met8100764.
- [35] X. Sun, E. V. Stephens, and M. A. Khaleel, "Effects of fusion zone size and failure mode on peak load and energy absorption of advanced high-strength steel spot welds," *Weld. J. (Miami, Fla)*, vol. 86, no. 1, 2007.
- [36] Y. Xiang, Q. Wang, Z. Fan, and H. Fang, "Optimal crashworthiness design of a spot-welded thin-walled hat section," *Finite Elem. Anal. Des.*, vol. 42, no. 10, pp. 846–855, Jun. 2006, doi: 10.1016/j.finel.2006.01.001.
- [37] B. T. Tang, S. Bruschi, A. Ghiotti, and P. F. Bariani, "Numerical modelling of the tailored tempering process applied to 22MnB5 sheets," *Finite Elem. Anal. Des.*, vol. 81, pp. 69–81, Apr. 2014, doi: 10.1016/j.finel.2013.11.009.
- [38] B. Zhu, Z. Liu, Y. Wang, B. Rolfe, L. Wang, and Y. Zhang, "Application of a Model for Quenching and Partitioning in Hot Stamping of High-Strength Steel," *Metall. Mater. Trans. A Phys. Metall. Mater. Sci.*, vol. 49, no. 4, pp. 1304–1312, Apr. 2018, doi: 10.1007/s11661-018-4484-8.
- [39] P. Hu, D. Shi, L. Ying, G. Shen, and W. Liu, "The finite element analysis of ductile damage during hot stamping of 22MnB5 steel," *Mater. Des.*, vol. 69, pp. 141–152, Mar. 2015, doi: 10.1016/j.matdes.2014.12.044.
- [40] K. Omer, "Development and Testing of a Hot Stamped Axial Crush Member with Tailored Properties," *Thesis, University of Waterloo*, 2014.

- [41] P. Åkerström, B. Wikman, and M. Oldenburg, "INSTITUTE OF PHYSICS PUBLISHING MODELLING AND SIMULATION IN MATERIALS SCIENCE AND ENGINEERING Modelling Simul Material parameter estimation for boron steel from simultaneous cooling and compression experiments," *Mater. Sci. Eng*, vol. 13, pp. 1291–1308, 2005, doi: 10.1088/0965-0393/13/8/007.
- [42] E. Voce, "E. Voce, *J. Inst. Met.*, vol. 74, pp. 537-562, 1948. [68]," *J. Inst. Met.*, vol. 74, pp. 537–562, 1948.
- [43] Y. Prajogo, "Hot Stamping of a Boron Steel Side Impact Beam with Tailored Flange Properties - Experiments and Numerical Simulations," *Thesis*, p. 125, 2015, Accessed: Mar. 22, 2020. [Online]. Available:
https://uwspace.uwaterloo.ca/bitstream/handle/10012/9784/Prajogo_Yonathan.pdf?sequence=3.
- [44] M. Bari, "A finite element study of shell and solid element performance in crash-box simulations," 2015. Accessed: Mar. 24, 2020. [Online]. Available: www.hv.se.
- [45] M. Langseth, O. S. Hopperstad, and T. Berstad, "Crashworthiness of aluminum extrusions: Validation of numerical simulation, effect of mass ratio and impact velocity," *Int. J. Impact Eng.*, vol. 22, no. 9, pp. 829–854, Oct. 1999, doi: 10.1016/S0734-743X(98)00070-0.
- [46] J. O. Hallquist, "LS-DYNA® THEORY MANUAL," 2006. Accessed: Feb. 11, 2020. [Online]. Available: www.lstc.com.
- [47] P. Samadian, C. O'Keefe, C. Butcher, and M. J. Worswick, "Fracture Response in Hot-Stamped Tailor-Welded Blanks of Ductibor® 500-AS and Usibor® 1500-AS: Experiments and Modelling," *Eng. Fract. Mech.*, vol. 253, no. June, p. 107864, 2021, doi: 10.1016/j.engfracmech.2021.107864.
- [48] C. Peister, "Axial Crush Performance of Hot Stamped Tailor Welded Blanks," *Thesis, Univ. Waterloo*, 2019.
- [49] T. M. Link and B. M. Hance, "Axial and bending crash performance of advanced high-strength steels," *Int. Symp. New Dev. Adv. High-Strength Sheet Steels*, no. January 2017, pp. 19–30, 2017.
- [50] F. Xu, G. Sun, G. Li, and Q. Li, "Crashworthiness design of multi-component tailor-welded blank (TWB) structures," *Struct. Multidiscip. Optim.*, vol. 48, no. 3, pp. 653–667, Apr. 2013, doi: 10.1007/s00158-013-0916-7.

- [51] J. Magliaro, W. Altenhof, A. Gudisey, and A. Shakib, "Energy dissipation characteristics for AA6061 extrusions subjected to hybrid cutting/clamping at impact velocities up to 32 m/s," *Int. J. Mech. Sci.*, vol. 208, no. April, p. 106678, 2021, doi: 10.1016/j.ijmecsci.2021.106678.
- [52] A. Radzi *et al.*, "Impact Response of Multi-Grooved Square Column," *Mod. Appl. Sci.*, vol. 7, no. 11, 2013, doi: 10.5539/mas.v7n11p12.
- [53] S. S. Hsu and N. Jones, "Quasi-static and dynamic axial crushing of thin-walled circular stainless steel, mild steel and aluminium alloy tubes," *Int. J. Crashworthiness*, vol. 9, no. 2, pp. 195–217, 2004, doi: 10.1533/ijcr.2004.0282.
- [54] F. Neukamm, M. Feucht, and A. Haufe, "Consistent damage modelling in the process chain of forming to crashworthiness simulations," *LS-DYNA Anwenderforum*, vol. 30, pp. 11–20, 2008.
- [55] A. Haufe, M. Feucht, F. Neukamm, and P. Dubois, "Recent Enhancements to the GISSMO Failure Model in LS-DYNA." Accessed: Apr. 22, 2020. [Online]. Available: <http://www.dynamore.de>.
- [56] P. Samadian, L. ten Kortenaar, K. Omer, C. Butcher, and M. J. Worswick, "Fracture characterization of tailored Usibor® 1500-AS and damage modelling based on a coupled-micromechanical-phenomenological strategy," *Eng. Fract. Mech.*, vol. 223, no. July 2019, p. 106785, 2020, doi: 10.1016/j.engfracmech.2019.106785.
- [57] M. Dunand and D. Mohr, "Optimized butterfly specimen for the fracture testing of sheet materials under combined normal and shear loading," *Eng. Fract. Mech.*, vol. 78, no. 17, pp. 2919–2934, 2011, doi: 10.1016/j.engfracmech.2011.08.008.
- [58] "ISO - ISO 16630:2017 - Metallic materials — Sheet and strip — Hole expanding test." Accessed: Feb. 01, 2022. [Online]. Available: <https://www.iso.org/standard/69771.html>.
- [59] K. Cheong, K. Omer, C. Butcher, R. George, and J. Dykeman, "Evaluation of the VDA 238-100 Tight Radius Bending Test using Digital Image Correlation Strain Measurement," *J. Phys. Conf. Ser.*, vol. 896, no. 1, 2017, doi: 10.1088/1742-6596/896/1/012075.
- [60] A. L. Gurson, "Continuum Theory of Ductile Rupture By Void Nucleation and Growth - 1. Yield Criteria and Flow Rules for Porous Ductile Media.," *Am. Soc. Mech. Eng.*, no. 76-Mat-CC, 1976.

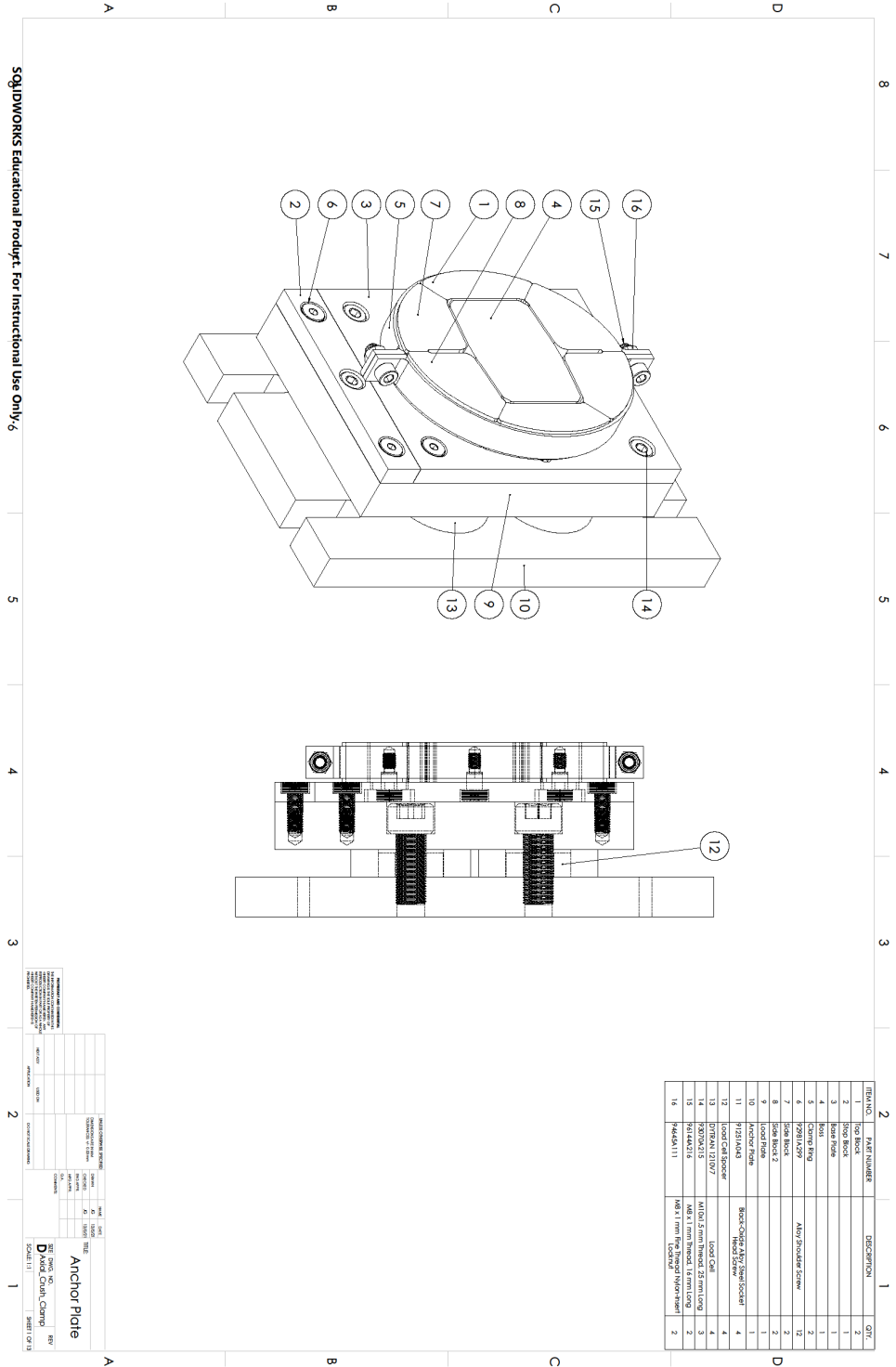
- [61] G. R. Johnson and W. H. Cook, "A Computational Constitutive Model and Data for Metals Subjected to Large Strain, High Strain Rates and High Pressures," *Seventh Int. Symp. Ballist.*, pp. 541–547, 1983.
- [62] G. R. Johnson and W. H. Cook, "Fracture characteristics of three metals subjected to various strains, strain rates, temperatures and pressures," *Eng. Fract. Mech.*, vol. 21, no. 1, pp. 31–48, Jan. 1985, doi: 10.1016/0013-7944(85)90052-9.
- [63] M. Tummers *et al.*, "Introduction of a 1000 MPa crush tip within a Usibor® 1500-AS axial crush rail using in-die heated hot stamping," *IOP Conf. Ser. Mater. Sci. Eng.*, vol. 418, no. 1, 2018, doi: 10.1088/1757-899X/418/1/012126.
- [64] Y. C. Lin and X. M. Chen, "A critical review of experimental results and constitutive descriptions for metals and alloys in hot working," *Mater. Des.*, vol. 32, no. 4, pp. 1733–1759, 2011, doi: 10.1016/j.matdes.2010.11.048.
- [65] I. S. Sarraf, "Flow curve and constitutive equation parameters," pp. 2–47, 2015.
- [66] Y. C. Lin, X. M. Chen, and G. Liu, "A modified Johnson-Cook model for tensile behaviors of typical high-strength alloy steel," *Mater. Sci. Eng. A*, vol. 527, no. 26, pp. 6980–6986, 2010, doi: 10.1016/j.msea.2010.07.061.
- [67] A. Jenab, I. Sari Sarraf, D. E. Green, T. Rahmaan, and M. J. Worswick, "The Use of genetic algorithm and neural network to predict rate-dependent tensile flow behaviour of AA5182-sheets," *Mater. Des.*, vol. 94, pp. 262–273, 2016, doi: 10.1016/j.matdes.2016.01.038.
- [68] I. S. Sarraf, A. Jenab, K. P. Boyle, and D. E. Green, "Effect of rate-dependent constitutive equations on the tensile flow behaviour of DP600 using Rousselier damage model," *Mater. Des.*, vol. 117, pp. 267–279, 2017, doi: 10.1016/j.matdes.2016.12.088.
- [69] X. Zhuang, Z. Zhao, H. Li, and H. Xiang, "Experimental methodology for obtaining the flow curve of sheet materials in a wide range of strains," *Steel Res. Int.*, vol. 84, no. 2, pp. 146–154, 2013, doi: 10.1002/srin.201200104.
- [70] I. S. Sarraf and D. E. Green, "A numerical method to predict the rate-sensitive hardening behaviour of sheet materials using uniaxial and biaxial flow curves," *IOP Conf. Ser. Mater. Sci. Eng.*, vol. 418, no. 1, 2018, doi: 10.1088/1757-899X/418/1/012087.

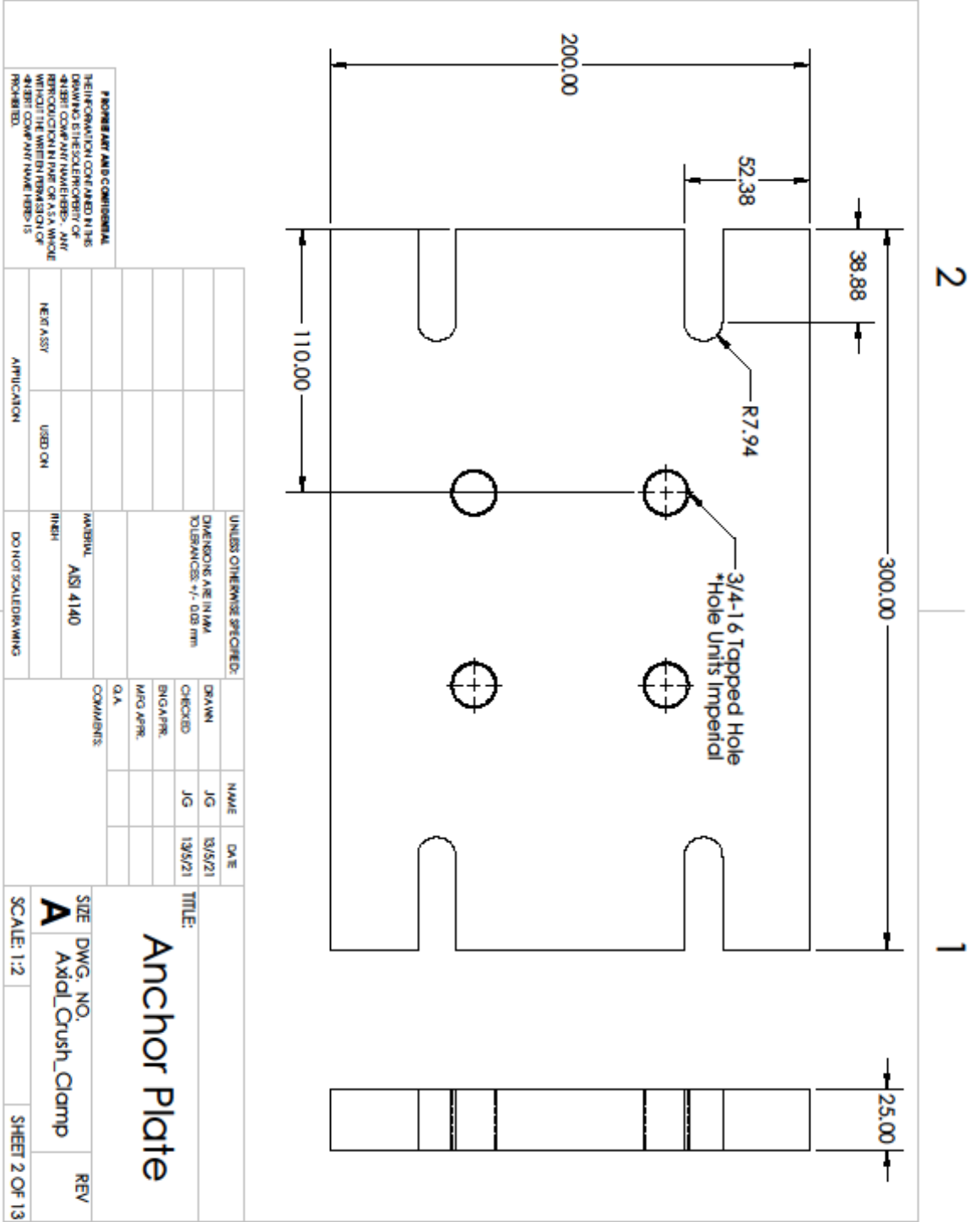
- [71] A. S. Khan, Y. S. Suh, and R. Kazmi, "Quasi-static and dynamic loading responses and constitutive modeling of titanium alloys," *Int. J. Plast.*, vol. 20, no. 12, pp. 2233–2248, Dec. 2004, doi: 10.1016/J.IJPLAS.2003.06.005.
- [72] R. Smerd, S. Winkler, C. Salisbury, M. Worswick, D. Lloyd, and M. Finn, "High strain rate tensile testing of automotive aluminum alloy sheet," *Int. J. Impact Eng.*, vol. 32, no. 1–4, pp. 541–560, Dec. 2005, doi: 10.1016/J.IJIMPENG.2005.04.013.
- [73] B. S. E. N. Iso, "Resistance welding — Peel and chisel testing of resistance spot and projection welds," *Management*, vol. 3, 2007, Accessed: Feb. 24, 2022. [Online]. Available: www.iso.org.
- [74] J. D. and D. M. F. Beer, E. Johnstron, *Mechanics of Materials*, 6th ed. New York, N.Y.: McGraw Hill, 2012.
- [75] W. L. Oberkampf and T. G. Trucano, "Verification and validation in computational fluid dynamics," *Prog. Aerosp. Sci.*, vol. 38, no. 3, pp. 209–272, Apr. 2002, doi: 10.1016/S0376-0421(02)00005-2.
- [76] J. J. Harrigan, B. Ahonsi, E. Palamidi, and S. R. Reid, "Experimental and numerical investigations on the use of polymer Hopkinson pressure bars," *Philos. Trans. R. Soc. A Math. Phys. Eng. Sci.*, vol. 372, no. 2023, 2014, doi: 10.1098/rsta.2013.0201.
- [77] Y. G. Miao *et al.*, "Determination of dynamic elastic modulus of polymeric materials using vertical split Hopkinson pressure bar," *Int. J. Mech. Sci.*, vol. 108–109, pp. 188–196, 2016, doi: 10.1016/j.ijmecsci.2016.02.005.

APPENDICES

Appendix A. Technical Drawings

A.1 Axial Crush Fixture



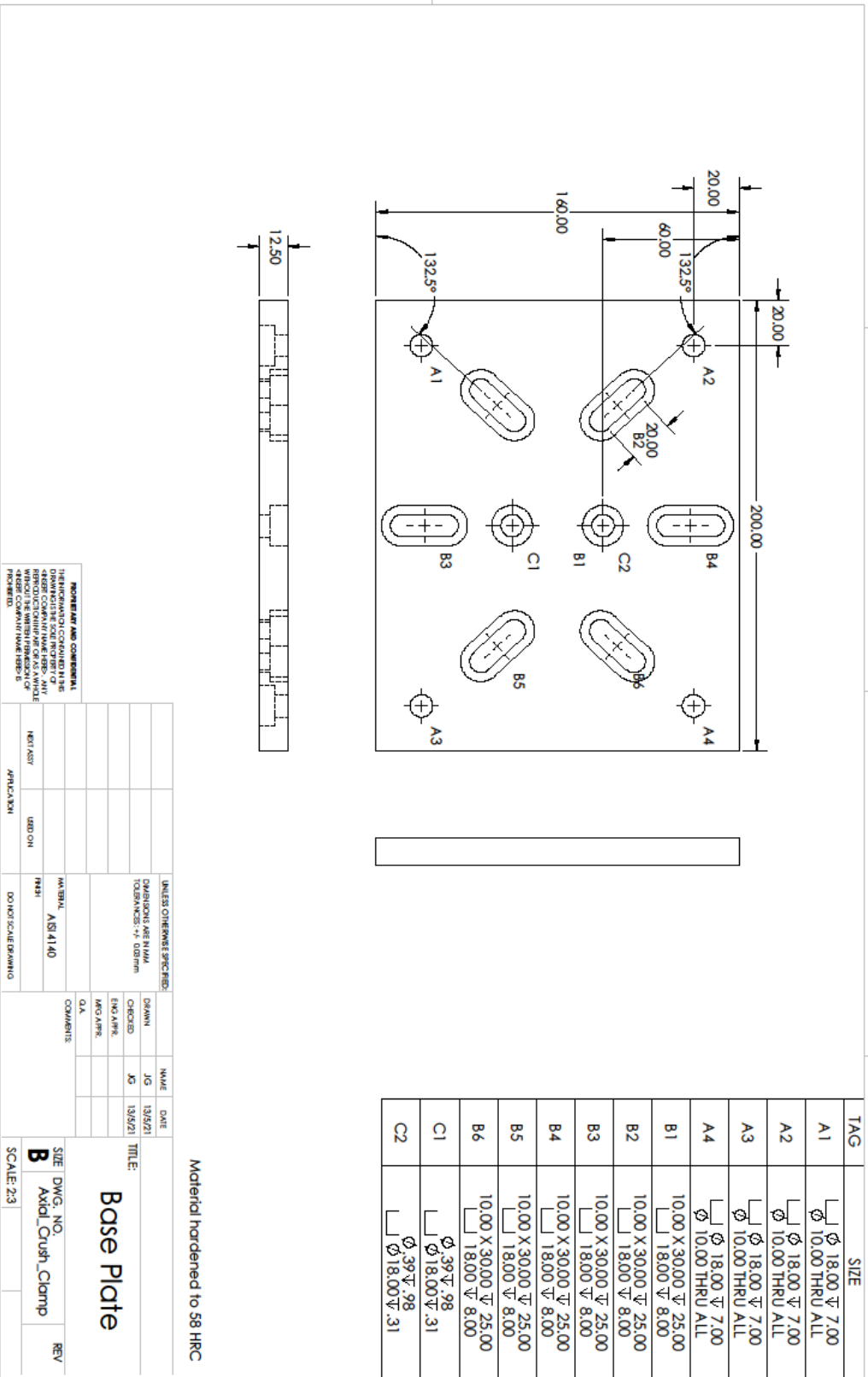


PROPRIETARY AND CONFIDENTIAL
 THE INFORMATION CONTAINED IN THIS
 DRAWING IS THE SOLE PROPERTY OF
 HUBERT COMPANY NUMBERED. ANY
 REPRODUCTION IN PART OR AS A WHOLE
 WITHOUT THE WRITTEN PERMISSION OF
 HUBERT COMPANY NUMBERED IS
 PROHIBITED.

| UNLESS OTHERWISE SPECIFIED: | | MATERIAL | |
|-----------------------------|-------------|----------|-----------|
| DRAWING | ASME Y14.5M | ASST | ASST 4140 |
| TOLERANCES | ±.003 mm | FINISH | |
| DATE | 12/15/21 | COMMENTS | |
| CHECKED | JG | Q.A. | |
| DRAWN | JG | | |
| DATE | 12/15/21 | | |
| APPROVED | | | |
| DATE | | | |
| SCALE | 1:2 | | |

| | | | | |
|--------------|--|---------------|-------------------|-----|
| TITLE: | | SIZE | DWG. NO. | REV |
| Anchor Plate | | A | Axial_Crush_Clamp | |
| SCALE: 1:2 | | SHEET 2 OF 13 | | |

SOLIDWORKS Educational Product For Instructional Use Only.



A

B

4

3

2

1

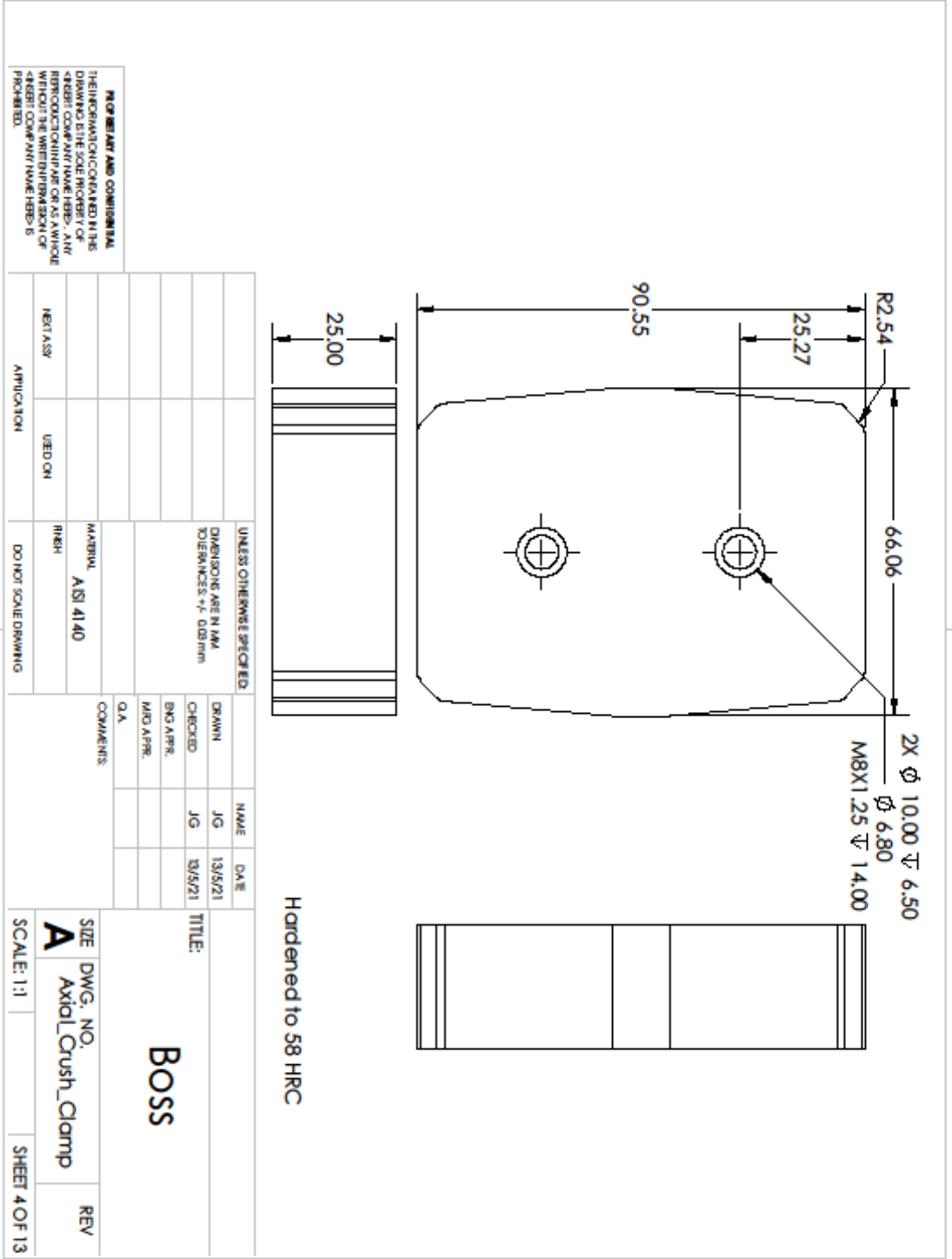
A

B

Material hardened to 58 HRC

| UNLESS OTHERWISE SPECIFIED: | | NAME | DATE |
|-----------------------------|-----------------------|-----------|-------------------|
| DIMENSIONS ARE IN INCH | DECIMALS ARE IN INCH | JG | 13/5/21 |
| TOLERANCES ARE: | FRACTIONS ± .005 INCH | CHECKED | JO |
| | DECIMALS ± .005 INCH | ENG APPR. | |
| | | MG APPR. | |
| | | QA | |
| | | COMMENTS | |
| | | DATE | |
| | | SIZE | DWG. NO. |
| | | | Axial_Crush_Clamp |
| | | SCALE | 2:3 |
| | | REV | |

PROPRIETARY AND CONFIDENTIAL
THIS INFORMATION CONTAINS THE
DESIGN AND CONSTRUCTION OF
A PRODUCT OF THE COMPANY AND IS
THE PROPERTY OF THE COMPANY. IT IS
TO BE KEPT CONFIDENTIAL AND NOT
DISCLOSED TO ANY OTHER PERSON
WITHOUT THE WRITTEN PERMISSION OF
THE COMPANY. (IN THE EVENT OF
PROSECUTION)



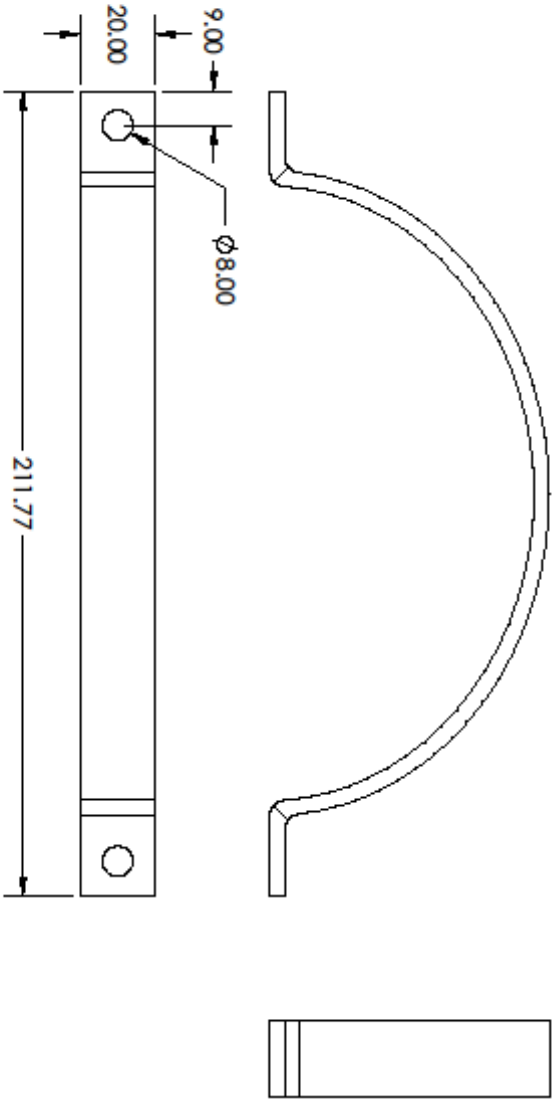
PROPRIETARY AND CONFIDENTIAL
 THE INFORMATION CONTAINED IN THIS
 DRAWING IS THE SOLE PROPERTY OF
 <FIRM COMPANY NAME HERE>. ANY
 REPRODUCTION IN PART OR AS A WHOLE
 WITHOUT THE WRITTEN PERMISSION OF
 <FIRM COMPANY NAME HERE> IS
 PROHIBITED.

| UNLESS OTHERWISE SPECIFIED | | NAME | DATE | TITLE: | SIZE DWG. NO. | REV |
|--|--|---------|---------|-----------|---------------|---------------|
| DIMENSIONS ARE IN MM TOLERANCES: ± 0.08mm | | JG | 13/5/21 | | | |
| MATERIAL: AISI 4140 | | JG | 13/5/21 | | | |
| H8RH | | | | | | |
| DO NOT SCALE DRAWING | | | | | | |
| DRAWN | | | | COMMENTS: | SCALE: 1:1 | SHEET 4 OF 13 |
| CHECKED | | | | | | |
| ENG APPR. | | | | | | |
| MFG APPR. | | | | | | |
| Q.A. | | | | | | |
| NEXT ASSY | | USED ON | | | | |
| APPLICATION | | | | | | |

SOLIDWORKS Educational Product For Instructional Use Only.

2

1

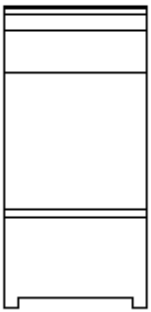
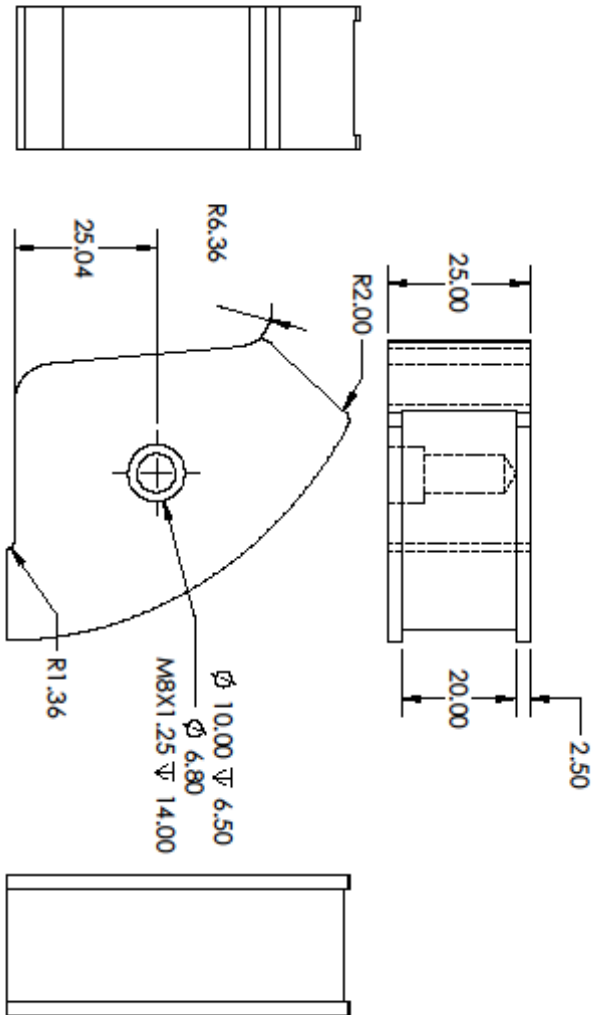


| | | | | |
|---|--|--|--|--|
| <p>PROPRIETARY AND CONFIDENTIAL THE INFORMATION CONTAINED HEREIN IS THE SOLE PROPERTY OF PDS. ANY REPRODUCTION OR TRANSMISSION IN ANY FORM OR BY ANY MEANS, WITHOUT THE WRITTEN PERMISSION OF PDS, IS PROHIBITED.</p> | | <p>UNLESS OTHERWISE SPECIFIED, DIMENSIONS ARE IN MM TOLERANCES: +/- 0.05mm</p> | | <p>NAME: JG DATE: 13/5/21</p> |
| <p>APPLICATION: NEST ASSY</p> | | <p>DO NOT SCALE DRAWING</p> | | <p>CHECKED: JG 13/5/21</p> |
| <p>USED ON:</p> | | <p>MATERIAL: AISI 4140</p> | | <p>ENG APPR:</p> |
| <p>REVISIONS:</p> | | <p>COMMENTS:</p> | | <p>APPROV:</p> |
| <p>SIZE: A</p> | | <p>DWG. NO.: Axial_Crush_Clamp</p> | | <p>REV:</p> |
| <p>SCALE: 2:3</p> | | <p>SHEET 5 OF 13</p> | | |

SOLIDWORKS Educational Product For Instructional Use Only.

2

1



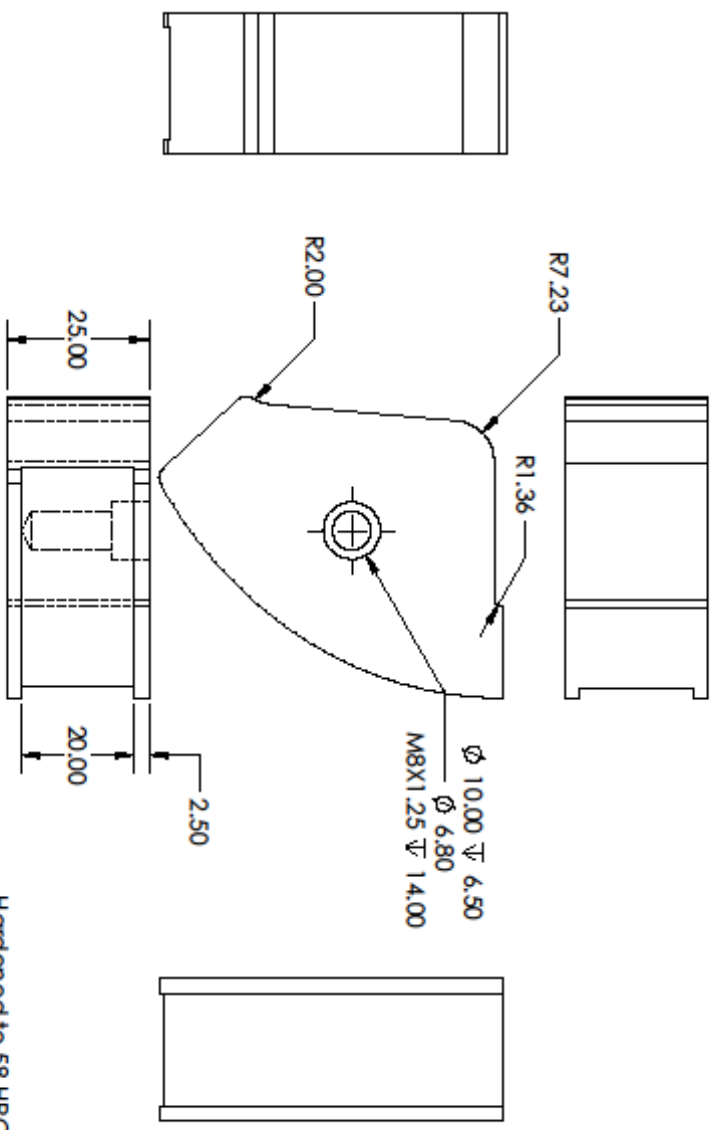
Hardened to 58 HRC

| | | | | | |
|--|----------------|---|---|--------------------------------------|---|
| <p>PROPRIETARY AND CONFIDENTIAL</p> <p>THIS INFORMATION CONTAINS THE DESIGN AND/OR INVENTIVE CONCEPTS OF THE COMPANY AND IS UNLAWFULLY REPRODUCED IN PART OR AS A WHOLE WITHOUT THE WRITTEN PERMISSION OF THE COMPANY. NAME (FED) IS PROTECTED.</p> | | <p>UNLESS OTHERWISE SPECIFIED, DIMENSIONS ARE IN MM TOLERANCES: \pm 0.03mm</p> | | <p>NAME: JG</p> <p>DATE: 13/5/21</p> | <p>TITLE: Side Block</p> |
| <p>NEXT ASSY</p> | <p>USED ON</p> | <p>MATERIAL: AISI 4140</p> <p>FINISH: FINE</p> | <p>DRAWN: JG</p> <p>CHECKED: JG</p> <p>END APPR: JG</p> <p>MFG APPR: JG</p> <p>QA: JG</p> | <p>COMMENTS:</p> | <p>SIZE: DWG. NO. Axial_Crush_Clamp</p> <p>SCALE: 1:1</p> |
| <p>APPLICATION</p> | | <p>DO NOT SCALE DRAWING</p> | <p>REV SHEET 7 OF 13</p> | | |

SOLIDWORKS Educational Product For Instructional Use Only.

2

1



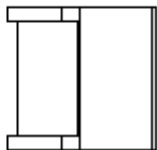
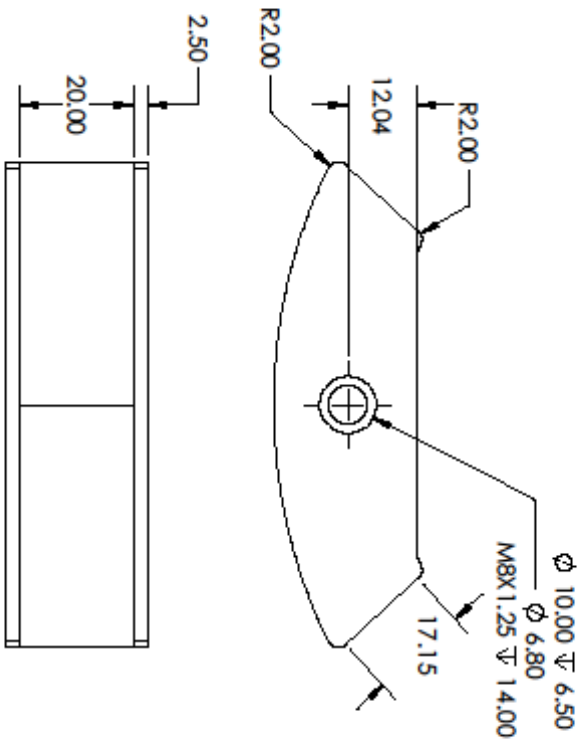
Hardened to 58 HRC

| | | | |
|------------------------------------|---------------------|------------|-------------------|
| UNLESS OTHERWISE SPECIFIED: | | NAME | DATE |
| DIMENSIONS ARE IN MM | | JG | 13/9/21 |
| TOLERANCES: ± 0.03 mm | | CHECKED | JG |
| | | DWG APPR | |
| | | MFG APPR | |
| | | Q.A. | |
| | | COMMENTS: | |
| MATERIAL | | AS14140 | |
| FINISH | | FRESH | |
| NEST ASSY | USED ON | | |
| APPLICATION | DONOT SCALE DRAWING | | |
| PROPERTY AND COMMERCIAL | | SIZE | DWG. NO. |
| THE INFORMATION CONTAINED IN THIS | | A | Axial_Crush_Clamp |
| DRAWING IS THE SOLE PROPERTY OF | | SCALE: 1:1 | REV |
| ENTER COMPANY NAME HERE. ANY | | | |
| REPRODUCTION IN PART OR AS A WHOLE | | | |
| WITHOUT THE WRITTEN PERMISSION OF | | | |
| ENTER COMPANY NAME HERE IS | | | |
| PROHIBITED. | | | |

SOLIDWORKS Educational Product For Instructional Use Only.

2

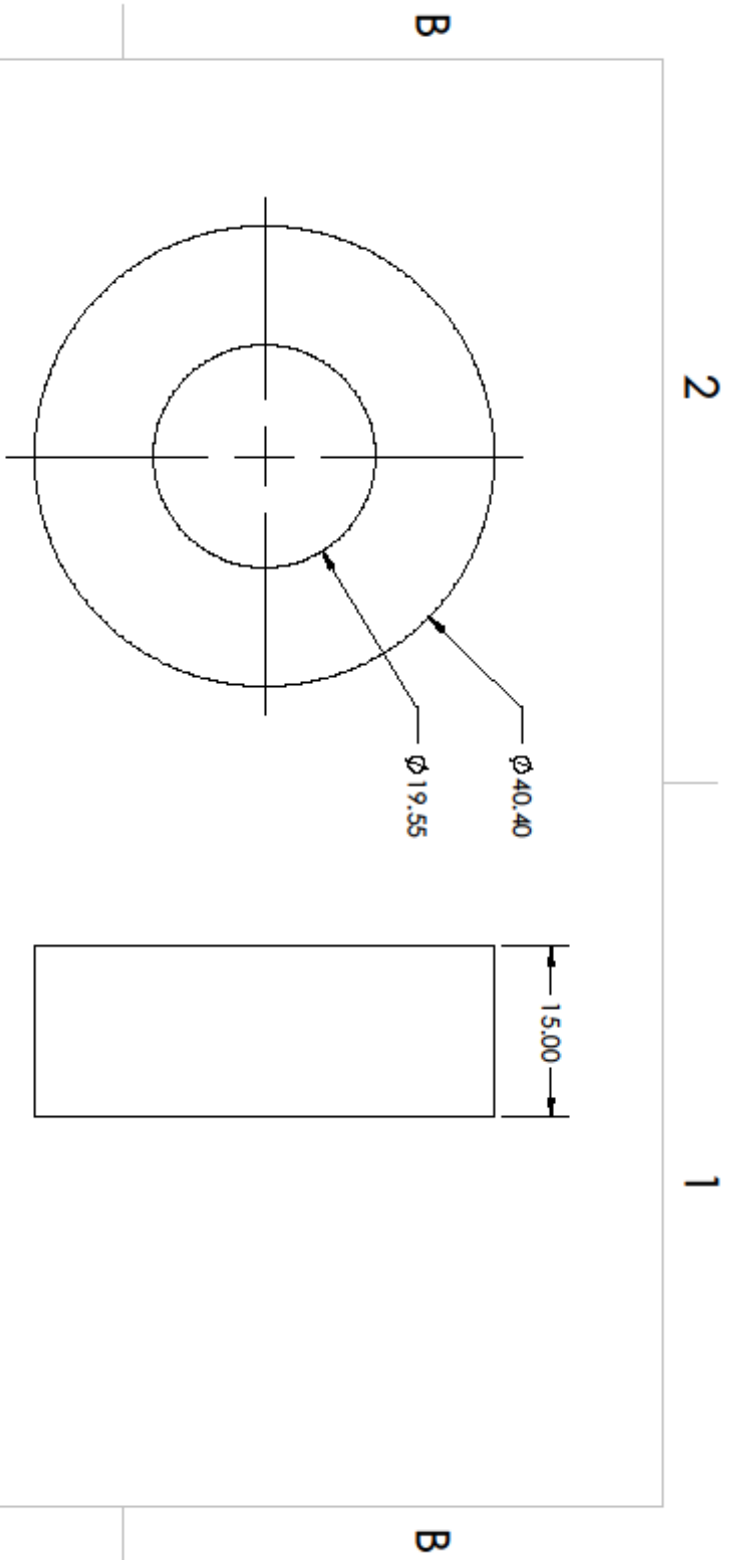
1



Hardened to 55 HRC

Top Block

| | | | |
|---|--|-------------------|---------------|
| UNLESS OTHERWISE SPECIFIED: | | NAME | DATE |
| DIMENSIONS ARE IN MM | | JG | 13/5/21 |
| TOLERANCES: ± 0.03/mm | | JG | 13/5/21 |
| | | BIG APPR | |
| | | MFG APPR | |
| | | Q.A. | |
| MATERIAL: AISI 4140 | | COMMENTS: | |
| FINISH | | | |
| USED ON | | | |
| NEXT ASSY | | | |
| APPLICATION | | | |
| DO NOT SCALE DRAWING | | | |
| PROPERTY AND CONFIDENTIALITY NOTICE: THIS DRAWING IS THE SOLE PROPERTY OF ANDERSON COMPANY. NAME, LETTERS, AND DIMENSIONS IN PART OR AS A WHOLE WITHOUT THE WRITTEN PERMISSION OF ANDERSON COMPANY. NUMBER IS PROHIBITED. | | SIZE | REV |
| | | A | |
| | | DWG. NO. | |
| | | Axial_Crush_Clamp | |
| | | SCALE: 1:1 | SHEET 9 OF 13 |



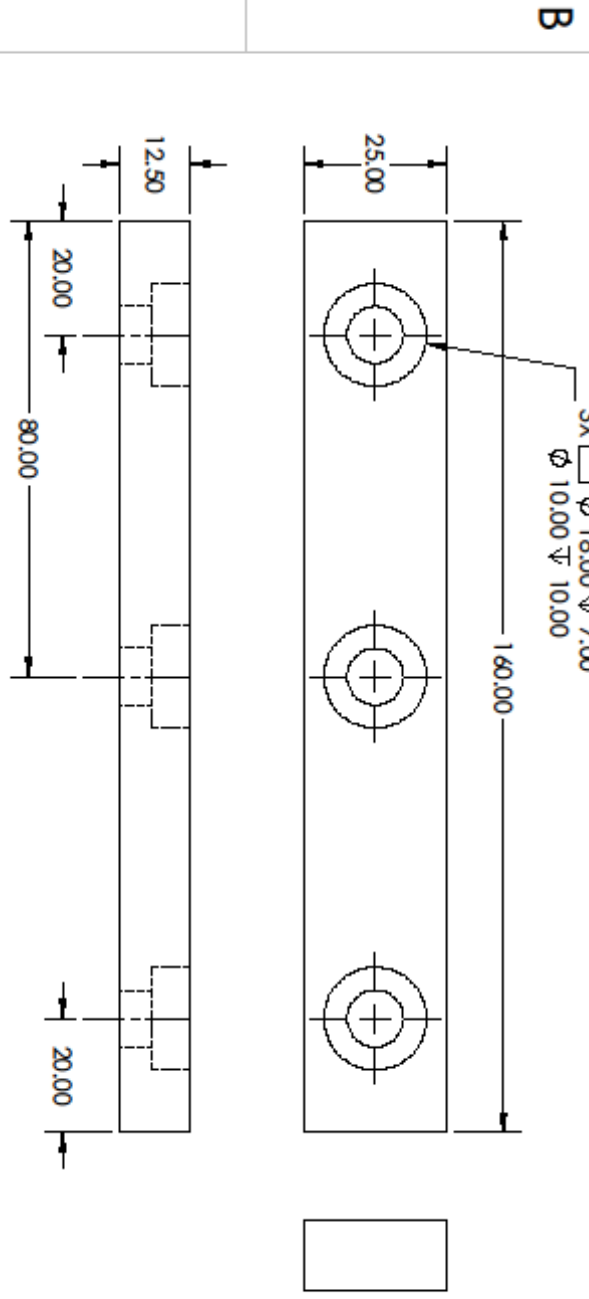
| | | | | | |
|-----------------------------|--|----------------------------|---------|-----------------------------------|---------|
| UNLESS OTHERWISE SPECIFIED: | | NAME | DATE | TITLE: Load Cell Spacer | |
| DIMENSIONS ARE IN INCHES | | DRAWN | JG | | 23/4/21 |
| TOLERANCES: | | CHECKED | JG | | 23/4/21 |
| FRACTIONAL ± | | BY | SHG/PRR | | MFO/AFR |
| ANGULAR MATCH ± | | THREE PLACE DECIMAL ± | | Q.A. | |
| TWO PLACE DECIMAL ± | | THREE PLACE DECIMAL ± | | COMMENTS: | |
| NEEDLE GEOMETRIC | | Q.A. | | SIZE DWG. NO. A | |
| TOLERANCES PER: | | Q.A. | | SCALE: 2:1 | |
| MATERIAL | | Slepaary UHMW Polyethylene | | WEIGHT: | |
| FINISH | | NONE | | SHEET 10 OF 13 | |
| DO NOT SCALE DRAWING | | NEXT ASSY | | REV | |
| APPLICATION | | USED ON | | | |

PROPRIETARY AND CONFIDENTIAL
 THE INFORMATION CONTAINED IN THIS DRAWING IS THE SOLE PROPERTY OF QIBERT COMPANY. ANY REPRODUCTION IN PART OR AS A WHOLE WITHOUT THE WRITTEN PERMISSION OF QIBERT COMPANY IS PROHIBITED.

SOLIDWORKS Educational Product For Instructional Use Only.

2

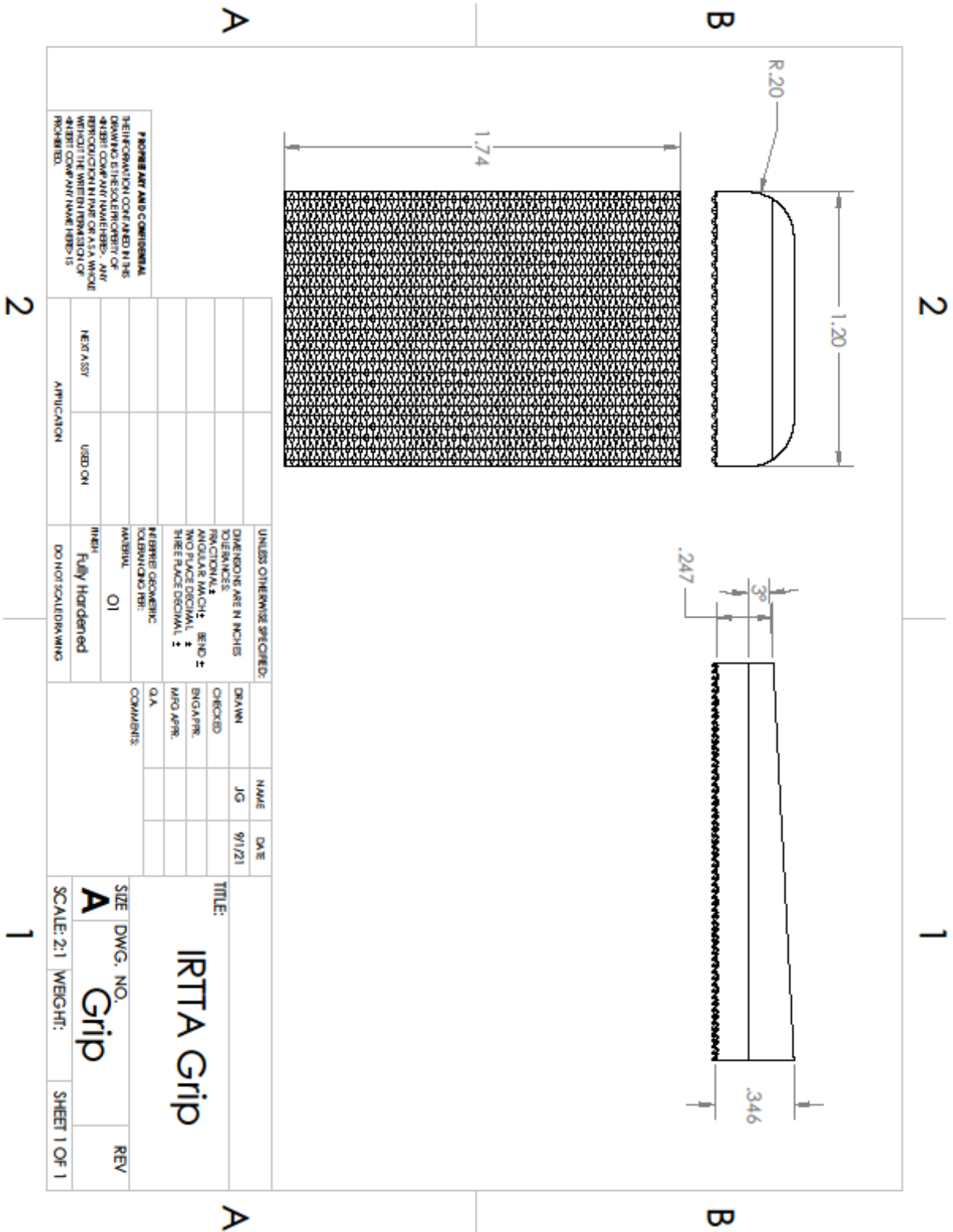
1



| | | | |
|--|--|---|--|
| <p>UNLESS OTHERWISE SPECIFIED: DIMENSIONS ARE IN MM TOLERANCES +/- 0.02 mm</p> | | <p>DATE: 13/5/21 DRAWN: JG</p> | |
| <p>MATERIAL: ALSI 4140</p> | | <p>CHECKED: JG 13/5/21</p> | |
| <p>COMMENTS:</p> | | <p>ENG APPR: MFG APPR: Q.A.</p> | |
| <p>NEE: ASV</p> | | <p>USED ON:</p> | |
| <p>APPLICATION:</p> | | <p>DO NOT SCALE DRAWING</p> | |
| <p>PROPERTY AND CONFIDENTIAL INFORMATION CONTAINED HEREIN IS THE SOLE PROPERTY OF HEBB. ANY REPRODUCTION IN PART OR AS A WHOLE WITHOUT THE WRITTEN PERMISSION OF HEBB IS PROHIBITED.</p> | | <p>SIZE: A DWG. NO.: Axial_Crush_Clamp</p> | |
| <p>REV</p> | | <p>SHEET 11 OF 13</p> | |

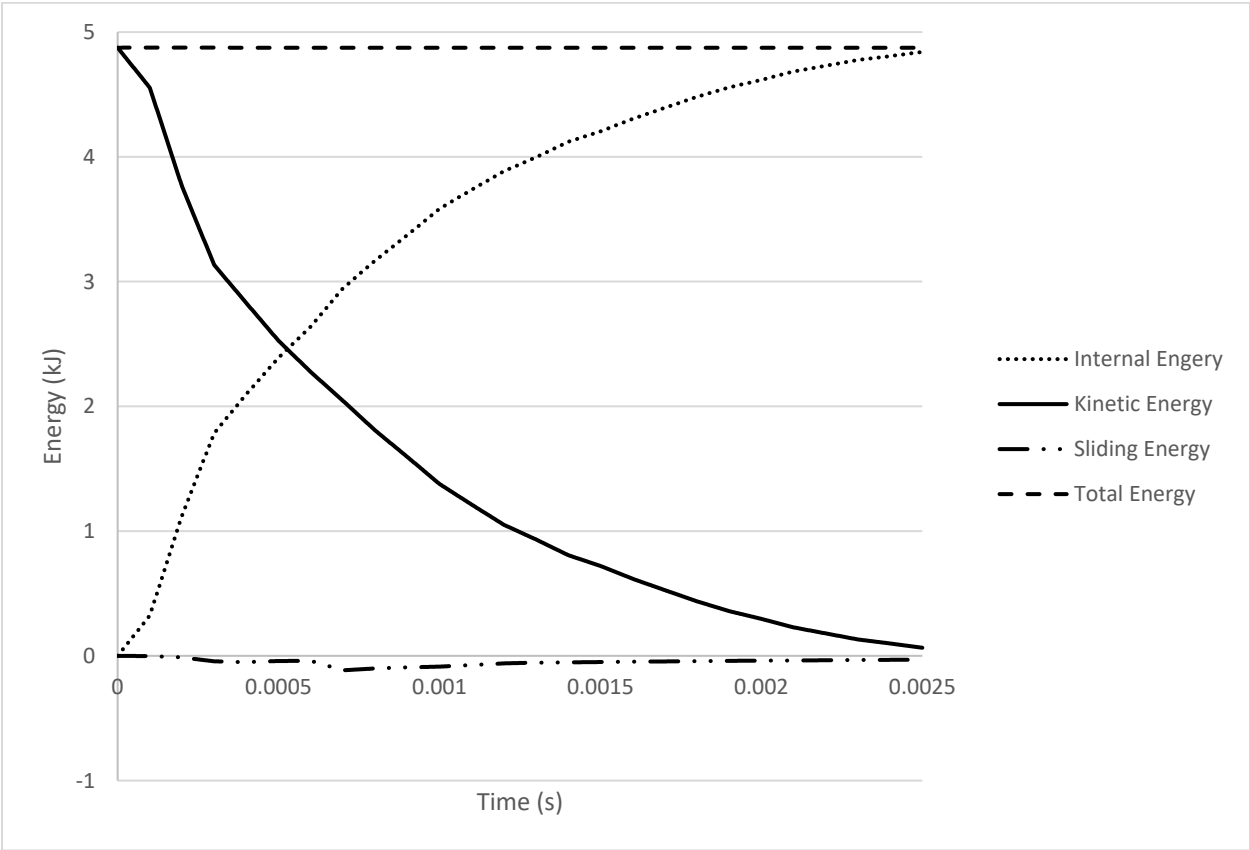
SOLIDWORKS Educational Product For Instructional Use Only.

A.3 Split Hopkinson Bar Grip Insert

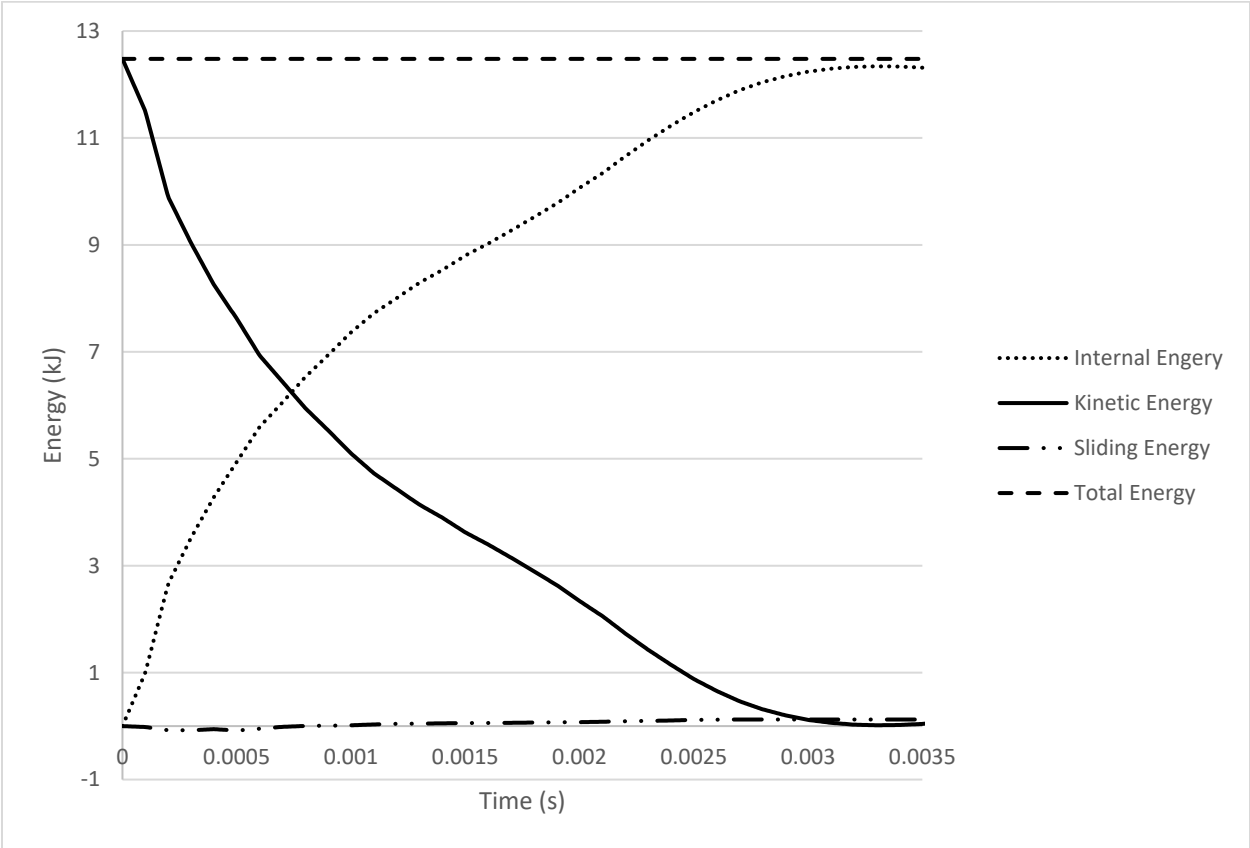


Appendix B. LS-Dyna Energy Balance

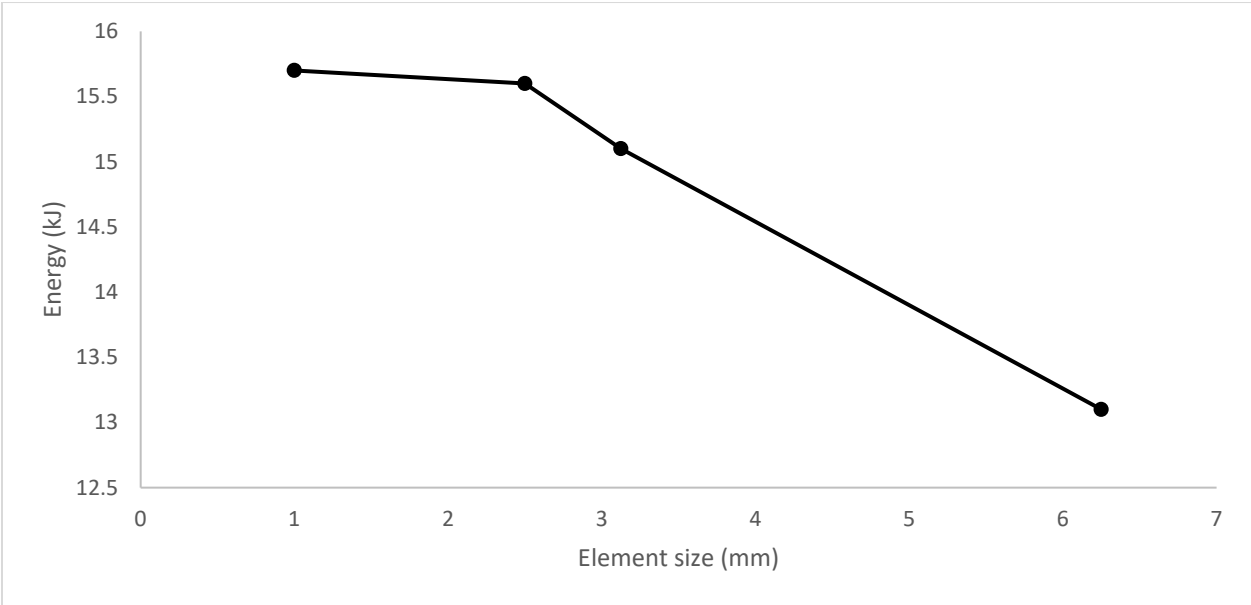
B.1 Tailored 1500 MPa PHS at 25 m/s



B.2 Tailored 2000 MPa PHS at 40 m/s



Appendix C. Mesh Sensitivity for Axial Crush Numerical Simulation



VITA AUCTORIS

NAME: Joseph Guignard

PLACE OF BIRTH: Windsor, ON

YEAR OF BIRTH: 1996

EDUCATION: Walkerville Collegiate Institute, Windsor, ON, 2014

University of Windsor, B.Sc., Windsor, ON, 2019